AN ABSTRACT OF THE DISSERTATION OF

Anna L. Herring for the degree of Doctor of Philosophy in Environmental Engineering presented on December 11, 2014.

Title: An Investigation into the Pore-Scale Mechanisms of Capillary Trapping: Application to Geologic CO_2 Sequestration

Abstract approved: ____

Dorthe Wildenschild

Geologic CO_2 sequestration is a climate change mitigation strategy that prevents CO_2 emissions to the atmosphere by capturing CO_2 gasses from large point source emissions streams and then pressurizing and pumping the supercritical-state CO_2 into underground geologic storage reservoirs. Once underground, CO_2 is prevented from buoyant migration to the surface by various trapping mechanisms, one of which is capillary trapping. Capillary trapping is a secure trapping mechanism that immobilizes CO_2 on relatively short timescales; accurate prediction and optimization of capillary trapping of CO_2 is crucial to ensure the safety and success of a sequestration operation. The research comprising this dissertation utilizes x-ray computed microtomography (x-ray CMT) to allow for three-dimensional (3D) investigation of the main factors influencing nonwetting phase capillary trapping from a pore-scale *in-situ* perspective. Results from ambient- and supercritical-condition experiments are presented that provide insight as to the controls on capillary trapping during multiphase flow in porous media. The presented findings may be used to help design injection strategies that optimize capillary trapping of CO_2 during sequestration operations and to help develop more accurate predictive transport models.

An Investigation into the Pore-Scale Mechanisms of Capillary Trapping: Application to Geologic CO_2 Sequestration

by
Anna L. Herring

A DISSERTATION

submitted to

Oregon State University

in partial fulfillment of
the requirements for the
degree of

Doctor of Philosophy

Presented December 11, 2014
Commencement June 2015

Doctor of Philosophy dissertation of Anna L. Herring presented on December 11, 2014

APPROVED:

Major Professor, representing Environmental Engineering

Head of the School of Chemical, Biological, and Environmental Engineering

Dean of the Graduate School

I understand that my dissertation will become part of the permanent collection of Oregon State University libraries. My signature below authorizes release of my dissertation to any reader upon request.

Anna L. Herring, Author

ACKNOWLEDGEMENTS

I would like to express sincere and immense appreciation to Dr. Dorthe Wildenschild; her technical expertise, support, and guidance have been instrumental to the completion of this dissertation and to my personal development as a scientist and researcher. I have benefitted from the knowledge and friendship of everyone in the Wildenschild Lab group, but especially from that of Dr. Linnéa Andersson; her assistance in conducting and interpreting beamtime experiments has been invaluable. I would like to thank my parents, Robin and Laurie Herring, for their unwavering love and support. I would also like to acknowledge all of my CCC buddies (especially Michael Freeman); thank you all so much for always being there for the nonacademic challenges and adventures.

CONTRIBUTION OF AUTHORS

The research presented in this dissertation is a product of the work of many researchers and could not have been completed without their help. Elizabeth Harper conducted the experiments and contributed analysis, and Brian Bay designed and supported the cone-beam tomography instrument for the study presented in Chapter 3; Ryan Armstrong and Ivan Lunati also contributed editorial and analytical support to that study. Linnéa Anderson assisted with experiments presented in Chapter 4; and Linnéa, Steffen Schlüter, and Adrian Sheppard also assisted with analysis of that data. The experiments of the study of Chapter 5 were conducted and analyzed in collaboration with Adrian Sheppard. The supercritical experimental set-up that was utilized for the experiments presented in Chapter 6 was designed and built with technical support from Linnéa Anderson and Dennis Newell; experiments were performed with considerable assistance from Linnéa Anderson; and Linnéa, Dennis, and Bill Carey also contributed editorial support to that study. Dorthe Wildenschild has provided technical, analytical, and editorial support for all the research comprising this dissertation.

TABLE OF CONTENTS

TABLE OF CONTENTS (Continued)

TABLE OF CONTENTS (Continued)

Page

LIST OF FIGURES

LIST OF FIGURES (Continued)

LIST OF FIGURES (Continued)

LIST OF FIGURES (Continued)

LIST OF FIGURES (Continued)

LIST OF FIGURES (Continued)

LIST OF FIGURES (Continued)

LIST OF TABLES

An Investigation into the Pore-Scale Mechanisms of Capillary Trapping: Application to Geologic CO_2 Sequestration

Chapter 1. Introduction

1.1 The role of capillary trapping in geologic CO_2 sequestration

Geologic sequestration of carbon dioxide (CO_2), also known as carbon capture and storage (CCS), has been proposed as a climate change mitigation strategy to limit carbon emissions from large point sources. CCS entails capturing CO_2 gases from the effluent of energy production plants, pressurizing the CO_2 into a supercritical fluid at conditions representative of geologic conditions, and pumping the supercritical-phase fluid into a saline aquifer or other geologic storage reservoir. Once injected into the subsurface, accurate prediction of the transport and trapping of supercritical CO_2 fluid is crucial because buoyant migration of un-trapped CO_2 fluid could result in leakage back to the atmosphere or groundwater contamination.

Once underground, CO_2 can be trapped via four different mechanisms: structural trapping, dissolution trapping, mineral trapping, and capillary (also known as residual) trapping. Structural trapping, also called hydrodynamic trapping, utilizes a caprock or impermeable layer to prevent the buoyant CO_2 plume from mobilizing upwards to the surface. Dissolution trapping occurs when supercritical CO_2 fluid dissolves into the resident brine of the formation and forms aqueous carbonate species; mineralization trapping occurs when these carbonate species precipitate out from solution to form a solid phase. Capillary trapping occurs when small clusters of the supercritical CO_2 fluid are isolated along the trailing edge of the migrating CO_2 plume due to capillary interactions between the CO_2, resident brine, and rock surface. Capillary trapping is an advantageous trapping mechanism because (1) it is a more secure form of trapping than structural trapping as it is less susceptible to failure due to geologic events (e.g. earthquakes) or unmapped preferential pathways (e.g. abandoned well bores or fault lines); (2) it has the potential to trap large fractions of the injected CO_2 tens to thousands of years earlier than dissolution or mineralization trapping; and (3) capillary trapping breaks up the larger CO_2 plume into small bubbles with large surface-to-volume ratio facilitating subsequent dissolution reactions (Figure 1-1, [*IPCC*, 2005]).

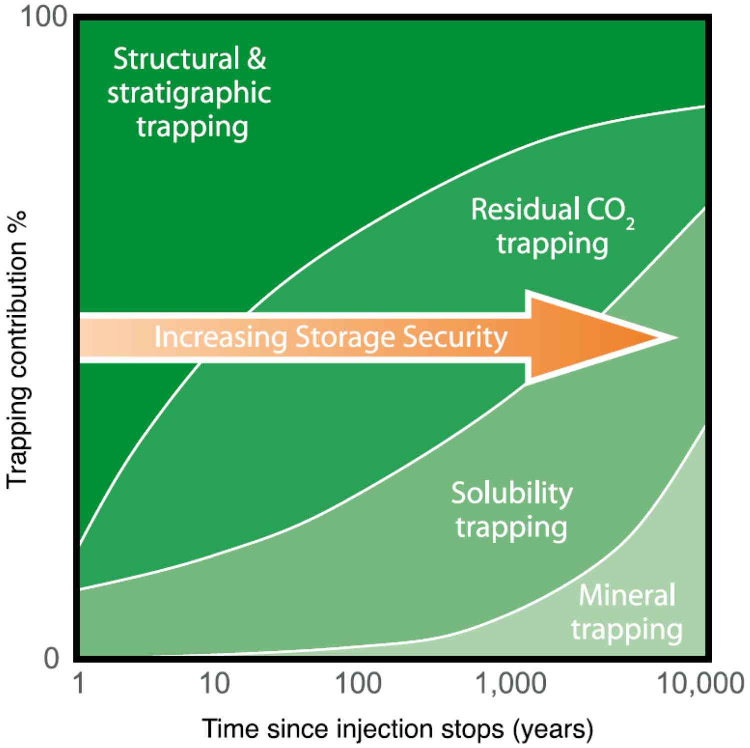

Figure 1-1. Subsurface storage mechanisms of CO_2 trapping are evaluated on the relative security of the trapping process and the time required for significant amounts of CO_2 to become immobilized [*IPCC*, 2005].

During immiscible multiphase flow, drainage is the process of nonwetting (NW) fluid invading the pore space and displacing wetting (W) fluid, and imbibition is the process of W fluid invading the pore space and displacing NW fluid; supercritical CO_2 fluid is expected to be the

NW fluid in the sedimentary reservoirs considered for storage scenarios (e.g. Krevor et al. [2012]). Capillary trapping of CO_2 occurs in two steps: first, CO_2 is injected into a saline reservoir, displacing the resident formation brine (drainage); then, as the buoyant CO_2 plume migrates away from the injection site, brine re-enters the pore space (imbibition), filling small pore throats and isolating CO_2 clusters in the pore bodies of the porous medium. CO_2 that is present at the endpoint of the drainage-imbibition cycle is thus capillary trapped (Figure 1-2).

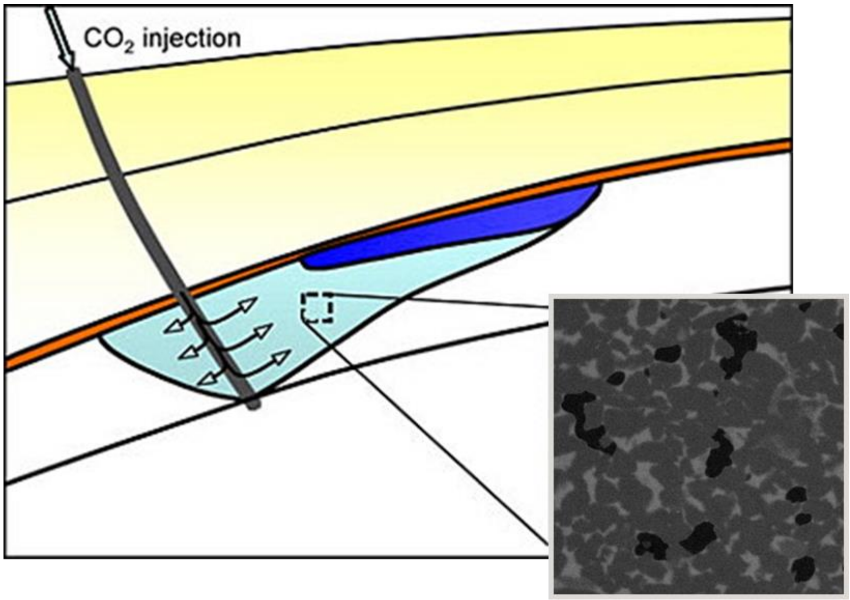

Figure 1-2. Schematic of CO_2 capillary trapping. CO_2 is injected and subsequently buoyantly migrates away from the injection well (dark blue). Light blue represents residually trapped CO_2. The zoomed-in view shows an x-ray tomographic image of bubbles of nonwetting (NW) fluid (black) that have been capillary trapped in the pore space of sandstone (intermediate gray color) by wetting (W) phase (light gray color). Modified from an image by Ruben Juanes, MIT.

Many engineered processes in the subsurface require fundamental understanding of drainage and imbibition processes and the accompanying NW phase capillary trapping; for example, during oil recovery operations, remediation of non-aqueous phase liquid (NAPL) contaminants in the subsurface, or gas-liquid mass transfer processes in the vadose zone. In these examples, water is generally considered to be the W phase, while oil/NAPL/gas are the NW phase. Consequently, comparisons can be made between previous oil/NAPL/gas-water studies and CO_2 sequestration.

However, the study of CO_2 sequestration introduces three new complications to the study of NW phase trapping: (1) the geologic matrix surface may exhibit intermediate or CO_2-wet wettability, or progressively transition to a different wettability upon exposure to the supercritical CO_2-brine fluid mixture [*Chalbaud et al.*, 2007; *Chiquet et al.*, 2007b; *Kim et al.*, 2012]; (2) the supercritical state of the fluid results in highly variable fluid properties (viscosity, density, interfacial tension, solubility) as a function of pressure and temperature [*Chiquet et al.*, 2007a; *Bachu and Bennion*, 2008, 2009; *Bachu et al.*, 2009]; and (3) both the *drainage* process (CO_2 injection) as well as the *imbibition* process (subsequent waterflood or natural groundwater flow) can be manipulated; whereas in oil recovery or NAPL remediation applications, NW fluid is initially present in the medium and only the imbibition process can be engineered.

The research presented in this dissertation examines the individual and interrelated effects of these three factors (fluid property variation, and initial-residual relationships, and wettability state) on capillary trapping and pore-scale multiphase flow patterns with application to geologic sequestration of CO_2. Flow and trapping of the NW phase is characterized on a pore-scale basis using x-ray microtomography (x-ray CMT), which allows for three dimensional (3D) *in-situ* visualization of the W, NW, and solid phases. We investigate the fundamental mechanisms of capillary trapping as a function of fluid properties and pore-scale forces, initial system state, and medium wettability via ambient pressure and temperature condition systems of NW phase (air) and W phase (brine) in Bentheimer sandstone and glass beads. We also present results of supercritical condition CO_2 and brine experiments in Bentheimer sandstone and relate the results to previous ambient condition studies.

1.2 Document Organization

Chapter 2 presents a brief overview of the basics of multiphase flow (Chapter 2.1) and capillary trapping in terms of fluid properties, the initial state of the system, and wettability state of the medium (Chapter 2.2). Chapter 2.3 provides an introduction to x-ray CMT imaging, which is the primary experimental technique utilized for pore-scale investigations comprising the research of this dissertation.

To explore the impact of fluid property variation on capillary trapping, Chapter 3 presents a study investigating dominant fluid properties and pore-scale forces in ambient condition experiments of multiple fluid pairs in a glass bead porous medium; in Chapter 4 an approach for analysis and characterization of pore-scale force dominance is demonstrated, which explains the behavior of the glass bead system as compared to that of a natural geologic medium (Bentheimer sandstone). Also in Chapter 4, the relationship between the system initial state and NW capillary trapping is also explored via an analysis of initial NW phase connectivity and topology in an ambient condition Bentheimer sandstone system. Medium wettability effects are investigated in the study presented in Chapter 5, which details an ambient condition experimental study of flow patterns and capillary trapping of NW phase in wettability-altered Bentheimer sandstone. Chapter 6 showcases our supercritical experimental set-up and the results of our first supercritical experimental run and demonstrates how supercritical and ambient condition experiments can be related via nondimensionalization of fluid properties. Finally, Chapter 7 provides summary and conclusions of this research, as well as future work that is intended on these topics.

Chapter 2. Background

2.1 Basics of Multiphase Flow

The wettability of a medium surface describes the affinity of a solid surface for one fluid relative to the other fluid in an immiscible multiphase system. The wettability of a surface is quantified by the contact angle that is created by the tangent line of the fluid-fluid interface drawn to the intersection point of the fluid-fluid-solid phases (Figure 2-1). In geologic applications (e.g. an oil-water or CO_2-brine system), the contact angle is generally measured through the aqueous phase. For a solid medium in the presence of two fluids, the fluid that preferentially spreads across the surface is termed the wetting fluid, and the other fluid is the nonwetting fluid. In the examples in Figure 2-1, a contact angle (measured through the aqueous phase) near 0^o indicates that the surface is water-wet, a contact angle near 180^o indicates a CO_2-wet surface, and an angle between these extremes (e.g. an angle of approximately $75\text{-}105^o$) indicates intermediate-wet conditions [*Treiber and Owens*, 1972; *Anderson*, 1987].

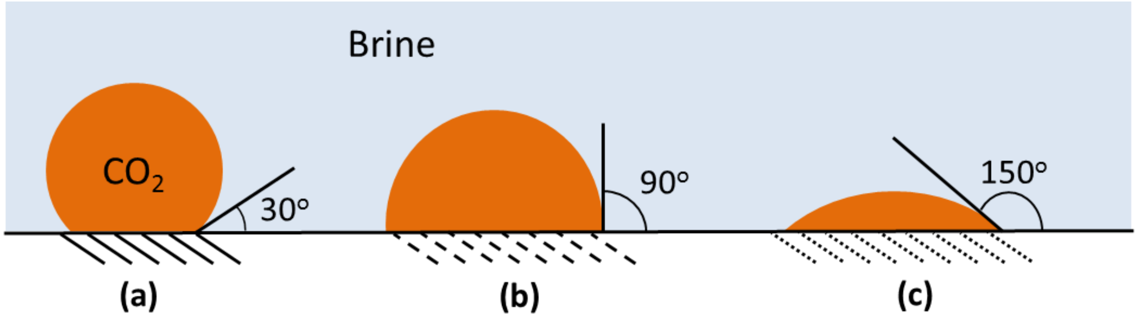

Figure 2-1. Contact angles, measured through the brine phase, of three idealized CO_2-brine systems: (a) illustrates a brine-wet medium, (b) an intermediate-wet system and (c) a CO_2-wet system.

In an immiscible multiphase system in a porous medium, a curved interface may be formed at the boundary between two fluid phases. In a static system at equilibrium, the interfacial tension forces creating this curvature are balanced by a pressure difference across the interface, defined as capillary pressure, P_c [*Anderson*, 1987]. The Young-Laplace equation states that the capillary pressure is a function of the interfacial tension between the wetting and nonwetting phase fluids (σ), the contact angle (θ), and the effective radius (r) of the interface:

$$P_c = P_{NW} - P_W = \frac{2\sigma\cos(\theta)}{r} \qquad \text{(eqn. 2.1)}$$

Capillary pressure can also be thought of as the pressure difference value that must be exceeded in order to mobilize NW phase fluid through a constriction (pore throat) of radius r. Equation 2.1 dictates that NW phase fluid can more easily pass through pore throats with larger radii, while higher capillary pressure is required to mobilize NW fluid through smaller pore throats.

The dependence of capillary pressure on r explains the shape of a capillary pressure-saturation (P_c-S) curve for a porous medium comprising a range of pore body and throat sizes (Figure 2-2). For a medium undergoing drainage, some finite capillary pressure is required to introduce NW phase into the pore space (the “entry pressure”). As capillary pressure increases, NW phase invades smaller and smaller pore bodies and throats until all available wetting phase has been displaced from the medium. For a system undergoing imbibition, W phase first fills the smallest constrictions in the porous media and requires lower capillary pressure (higher wetting phase pressure) to invade the larger pore bodies and throats. Imbibition capillary pressures are reduced relative to the drainage capillary pressure for the same saturation value; the difference in drainage and imbibition curves is termed P_c-S hysteresis (e.g. Selker et al. [1999]). The difference in W phase saturation between the start of the primary drainage curve and the endpoint of the secondary imbibition curve is equivalent to the capillary trapped NW phase saturation.

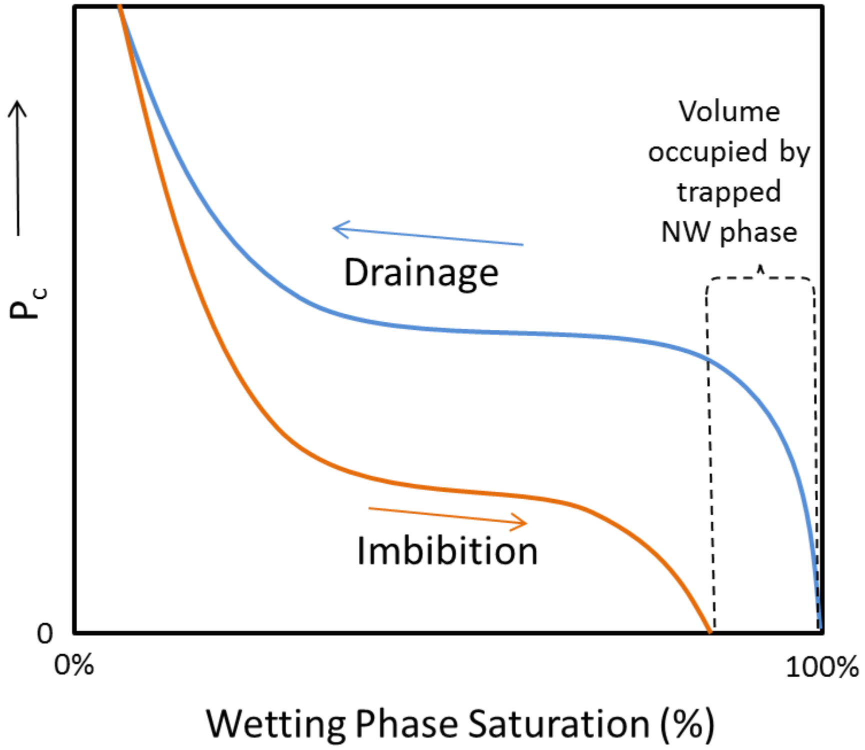

Figure 2-2. Capillary pressure-saturation (P_c-S) relationship for primary drainage and secondary imbibition in a porous medium. The difference in saturation between the start of drainage and the end of imbibition is equivalent to the amount of pore space occupied by trapped nonwetting (NW) phase.

Because W phase fluid is continuous through small constrictions while NW phase resides in larger pore spaces, upon imbibition, W phase will flow via films on the medium surface and invade the small pore throats surrounding NW fluid, thereby disconnecting NW phase clusters from the mobile NW fluid flow paths. This is termed "snap-off" and is a major mechanism contributing to capillary trapping; alternatively, W fluid may circumvent NW fluid clusters ("bypassing"), which also results in capillary trapped NW fluid [*Chatzis et al.*, 1983].

2.2 Factors Impacting Capillary Trapping

Given the controls on multiphase flow described above, there are three factors that warrant investigation in regards to capillary trapping of supercritical CO_2; these are introduced below.

2.2.1 Supercritical CO_2 Fluid Properties

Supercritical CO_2 fluid properties are highly sensitive to pressure and temperature conditions. Figure 2-3 shows values for CO_2 (a) viscosity and (b) density as a function of pressure and temperature [*Bachu*, 2003]; these parameters generally increase as pressure increases and decrease as temperature increases. CO_2 solubility in brine also increases with pressure increase and decreases with temperature increase; additionally, CO_2 solubility decreases as brine concentration increases (e.g. Iglauer 2011). Interfacial tension between CO_2 and brine is also dependent on brine composition, as well as temperature and pressure (Figure 2-4).

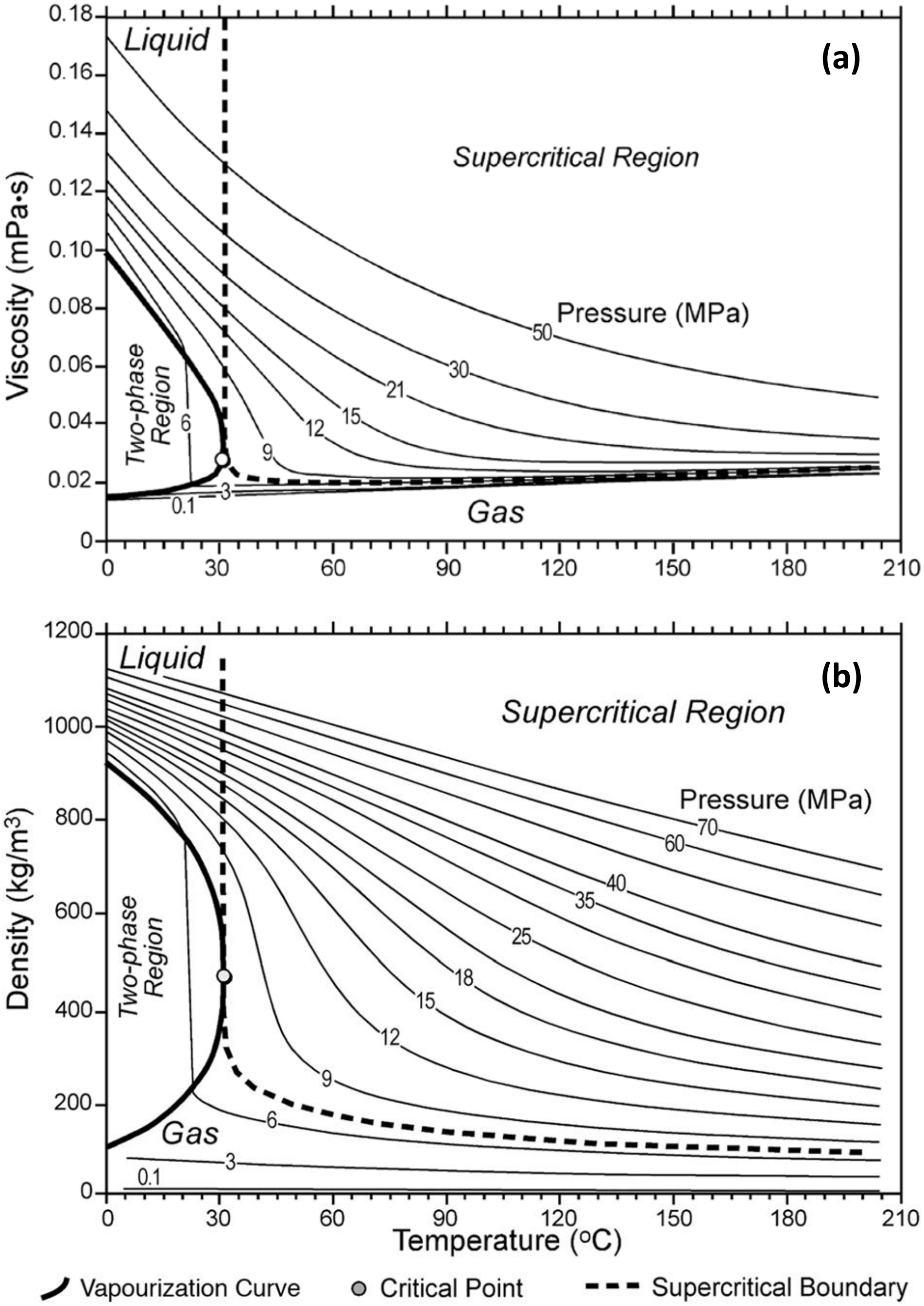

Figure 2-3. Variation of (a) viscosity and (b) density of CO_2 as a function of pressure and temperature [*Bachu*, 2003].

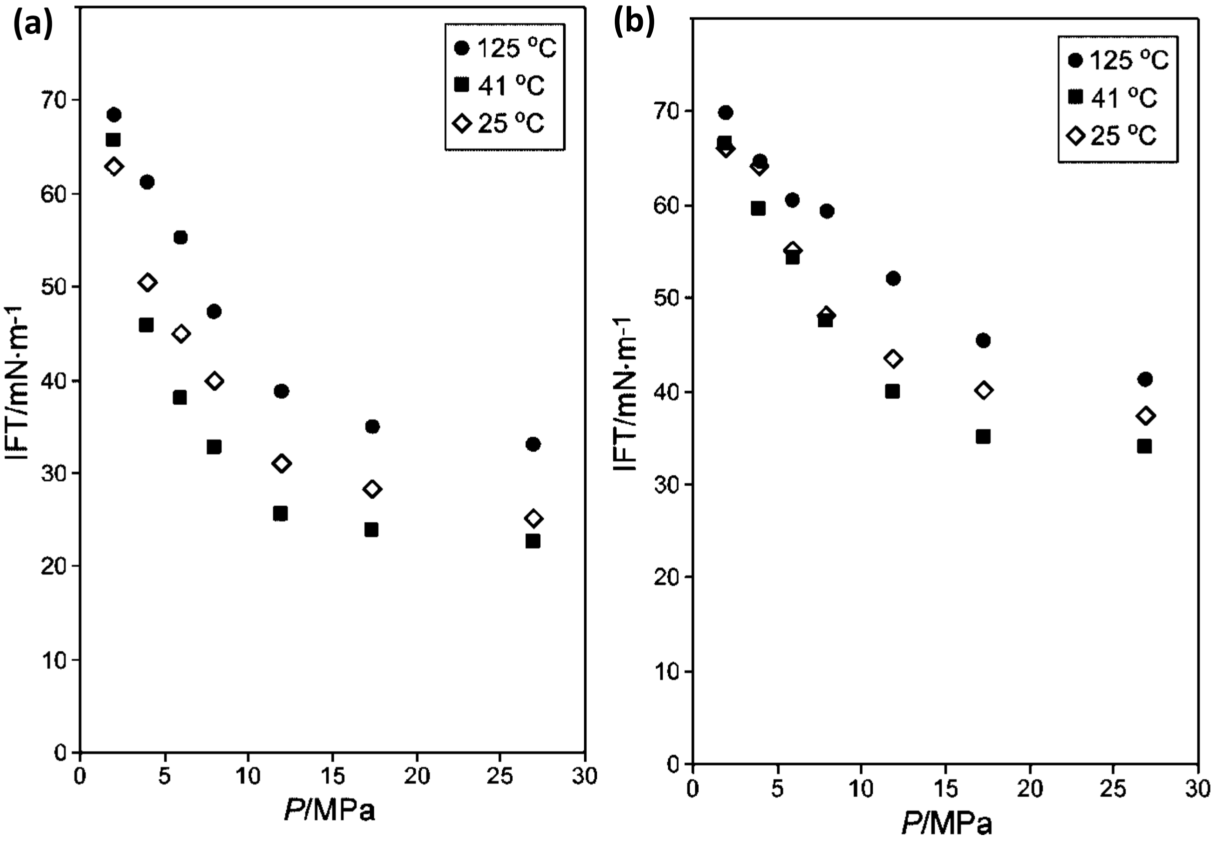

Figure 2-4. Interfacial tension (IFT) of CO_2 and brine as a function of pressure (P), temperature, and brine salinity: (a) 75,780 mg·L^{-1}, and (b) 282,770 mg·L^{-1}. Reprinted with permission from Bachu et al. [*Bachu et al.*, 2009]. Copyright (2009) American Chemical Society.

Multiphase fluids flowing through porous media are subject to capillary, viscous, and gravitational forces; and the relative importance of these forces is dependent on fluid properties, including W and NW viscosity and density, and W/NW interfacial tension. Dimensionless numbers have been developed which combine fluid flow parameters to allow comparison of different systems. The capillary number (Ca) describes the ratio of viscous force to capillary forces, and although there are numerous formulations of Ca [*Chatzis and Morrow*, 1984; *Jamaloei et al.*, 2012; *Armstrong et al.*, 2014], we define it as follows:

$$Ca = \frac{\mu_{INV} v_{INV}}{\sigma} \qquad \text{(eqn. 2.2)}$$

where μ_{INV} is the invading phase viscosity, v_{INV} is the invading phase pore velocity (the Darcy velocity divided by the porosity of the medium), and σ is the interfacial tension between the wetting and nonwetting phases.

In order to take into account the defending phase viscosity, μ_{DEF}, we define the mobility ratio (M, sometimes called the "viscosity ratio") as:

$$M = \frac{\mu_{INV}}{\mu_{DEF}} \qquad \text{(eqn. 2.3)}$$

The interaction between gravitational and capillary forces is described by the Bond number (Bo), which we define as:

$$Bo = \frac{\Delta\rho \cdot g \cdot d^2}{\sigma} \qquad \text{(eqn. 2.4)}$$

where $\Delta\rho$ is the difference in W/NW densities, g is the gravitational constant, and d is a representative length scale (for investigating capillary trapping on a pore-scale basis, we chose d to be the representative grain/bead diameter of the porous medium).

Finally, the capillary and Bond numbers of a flow process can be combined in order to describe the relative importance of gravitational and viscosity forces, as follows:

$$Ca \cdot Bo^{-1} = \frac{\mu_{INV} v_{INV}}{\Delta\rho \cdot g \cdot d^2} \qquad \text{(eqn. 2.5)}$$

Note that this term is not independent of Ca and Bo. Previous studies of micromodels have developed so-called fluid flow regimes which are defined by the combination of Ca and M values of a drainage process [*Lenormand et al.*, 1988; *Zhang et al.*, 2011; *Wang et al.*, 2012] (Figure 2-5). Although analogous regimes are not well-defined for the imbibition process (during which capillary trapping of NW phase occurs), similar flow behavior has been observed and qualitative descriptions have been developed. For low capillary number displacement, capillary forces dominate, and the invading fluid flows in all directions, even against the direction of injection. When capillary number increases, viscous forces become more dominant and the front morphology is dictated by the viscosity ratio M (e.g. Lenormand et al. [1988]; Ferrari and Lunati [2013]). For M>1 the invading fluid is more viscous than the defending fluid, the front is stable and tends to remain compact. For M<1, the invading fluid is less viscous, and the front is destabilized by viscous effects; and long, thin fingers of invading fluid develop.

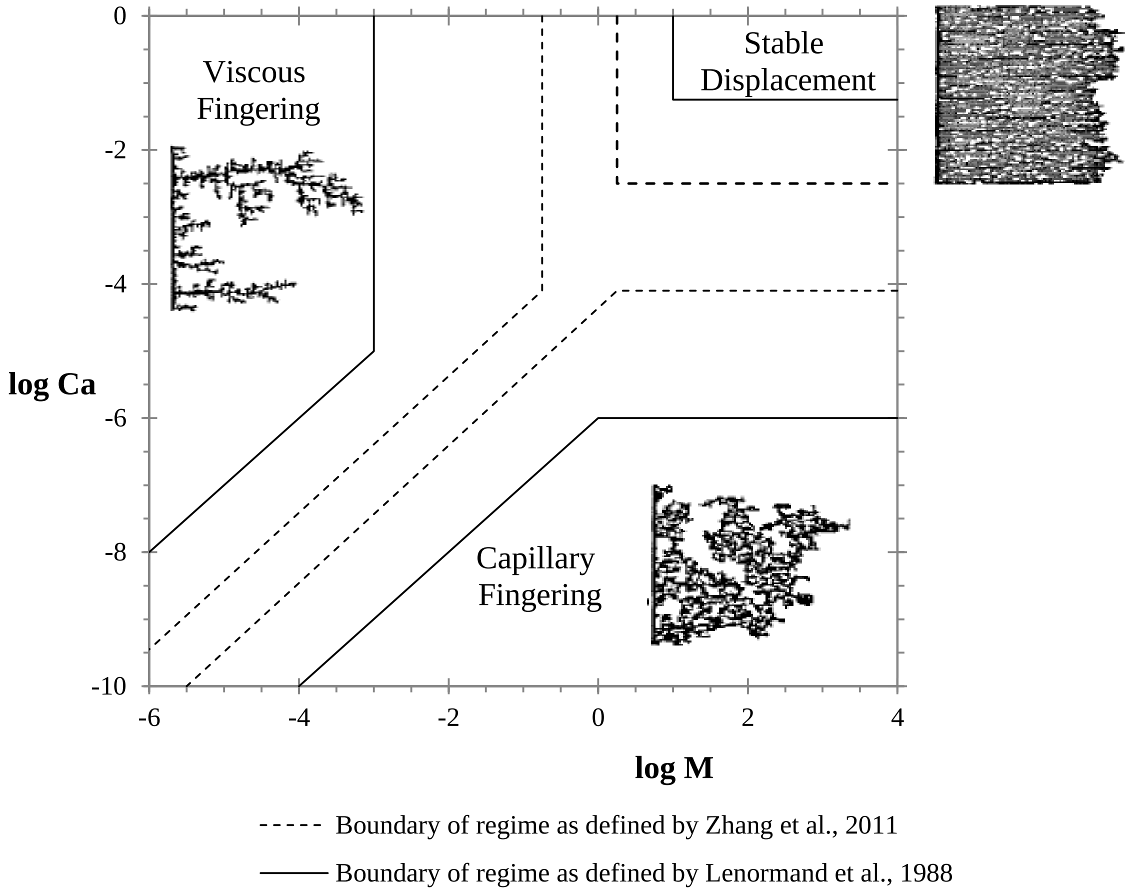

Figure 2-5. Flow regimes of nonwetting (NW) phase flow during drainage as a function of capillary number (Ca) and mobility ratio (M) of the drainage process. These regimes are developed from investigation of two-dimensional (2D) micromodel experiments originally performed by Lenormand et al. [1988] and subsequently revisited by Zhang et al. [2011]. Depictions of flow regimes from Lenormand et al. [1988].

Numerous studies have investigated the influence of fluid property variation during the imbibition process on capillary trapping; generally, as capillary forces are reduced relative to viscous or gravitational forces (i.e. as the imbibition capillary or Bond number increase), capillary trapping is reduced [*Chatzis and Morrow*, 1984; *Chatzis et al.*, 1988; *Morrow et al.*, 1988; *Fry et al.*, 1997; *Hughes and Blunt*, 2000; *Nguyen et al.*, 2006; *Ding and Kantzas*, 2007; *Cense and Berg*, 2009]. However, there are exceptions and contradictions to these general empirical relationships [e.g. *Harper and Wildenschild*, 2012; *Geistlinger et al.*, 2014]. In Chapters 3 and 4, two ambient condition studies are described which investigate the effect of variation of fluid properties and dimensionless ratios, and an approach which utilizes what is termed the “pore-scale force balance” is presented in order to characterize a system and allow for prediction of the dominant controls on the resulting amount of NW phase capillary trapping.

2.2.2 Initial State of the System

Previous studies focusing on capillary trapping for oil recovery applications have demonstrated that the residual NW phase saturation (i.e. the amount of NW phase present after imbibition) is dependent on the amount of NW phase initially in the system [*Land*, 1968; *Al Mansoori et al.*, 2010; *Akbarabadi and Piri*, 2013]. For an oil recovery scenario, the initial NW saturation is fixed, the initial NW saturation is simply the oil originally present in the reservoir. However, for a CO_2 sequestration project, there is no CO_2 present in the original state of the storage reservoir, and the initial saturation of CO_2 can be manipulated based on CO_2 injection parameters; this allows for engineered manipulation of both the drainage and imbibition process. We refer to a system prior to any injection as being the *original state* of the system; the end of the drainage process (CO_2 injection) is the *initial state*; and the end of the imbibition process is the *residual state* of the system (Figure 2-6).

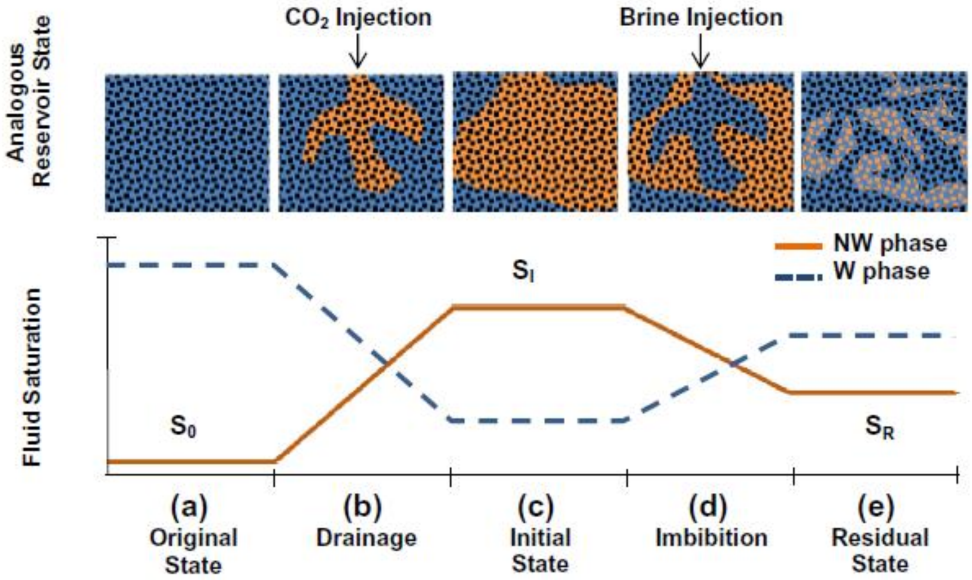

Figure 2-6. Nomenclature applied to a CO_2 sequestration processes: (a) original state, S_0: reservoir prior to CO_2 injection; (b) drainage: reservoir during CO_2 injection; (c) initial state, S_I: reservoir just after CO_2 injection; (d) imbibition: reservoir during waterflood injection or natural groundwater flow; and (e) residual state, S_R: final reservoir state after migration of mobile CO_2 plume and reinvasion of the pore space by wetting (W) phase.

Empirical models such as Land's model [*Land*, 1968] illustrate the general relationship between initial (S_I) and residual (S_R) NW phase saturations (Figure 2-7) on a core-scale basis, and recent advances in x-ray CMT technology allow for investigation of the pore-scale physics which control these relationships. In Chapter 5, we present experimental results that explore how *initial* NW phase connectivity and topology at the pore-scale influence overall NW phase trapping and how this information can be applied to CO_2 sequestration scenarios in order to enhance capillary trapping.

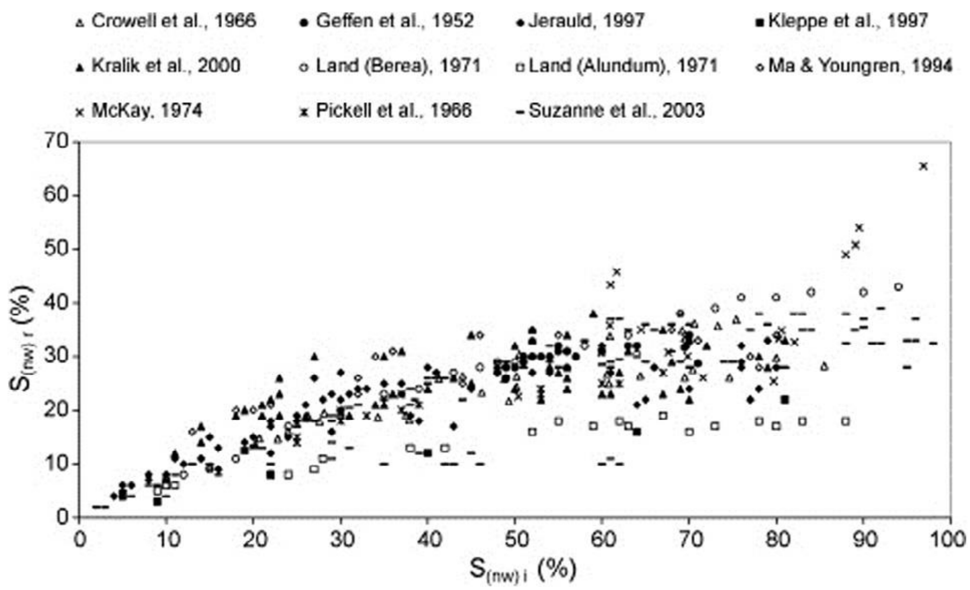

Figure 2-7. Experimental data demonstrating the relationship between initial nonwetting (NW) phase saturation ($S_{(NW)\,i}$) and residual NW phase saturation ($S_{(NW)\,r}$), from Al Mansoori et al. [*Al Mansoori et al.*, 2010].

2.2.3 Wetting Behavior of a Multiphase Fluid-Porous Medium System

Some studies have indicated that exposure of the host rock to supercritical CO_2 and brine solutions may cause a transition in wettability state from water-wet to intermediate-wet conditions, i.e. an increase in contact angle towards 90^o [*Chiquet et al.*, 2005, 2007a; *Chalbaud et al.*, 2007; *Broseta et al.*, 2012; *Kim et al.*, 2012]. As demonstrated by Equation 2.1, an increase in contact angle reduces the capillary pressure required to mobilize NW fluid through a constriction (pore throat), allowing for migration of NW phase under relatively lower applied pressure gradients. Conceptually, as a surface exhibits a weaker affinity for wetting phase, W fluid flow through small constrictions or as a film on the medium surface is less likely to occur; thus, snap-off is suppressed, and the amount of NW phase capillary trapping decreases. Therefore, wettability changes may have a dramatic impact on the efficiency of a CO_2 sequestration operation.

In order to investigate the effect of wettability on capillary trapping and NW flow patterns during drainage and imbibition, we have conducted a series of ambient-condition experiments of brine and air within Bentheimer sandstone cores that have been chemically treated such that the sandstone surface ranges from water-wet to intermediate-wet to air-wet; this study is presented in Chapter 5.

2.3 X-ray Computed Microtomography

The experimental research presented in this dissertation is largely derived from x-ray computed microtomography (x-ray CMT) images of pore-scale phenomena. X-ray CMT is a non-destructive method of imaging a three-dimensional (3D) sample by mapping the x-ray attenuation values of the internal structure of the sample; this technology has been used to investigate flow processes in porous media for a variety of applications [*Ketcham and Carlson*, 2001; *Wildenschild et al.*, 2002; *Taina et al.*, 2008; *Cnudde and Boone*, 2013; *Wildenschild and Sheppard*, 2013]. In general, x-rays are emitted from a source and passed through the sample, and contiguous, sequential radiographs are collected by a detector as the sample rotates in minute increments. The collected radiographs are reconstructed to create a single 3D volume comprised of voxels (the 3D analogue to pixels), wherein the phases present in the sample (e.g. solid, gas, liquid) are identifiable by their relative grayscale values (Figure 2-8a). Image filters may be applied to the grayscale data volume to reduce noise and imaging artifacts. Segmentation of the data is generally accomplished by measuring a histogram of all the grayscale values comprising the data volume and setting a segmentation threshold at the local minimum between two peaks representing different phases present in the volume (Figure 2-8b). Thus, the grayscale data is converted into a data volume, wherein each phase is labeled with its own value (Figure 2-8c); and quantification (e.g. saturation, connectivity, and topological values) is performed on the labeled volume.

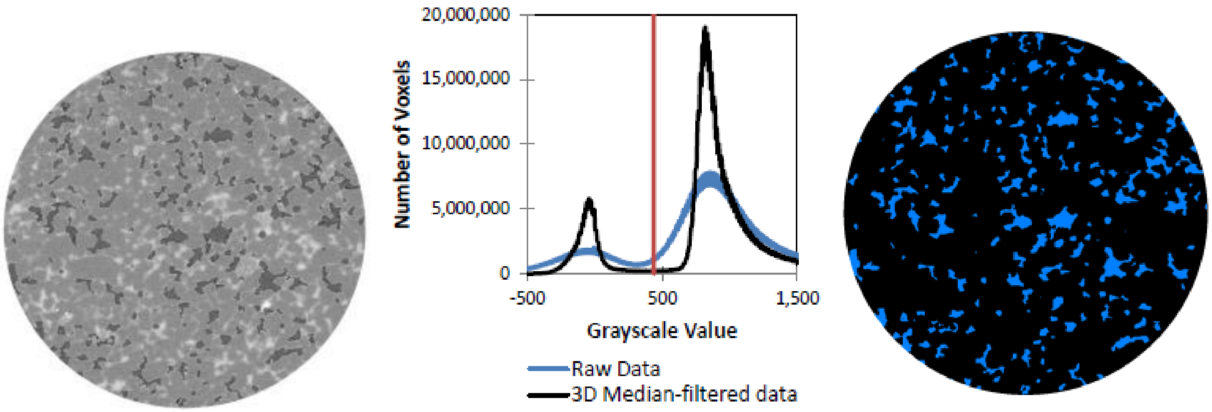

(a) **(b)** **(c)**

Figure 2-8. Data segmentation process: (a) a cross-sectional slice of grayscale data, (b) the grayscale histogram of the data volume for both raw and three-dimensional (3D) median-filtered data with the grayscale threshold value indicated, and (c) segmented data with the nonwetting (NW) phase identified.

In Chapters 4 and 5, the Euler number (χ) is used to quantify the topology of NW phase fluid. Euler number values are calculated for NW phase fluid via the difference between the first two Betti numbers:

$$\chi = \beta_0 - \beta_1 \qquad \text{(eqn. 2.6)}$$

β_0 is the number of discrete, individual objects (individual NW fluid bubbles or clusters) and β_1 is the number of redundant connections or loops within objects (redundant NW phase pathways formed by connections through multiple pore throats); examples of Betti number features of NW phase fluid within a porous medium are illustrated in Figure 2-9.

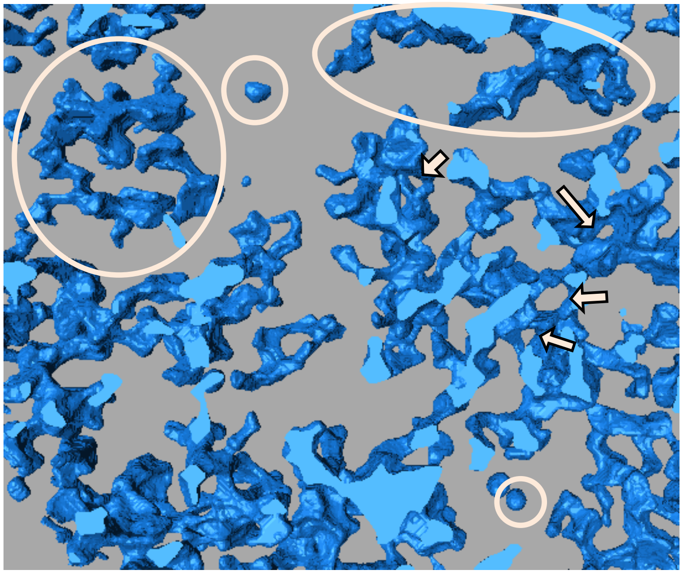

Figure 2-9. Examples of nonwetting (NW) fluid features contributing to the zeroth Betti number (β_0, indicated with circles) and the first Betti number (β_1, indicated with arrows) of a three-dimensional (3D) data volume.

The research of this dissertation utilizes a variety of x-ray CMT systems; specific details of collection, processing, segmentation, and quantification for each study are presented in their respective chapters.

Chapter 3. On the Optimization of Capillary Trapping during Geologic CO_2 Sequestration

Elizabeth J. Harper[1], Anna L. Herring[1], Ryan T. Armstrong[1,2], Ivan Lunati[3], Brian K. Bay[4], Dorthe Wildenschild[1]

[1]*School of Chemical, Biological and Environmental Engineering, Oregon State University, Corvallis, OR*
[2]*School of Petroleum Engineering, University of New South Wales, NSW 2052 Sydney, Australia*
[3]*Institute of Earth Sciences, University of Lausanne, Lausanne, Switzerland*
[4]*School of Mechanical, Industrial and Manufacturing Engineering, Oregon State University, Corvallis, OR*

International Journal of Greenhouse Gas Control
IEA Greenhouse Gas R&D Programme, Cheltenham, UK
Submittal expected December 2014

3.1 Abstract

Geological carbon sequestration is being considered worldwide as a means of mitigating anthropogenic emission of greenhouse gases. During sequestration, carbon dioxide (CO_2) gas effluent is captured from coal-fired power plants or other concentrated emission sources and injected into saline aquifers or depleted oil reservoirs for long term storage. In an effort to fully understand and optimize CO_2 trapping efficiency, the capillary mechanisms that immobilize subsurface CO_2 were analyzed at the pore-scale. Pairs of proxy fluids representing the potential range of in-situ conditions of supercritical CO_2 (nonwetting fluid) and brine (wetting fluid) were used during experimentation. The two fluids were imbibed and drained from a flow cell apparatus containing a sintered glass bead core. Fluid parameters (such as interfacial tension and fluid densities and viscosities) and flow rate were altered to characterize their relative impact on capillary trapping. Computed x-ray microtomography (microCT) was used to quantify immobilized nonwetting fluid volumes after imbibition and drainage events. MicroCT-analyzed data suggests that capillary trapping in sintered glass bead (a mildly consolidated porous medium) is dictated by the capillary number (Ca), the mobility ratio (M), and the Bond number (Bo) of the system, reflecting that all three viscous, capillary, and gravitational forces affect the displacement process to varying degree as their relative importance and the mobility ratio changes. The amount of residual trapped nonwetting phase was observed to increase with increasing nonwetting fluid viscosity, and with decreasing density difference of the fluids; this suggests that CO_2 sequestration can potentially be engineered for optimal trapping through alterations to the viscosity or density of supercritical CO_2.

3.2 Introduction

Carbon dioxide (CO_2) is emitted into the atmosphere through burning of fossil fuels for energy production. Combustion of fossil fuels accounts for approximately 75% of the atmosphere’s total anthropogenic CO_2 emissions and is currently released into the atmosphere at a rate higher than it can be removed by natural sources [IPCC, 2005a].

As a means of mitigating CO_2 emissions, carbon capture and storage (CCS) collects, concentrates, and transfers a stream of CO_2 from point sources of emissions to the injection site. To optimize storage volume, CO_2 is injected into formations at depths of more than 800 meters; at this depth, CO_2 is above its critical point (the critical temperature and pressure are 31°C and 7.4 MPa, respectively) and in a supercritical state. The success of a CCS project depends on its ability to efficiently trap CO_2 in the subsurface for hundreds of years and longer, and in order to ensure security and prevent leakage, the physical and chemical mechanisms that trap CO_2 must be understood.

The focus of this work is on capillary (or residual) trapping in mildly consolidated media. Capillary trapping involves drainage and imbibition in the porous medium and is a consequence of hysteresis. CO_2 injection in a water-wet system is a drainage process during which the resident brine is displaced from the pores; during imbibition, which takes place when the resident brine returns to the formation after injection has stopped, or during an engineered waterflood, some of the injected CO_2 is trapped as a result of capillary interactions.

Capillary trapping is arguably the most advantageous form of trapping because of its high storage security (the risk of leakage into the atmosphere or of groundwater contamination is less than for hydrodynamic trapping, which relies on the integrity of a cap-rock) and relatively short time scales [Juanes et al., 2006]. The capillary trapping mechanism also has the potential to contribute more to overall trapping than both dissolution or mineral trapping mechanisms [Kumar et al., 2004]. Under specific formation and time constraints, all of the injected CO_2, can be potentially trapped by capillary forces [IPCC, 2005b]. Al Mansoori et al. [2009] showed that poorly consolidated media produced relatively low residual nonwetting phase saturations (0-15%), thus suggesting that highly consolidated media would be better suited for CO_2 injection scenarios. Yet, the saline formation used for CO_2 storage at the Sleipner CCS project off the coast of Norway consists of unconsolidated sandstone and has stored approximately 1 Megaton (Mt) of CO_2 per year since 1996 [IPCC, 2005b].

MicroCT imaging has now been used in a number of studies to explore the storage security of residually trapped nonwetting phase. Iglauer et al. [2011] measured trapped residual saturations of supercritical CO_2 of 25% in quartz sandstone cores (4.95 mm diameter, 9 mm length) and concluded that local capillary trapping is a safe and effective method of securing supercritical CO_2 in the subsurface. In larger consolidated Berea sandstone cores (diameter of 38.5 mm, length of 75.3 mm), Pentland et al. [2011] measured somewhat higher trapping capacities, that is 37% and 48% residual nonwetting phase saturation in brine-supercritical CO_2 and brine-oil experiments, respectively. More recently, Tanino and Blunt [2012] studied capillary trapping in sandstones and carbonates, in particular the dependence on pore structure. They measured the residual state established by water flooding at low capillary number and found that residual saturation decreased as conditions became less favorable for snap-off.

Our objective is to explore how CO_2 storage capacity can be optimized via capillary trapping. The results reported were obtained using proxy fluids and mildly consolidated media, and trapping was quantified using microCT imaging. The use of proxy fluids allows exploring combinations of IFT, viscosity and flow rate that are expected at reservoir conditions, but cannot be easily reproduced in laboratory experiments if supercritical CO_2 is used as the nonwetting fluid.

3.3 Background

3.3.1 Capillary, Viscous, and Gravitational Forces

In two-phase immiscible fluid systems, the capillary number (Ca) is a dimensionless number that is used to characterize relative strength of viscous to capillary forces and it is the variable that is commonly used as the predictor of trapping efficiency of the nonwetting phase. There are many different definitions of capillary number, some of which incorporate relative permeability; however, in this work, we define:

$$Ca = \frac{\text{Viscous Force}}{\text{Capillary Force}} = \frac{\mu_{INV} \cdot v_{INV}}{\sigma} \qquad \text{(eqn. 3.1)}$$

where μ_{INV} is the viscosity of the invading fluid, v_{INV} is the average pore velocity of the invading fluid and σ is the interfacial tension between the two fluids [Heiß et al., 2011; Morrow et al., 1988; Suekane et al., 2009]. The role of the invading or defending fluid changes between imbibition and drainage events.

To account for the viscosity differences between the two fluids, a second dimensionless number needs to be introduced. The mobility ratio (M) is used to compare the viscosities of the invading and defending fluids and it is defined as:

$$M = \frac{\mu_{\mathrm{INV}}}{\mu_{\mathrm{DEF}}} \qquad \text{(eqn. 3.2)}$$

where μ_{INV} represents the viscosity of the invading fluid and μ_{DEF} represents the viscosity of the defending fluid, in agreement with Lenormand et al. [1988] and Zhang et al. [2011]. Again, notice that for the same fluid pair the mobility ratio is different in drainage and imbibition because the invading fluid is the nonwetting fluid in the former case and the wetting fluid in the latter case.

The effects of gravity on the system can be quantified by the Bond number (Bo), which estimates the relative importance of gravitational to capillary forces and is typically defined as:

$$Bo = \frac{\text{Gravitational Force}}{\text{Capillary Force}} = \frac{\Delta\rho \cdot g \cdot d^2}{\sigma} \qquad \text{(eqn. 3.3)}$$

where Δρ is the density difference between the invading and defending fluids, g is the gravitational constant, and d is a representative length scale [Løvoll et al., 2005]; here, we define d to be the median bead or grain diameter. The Bond number can be plotted inversely in combination with the capillary number to identify which of the three forces (capillary, viscous, or gravitational forces) will dominate flow at the pore-scale during fluid displacement (e.g. Polak et al. [2011])

3.3.2 Impact of Capillary Number on Trapping

It is commonly accepted that the residual nonwetting phase saturation, S_R, depends on the capillary number during the imbibition stage [Blunt and Scher, 1995; Lenormand et al., 1983; Lenormand et al., 1988; Morrow et al., 1988]. A significant body of research has shown that as capillary number increases (and thus, viscous forces dominate), residual trapping of the nonwetting phase decreases; typically a dramatic decrease in S_R is observed around a critical capillary number of 10^{-5} to 10^{-6} (e.g. Chatzis and Morrow [1984]; Morrow et al. [1988]; Ding and Kantzas [2007]; Cense and Berg [2009]). This trend has been observed in many different types of consolidated porous media and is generally attributed to suppression of snap-off at larger Ca. The critical capillary number for wetting-phase trapping is generally measured in the range of 10^{-5} and 10^{-3} [Cense and Berg, 2009; Suekane et al., 2010].

However, the capillary number alone does not describe the complexity of trapping mechanisms because it does not carry information on the role played by viscous forces when they dominate, which is described by the mobility ratio. When Ca increases and viscous forces becomes more important, the displacement becomes more stable (more effective oil recovery) for $M>1$, and more unstable for $M<1$. In the petroleum engineering literature, where the amount of oil (the defending fluid) is to be minimized, a viscosity ratio greater than one is also referred to as "favorable", while the term "unfavorable" is used when the viscosity ratio is less than one because the invading phase forms fingers that decrease the efficiency of oil recovery. This terminology was first introduced and discussed by Engelberts and Klinkenberg [1951] based on their experimental findings, and they coined the term viscous fingering to describe the fact that under unfavorable conditions the invading fluid flows only through sparse preferential flow paths.

Three distinct flow regimes have been identified for a drainage process in two-dimensional (2D) micromodels: viscous fingering, capillary fingering, and stable displacement [Lenormand et al., 1988; Wang et al., 2012; Zhang et al., 2011]. These flow regimes are defined by the Ca and M values in reference to the so-called Lenormand phase diagram, wherein capillary numbers are plotted against mobility ratios on a log-log basis. However, these flow regimes have thus far only been studied with respect to the drainage process; whereas capillary trapping of nonwetting phase occurs during the imbibition process. We suggest that analogous flow regimes do indeed occur during imbibition, and the effects of both capillary number and mobility ratio of the imbibition process need to be investigated in order to accurately predict capillary trapping.

Thus, trapping cannot be predicted solely based on imbibition Ca, except if Ca is low: in this case displacement is dominated by capillary forces resulting in a percolation pattern, where viscous forces can be neglected, and exhibiting snap-off-dominated trapping. When Ca increases, viscous forces become more dominant and the front morphology (and thus trapping) is dictated by the viscosity ratio M (e.g. Lenormand et al. [1988]; Ferrari and Lunati [2013]). For $M>1$ the invading fluid is more viscous than the defending fluid, the front is stable and tends to remain compact; therefore, trapping will decrease with Ca. For $M<1$ the invading fluid is less viscous, the front is destabilized by viscous effects and thin, long fingers develop resulting in a significant amount of trapped nonwetting fluid; in this case, trapping will increase with Ca [Ferrari and Lunati, 2013].

Using an analogy to the Lenormand phase diagram, one can envision manipulating capillary numbers and mobility ratios of the imbibition process to optimize residual trapping. The ultimate goal of CO_2 sequestration is to maximize the amount of trapped CO_2 in the subsurface in order to prevent migration to the surface. A few recent studies have explored the relative effect of individual properties (interfacial tension, viscosity, flow rate, and density) on residual trapping and their findings are summarized in the following sections.

3.3.3 Impact of Interfacial Tension and Viscosity on Trapping

Increasing viscosity and interfacial tension values, simultaneously, was shown to increase residual CO_2 saturations in consolidated sandstone samples collected from a site in Alberta, Canada [Bennion and Bachu, 2005; Bennion and Bachu, 2006a; b; c]. Further investigation confirmed the trend of increasing trapped CO_2 saturation during imbibition events with increasing interfacial tension. Trapped CO_2 was also observed to increase with increasing mobility ratio (with brine as the invading fluid and supercritical CO_2 as the displaced fluid) which was varied by changing pressure and temperature conditions. Since interfacial tension and viscosity both vary with pressure, temperature, and salinity, it was not possible to isolate a potential viscosity effect, and instead the authors concluded that the increasing residual CO_2 trapping with viscosity ratio was related to the increasing interfacial tension trend. The authors stated that it would be impossible to design a supercritical CO_2 experiment that isolates interfacial tension effects from viscous effects.

Altered interfacial tension and viscosity values were also studied in experiments in unconsolidated and sintered bead packs with capillary numbers ranging from 10^{-2} to 10^{-4} [Morrow et al., 1988]. In this enhanced oil-recovery study, capillary numbers for oil mobilization were approximately an order of magnitude higher in bead packs than in consolidated sandstones; but the resulting glass bead data still followed a trend of increasing residual nonwetting phase saturation with a decreasing capillary number. Altering interfacial tension was not found to have an effect on residual trapping. Further, the effect of altered viscosity was not isolated in their study and conclusions regarding its relative effect on trapping efficiency could therefore not be determined.

3.3.4 Impact of Flow Rate on Trapping

A consensus regarding the effects of flow rate on residual trapping has yet to be reached. Previous studies have generally been conducted for a single fluid pair, and thus the effect of the viscosity ratio on trapping mentioned previously is not relevant. Blunt and Scher [1995] investigated the effects of flow rate on immiscible fluid displacement in a pore-network model for applications in oil reservoirs. They concluded that the dominant fluid displacement mechanism will change depending on flow rate due to fluid flow competition at the pore-scale. Nguyen et al. [2006] produced high residual nonwetting saturations through a numerical study of the snap-off mechanism in the capillary fingering regime. Most research supports this finding, arguing that snap-off is suppressed and mobilization is enhanced at high flow rates; however, Wildenschild et al. [2011] showed a weakly increasing relationship between residual nonwetting phase and increasing flow rate. This issue becomes more complicated at larger scales as pore-scale mechanisms compete with basin-scale flow patterns; for example, Juanes et al. [2006] simulated capillary trapping on a basin scale and predicted that supercritical CO_2 can be more effectively sequestered due to radical dispersion patterns induced by high injection flow rates.

3.3.5 Impact of Bond number on trapping

In a three-dimensional (3D) system, gravity forces must be taken into consideration as well as viscous and capillary forces. Morrow et al. [1988] demonstrated that nonwetting phase capillary trapping decreased as Bo increased (i.e. gravitational forces dominated over capillary forces) in glass bead column experiments with water-oil and air-oil systems; Bo in these systems was manipulated by using columns composed of bead packings of different diameters.

3.3.6 Motivation

The impact of capillary forces (presented in terms of fluid flow rate, viscosity, and interfacial tension) on residual trapping were initially investigated by Wildenschild et al. [2011]. Proxy fluid-pair experiments in glass bead packs showed that nonwetting phase trapping was optimized at high flow rates and with increasing nonwetting phase viscosity; however, because the trend was relatively weak, the authors concluded that further experimentation was required to substantiate these results.

To our knowledge, no additional work has been published that systematically examines both the isolated and combined impacts of the elements of Ca, M, and Bo as a means of optimizing CO_2 trapping efficiency. Further investigation is needed to bring clarity to issues related to capillary number and mobility ratio and their effect on imbibition flow regimes and residual trapping. As stated by Bachu and Bennion [2008], the effects of interfacial tension and viscosity cannot be investigated under supercritical conditions, thus we report here on experiments using proxy fluids conducted under ambient conditions.

We emphasize that the focus of this study is on the relative importance of flow mechanisms that are in effect during imbibition, i.e. during an engineered waterflood that would take place after CO_2 injection has ceased. Thus, this work complements that of Herring et al. [2013] who focused on the mechanisms in effect at the initial state of the system, i.e. after CO_2 injection (before imbibition).

3.4 Materials and Methods

3.4.1 Experimental Set-Up

All experiments were performed in two sintered soda lime glass bead cores, approximately 5.7 mm inner diameter and 57 mm tall. The cores were a mixture consisting of 35% 600 µm, 35% 850 µm and 30% 1000-1400 µm size beads. The beads were sintered to a borosilicate glass pipette column using a graphite crucible in a muffle furnace at 760^{0}C. The approximate porosity of each core was 34%. Following the terminology of Morrow et al. [1988], we will refer to this sintered glass bead core as a mildly consolidated medium.

Experiments were conducted using seven pairs of proxy fluids, chosen to obtain a range of interfacial tensions, viscosities, and flow rates that mimic the properties of supercritical CO_2 and brine encountered during CCS injection at reservoir conditions. The injection characteristics of supercritical CO_2 and experimental proxy fluids are listed in Tables 3-1 and 3-2, respectively. Approximate viscosity and fluid-fluid interfacial tension ranges of supercritical CO_2 in Table 3-1 were reported by Bachu [2003] and Bachu and Bennion [2008]. Experimental proxy fluid viscosities and fluid-fluid interfacial tensions presented in Table 3-2 were measured in the laboratory: fluid viscosities were measured using a Cannon Ubbelohde size 75 viscometer; fluid-fluid interfacial tensions were measured using a Fisher Surface Tensiometer Model 20 and a duNuoy ring.

Table 3-1. Approximate values of interfacial tension (IFT), viscosity (μ), and density (ρ) of supercritical CO_2 (Bachu, 2003; Bachu and Bennion, 2008).

	IFT with brine (mN/m)	μ (mPa-s)	ρ (kg/m^3)
Supercritical CO_2	25-50	0.025 – 0.15	200-1000

In three pairs of proxy fluids, the wetting phase consisted of potassium iodide (KI) brines (1:6 mass ratio of KI to deionized water). The solution ratio was tailored to facilitate good contrast in the x-ray tomographic images used for quantification by increasing the contrast of the wetting phase relative to the other constituents (nonwetting and solid phases). In these pairs, octane, air, and Soltrol were used as nonwetting phase. In the other four pairs of proxy fluids, Triton 100X surfactant or glycerol were added to the KI brine at different concentrations to modify the properties of the wetting phase. Triton 100X was chosen to lower the interfacial tension (IFT) between the KI brine/air proxy pair because at very low concentrations it has a significant impact on the IFT value without affecting viscosity, thus allowing us to isolate potential effects of interfacial tension on trapping. Glycerol, a water soluble visco-thickener, was used to alter the viscosity of the wetting fluid without significantly altering the IFT. All experiments with the altered wetting fluids (solutions of KI brine and Triton or glycerol) were paired with air as a nonwetting fluid.

Table 3-2. Interfacial tension (IFT), viscosity (μ), and density (ρ); and resulting imbibition capillary number (Ca), mobility ratio (M), and Bond number (Bo) for the seven experimental fluid pairs consisting of wetting (W) and nonwetting (NW) fluids.

Fluid Pair Designation	Wetting Fluid	Nonwetting Fluid	IFT (mN/m)	μ_W (mPa-s)	μ_{NW} (mPa-s)	$\Delta\rho$ (kg/m^3)	Ca	M	Bo
BA	Brine	Air	72	1.13	0.018	1079	3.5×10^{-7} - 8.6×10^{-5}	62.8	0.106
BS	Brine	Soltrol	25	1.13	4.82	286	9.9×10^{-7} - 9.9×10^{-6}	0.23	0.082
BO	Brine	Octane	37	1.13	0.540	377	6.7×10^{-7} - 6.7×10^{-6}	2.10	0.071
T1A	Triton 1	Air	37	1.13	0.018	1079	6.7×10^{-7} - 6.7×10^{-6}	62.8	0.207
T2A	Triton 2	Air	51	1.13	0.018	1079	4.9×10^{-7} - 4.9×10^{-6}	62.8	0.150
G1A	Glycerol 1	Air	66	1.86	0.018	1144	1.6×10^{-7}	102	0.123
G2A	Glycerol 2	Air	69	3.95	0.018	1206	3.1×10^{-6} - 1.3×10^{-5}	218	0.124

Experiments were conducted at standard temperature (22°C) and pressure (1 atmosphere). The sintered glass bead core was placed on top of a semi-permeable hydrophilic membrane (GE Nylon Membrane, 10µm) which prevented the passage of nonwetting fluid into the wetting fluid tubing. The core and filter paper were secured to a plastic base with a set of threaded, plastic connectors and an O-ring. A Harvard PhD Ultra Syringe pump precisely injected wetting fluid into the glass bead core during imbibition. During drainage the pump was reversed to extract the wetting fluid and draw in the nonwetting fluid from a reservoir connected to the top of the core. A schematic of the experimental set-up is shown in Figure 3-1.

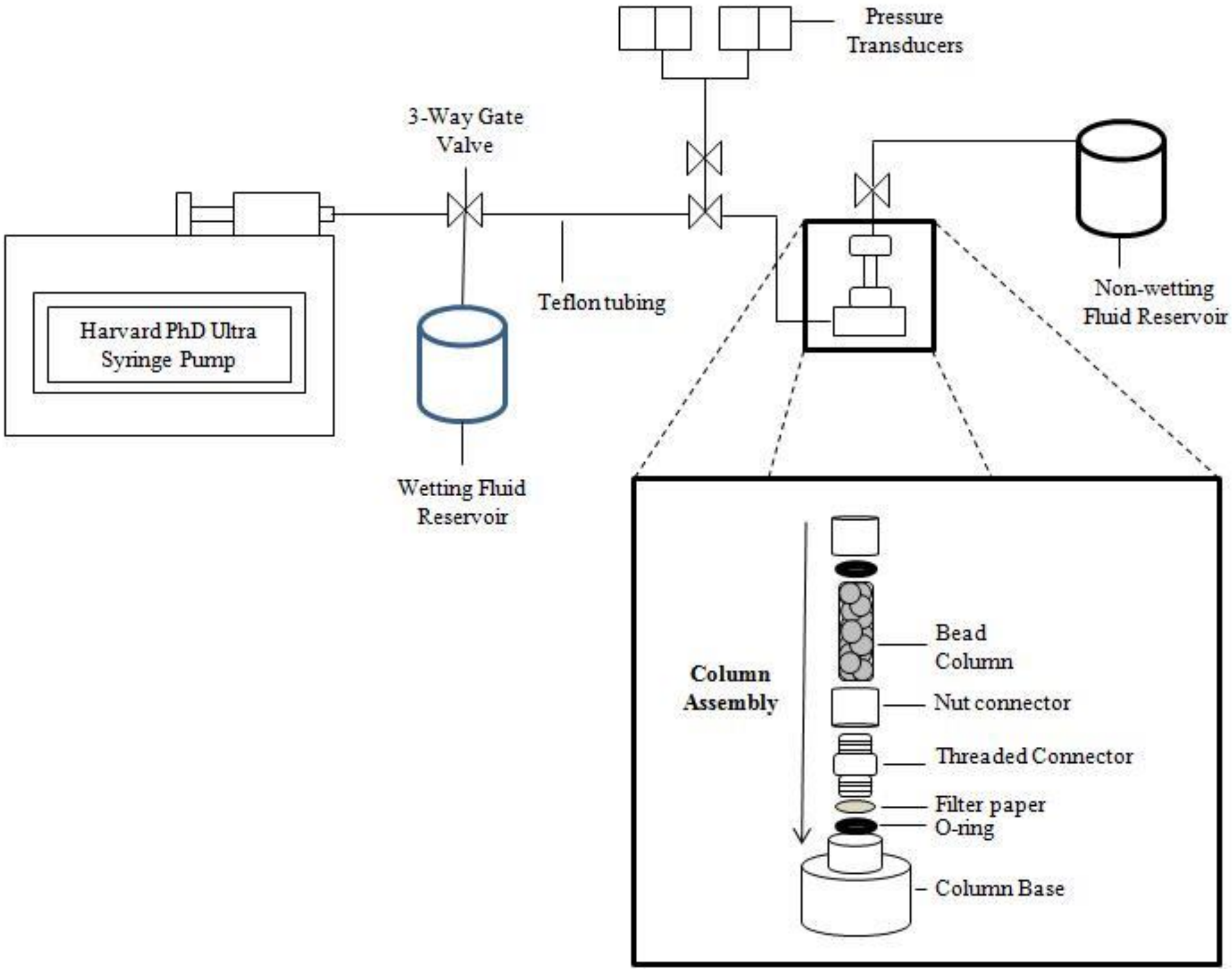

Figure 3-1. Schematic of the experimental set-up showing the syringe pump, wetting and nonwetting fluid reservoirs, pressure transducers, and sintered glass core.

The experimental set-up was assembled inside the hutch of a microCT scanner. Prior to each experiment, the glass bead core was removed from the experimental apparatus and cleaned with a series of fluids, each designed to dissolve and remove the preceding fluid from the core. The cleaning procedure required flushing the bead core first with acetone, then ethanol, next deionized water, and finally it was dried with compressed air. This procedure was repeated prior to every experiment to ensure that the starting conditions were the same for each experiment. The glass beads were assumed to comprise a water-wet system for all fluid pairs in this study.

The clean, dry bead core was placed in the core holder and secured onto the x-ray stage prior to the start of each experiment. The core was always imaged in its dry state before fluid injection to simplify data processing.

3.4.2 Experimental Procedure

After the dry scan, a primary imbibition step was performed by injecting the wetting fluid into the core at a relatively slow flow rate of 0.25 mL/hr to maximize the wetting phase saturation of the core. This process was complete once the wetting fluid reached the top of the beads and the pressure transducers indicated a zero capillary pressure. The fluids in the core were allowed to equilibrate for 15 minutes after each pumping event. Once the core had equilibrated (as indicated by approximately constant capillary pressure), the core was imaged to measure the original nonwetting-phase saturation (Figure 3-2a, S_O).

After the primary imbibition scan, the bead core was drained at a flow rate of 1 mL/hr. This step mimics the drainage of the reservoir occurring during the CO_2 injection phase (Figure 3-2b). In experiments in which the nonwetting fluids were octane or Soltrol, a line of the nonwetting fluid was connected to the top of the bead core during drainage. When the capillary pressure decreased rapidly and reached approximately -980 Pa, the drainage process was stopped. After equilibration, the core was imaged again to measure the initial nonwetting phase saturation (Figure 3-2c, S_I).

Once the drainage scan was complete, wetting fluid was re-imbibed into the core in the third step (secondary imbibition, Figure 3-2d). This step mimics an engineered waterflood or the natural migration of brine back into the drained reservoir region after CO_2 injection stopped. Fluid flow rates varied from 2-500 mL/hr, which corresponds to wetting phase capillary numbers of 10^{-6}-10^{-4} depending on the proxy pairs (Table 3-2). Four pore volumes were flushed through the core to ensure capillary trapping. After a final 15 minute equilibration period, the secondary imbibition scan was captured to establish the residual nonwetting phase saturation (Figure 3-2e, S_R).

Images were acquired using a microCT system in the School of Mechanical, Industrial and Manufacturing Engineering (MIME) at Oregon State University. The cone beam microCT system consists of a Microfocus FXE-160.20 x-ray source, a Medelex 9” image intensifier (model: HXS-93/PS), and a 2448 x 2048 pixel 16 bit CCD Point Grey Grasshopper (model: GRAS-5055M) camera. The camera had a maximum resolution of 3.45 microns and a frame rate of 15 frames per second (fps). All experiments were operated at a voltage of 100 kilovolts (kV) and a current of 78 microamps (µA). Images were collected over a rotation of 360^0 in 1440 increments, averaging 4 projections per increment. The approximate spatial resolution of each image was 13 microns per pixel and the height of the imaged region of the bead core was 20 millimeters, however, this region varied slightly due to small changes in stage location between experiments.

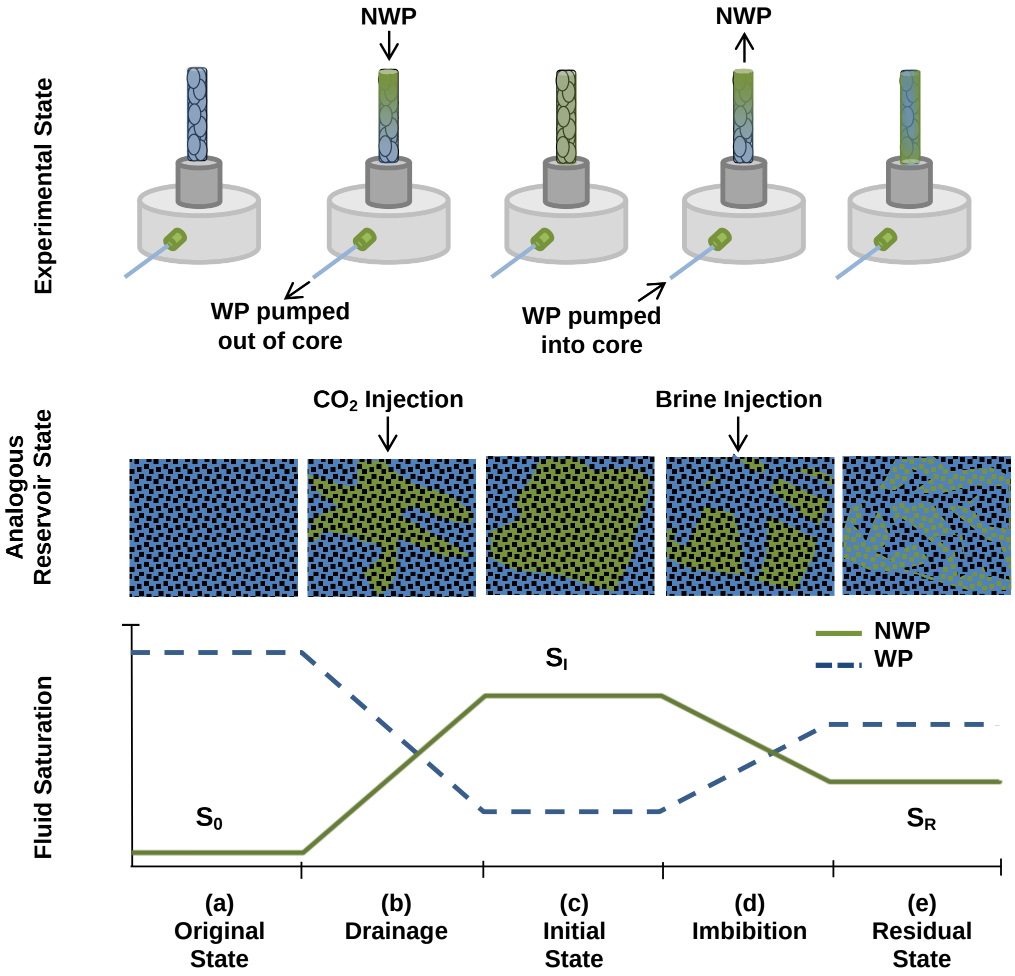

Figure 3-2. Experimental process and analogy to reservoir CO_2 sequestration processes:
(a) Original state, S_0: reservoir prior to CO_2 (nonwetting phase; NWP) injection;
(b) Drainage: reservoir during CO_2 injection;
(c) Initial state, S_I: reservoir just after CO_2 injection;
(d) Imbibition: reservoir during waterflood injection or natural groundwater flow; and
(e) Residual state, S_R: final reservoir state after migration of mobile CO_2 plume and reinvasion of the pore space by wetting phase (WP).

3.4.3 Image Processing

The images collected from each scan were saved in the form of 2D radiographs. Due to the nature of the microCT image detection configuration, the raw 2D images are inherently distorted, and were corrected using a distortion correction algorithm implemented in the Java-based program ImageJ. The distortion corrected 2D images were then reconstructed into three dimensional volumes using a cone-beam reconstruction algorithm in Octopus 8.5, a commercial software program for image reconstruction. A commercially available imaging software (Avizo Fire^{TM}) was used to prepare the 3D volumes for further analysis.

The goal of the image processing is to convert the collected grayscale images to images with three distinct phases (solid, wetting, and nonwetting fluids) for quantitative analysis. The segmented images can then be used to calculate a variety of desired system characteristics, in the present case, porosity and fluid saturations. The nonwetting saturation after the primary scan is defined as the original saturation, S_O, while the nonwetting saturation after the drainage scan is defined as the initial saturation, S_I, and the nonwetting saturation after the secondary imbibition scan is defined as the residual saturation, S_R (Figure 3-2).

Exactly the same region of the core was analyzed in all three scans within the same experiment. However, from experiment to experiment, this region changed slightly due to variation in the vertical positioning of the core inside the core holder, and of the stage. The final calculated saturations from each scan represented approximately 10 mm of the total core.

A target goal of 98% original wetting saturation was set for each experiment; however data analysis of initial experiments indicated that this goal was not consistently achieved as some air was trapped in the core initially. A trend of increasing *residual* non-wetting phase saturation with increasing *original* non-wetting phase saturation emerged [Harper, 2012]. Because many CO_2 sequestration injection sites will consist of depleted oil or gas reservoirs (e.g. Saeedi and Rezaee [2012]), this phenomenon is likely to be observed in natural settings and we chose to examine the effect, and correct for it, as opposed to trying to achieve complete original saturation (i.e. S_O=100% saturation).

Additional details regarding image reconstruction and segmentation can be found in Section 4.9, the appendix.

3.5 Results

The experimental results are discussed in terms of the wetting/nonwetting fluid pairs which are described in Table 3-2. The experiments using different nonwetting fluids are defined as Brine-Air (BA), Brine-Soltrol (BS), and Brine-Octane (BO). Experiments using altered wetting fluids (through addition of either the surfactant, Triton100X, or visco-thickener, glycerol) are defined as Triton 1-Air (T1A), Triton 2-Air (T2A), Glycerol 1-Air (G1A) and Glycerol 2-Air (G2A) in this section. We first present trapping as a function of the dimensionless ratios Ca, Bo, and M in Section 3.5.1, 3.5.2, and 3.5.3, respectively; then the individual parameters that comprise these ratios are examined in Section 3.5.4. Results of t-test analyses (using t-values as calculated by equation 3.4, see the appendix in Section 3.9) on the linear regressions of investigated parameters are presented in Table 3-3.

Table 3-3. Results of t-test analysis on the linear regressions of trapped residual nonwetting (NW) phase saturation as a function of individual fluid parameters.

Dimensionless Ratio	R^2 value of linear regression	Number of data points, n	Degrees of Freedom, d.f. (n-2)	t-value	Student's t-test two tailed p-value
Capillary Number (Ca) for M >>1	0.03	23	21	0.77	0.45
Capillary Number (Ca) for M=0.23	0.17	9	7	1.19	0.27
Mobility Ratio (M)	0.30	35	33	3.72	**<0.001**
Bond Number (Bo)	0.38	35	33	4.47	**<0.001**
Experimental Parameter					
Flow Rate	0.04	35	33	1.10	0.28
Interfacial Tension (IFT)	0.16	23	21	0.75	0.46
Wetting Phase Viscosity (μ_W)	0.03	35	33	1.07	0.29
Nonwetting Phase Viscosity (μ_{NW})	0.80	35	33	11.58	**<0.001**
Wetting/Nonwetting Phase Density Difference ($\Delta\rho$)	0.77	35	33	10.45	**<0.001**

3.5.1 S_R vs. Capillary Number

We present results in terms of residual nonwetting phase saturation (S_R) as a function of Ca. Values shown in Figures 3-3 correspond to the experimental properties (flow rate and viscosity) of the invading (wetting) fluid during secondary imbibition and range from approximately 10^{-4} to 10^{-6}. As trapping cannot be predicted solely based on Ca, in Figure 3-3 we present the data for stable (M>>1, Figure 3-3a) and unstable (M<1, Figure 3-3b) displacement in separate plots. The error bars in this and in the following figures reflect standard deviation around the average when multiple experiments were performed for the same experimental conditions.

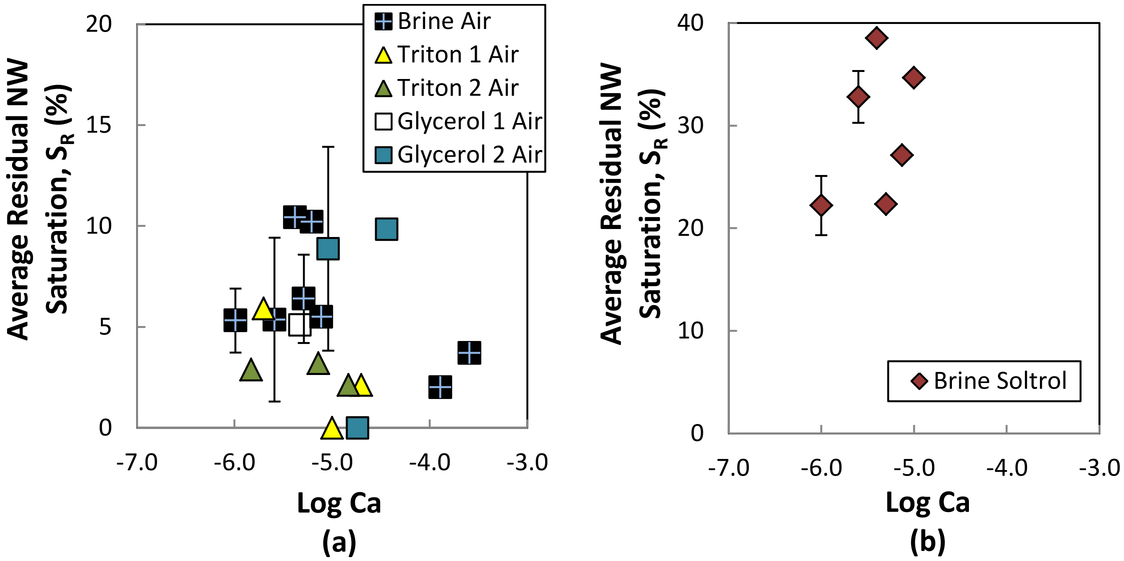

Figure 3-3. Residual nonwetting phase saturation as a function of imbibition capillary number (Ca). Fluid pairs presented in (a) exhibit mobility ratio that indicates stable displacement (M>>1); results of brine-Soltrol experiments are shown in (b), the mobility ratio of these experiments indicates unstable displacement (M=0.23).

Measured S_R vs. Ca values are presented in Figure 3-3a for fluid pairs (BA, T1A, T2A, G1A, and G2A) with a viscosity ratio of M>>1 (stable displacement), and the expected trend of decreasing S_R with increasing Ca is observed; albeit with a large amount of scatter in the data (see Table 3-2 for M values for each fluid pair). Most previously published data of S_R as a function of imbibition Ca represents consolidated rock cores, typically sandstone [Bachu and Bennion, 2008; Chatzis and Morrow, 1984; Chatzis et al., 1988; Ding and Kantzas, 2007; Kantzas et al., 2001; Shen et al., 2010; Suekane et al., 2008], and residual nonwetting phase trapping in high porosity, unconsolidated, or mildly consolidated media is not necessarily expected to follow the same trends as firmly consolidated media. Morrow et al. [1988] also reported sintered bead pack capillary trapping data that indicated a decrease in residual trapped oil with increasing capillary number (over a range of capillary numbers of 10^{-4}-10^{-2}). The scatter observed in the relationship between S_R and Ca in this study implies that Ca does not fully describe the physics dominating this experimental system, and that other experimental parameters may contribute more to trapping. A t-test analysis on the linear regression of all data points of all fluid pairs with $M>>1$ comprising residual nonwetting saturation as a function Ca results in a p-value of 0.45, indicating no statistical significance of the linear relationship between S_R and Ca for $M>>1$ (Table 3-3).

The same quantities for the experiments with a low viscosity ratio of $M=0.23$ (unstable displacement) are plotted in Figure 3-3b and a relatively high amount of residual trapping is observed. As a consequence of the unstable flow regime ($M<1$), the observed residual saturations are generally higher than other published residual saturation in glass bead packs, e.g. a maximum residual nonwetting saturation of approximately 3.5% for a water-nitrogen gas system reported by Suekane et al. [2010], and 16% for a water-oil system reported by Morrow et al. [1988]. The trend of increasing nonwetting phase saturation in the unstable viscous regime ($M=0.21$) is however, well-supported by the studies of Lenormand et al. [1988] and by simulations by Ferrari and Lunati [2013]; yet, very little experimental data exists in which the viscosity ratio of the fluids was varied during imbibition experiments. Zhang et al. [2011] and Wang et al. [2012] did study trapping using different fluid pairs with varying viscosity ratios, but focused on drainage to assess the effect these properties have on the initial saturation of CO_2 obtained during the injection stage. A t-test analysis on the linear regression of BS data points comprising residual nonwetting saturation as a function Ca (for $M=0.23$) results in a p-value of 0.27, indicating no statistical significance of the linear relationship between S_R and Ca for $M<1$ (Table 3-3).

3.5.2 S_R vs. Bond Number

Measured S_R vs. Bo values for all seven fluid pairs are presented in Figure 3-4. As Bo increases and gravitational forces become dominant over capillary forces in the experimental system, trapped nonwetting phase decreases due to the upward mobilization of the less-dense nonwetting phase. This is consistent with previous works; e.g. Morrow et al [1988]. For each fluid pair investigated in this study, the nonwetting phase was the less dense fluid, which is representative of a supercritical CO_2 sequestration operation. The relationship between residual nonwetting saturation and Bo is quantitatively more significant than the relationship between residual nonwetting saturation and Ca, with a t-test analysis on the linear regression resulting in a p-value of <0.001, indicating a highly significant relationship between Bo and S_R (Table 3-3); thus, buoyant transport must be considered in this system.

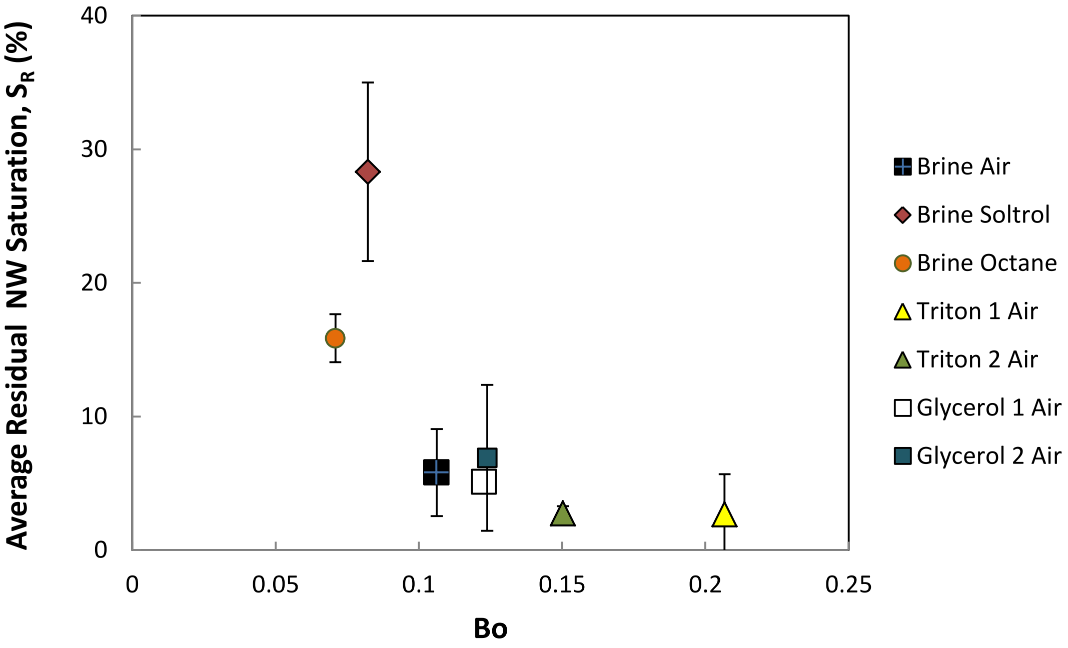

Figure 3-4. Residual nonwetting phase saturation as a function of Bond number (Bo) for all seven experimental fluid pairs.

3.5.3 S_R vs. Mobility Ratio

Mobility ratios are summarized in Table 3-2, and Figure 3-5 shows the effect of mobility ratio on residual nonwetting phase trapping. The results in Figure 3-5 demonstrate decreasing residual saturation with increasing mobility ratio; this is consistent with previous work by Bennion and Bachu [2005] who also showed decreased residual trapping with decreasing nonwetting phase viscosity. Bachu and Bennion [2008] explain that as the mobility ratio increases (lowering the nonwetting phase viscosity), the dominating and invading wetting fluid experiences less resistance while flowing in the pore space. In these instances, the wetting phase is more likely to dislodge nonwetting phase, and also will prevent nonwetting phase immobilization or trapping.

A t-test analysis on the linear regression of the relationship between M and S_R indicates high statistical significance (p-value <0.001, see Table 3-3).

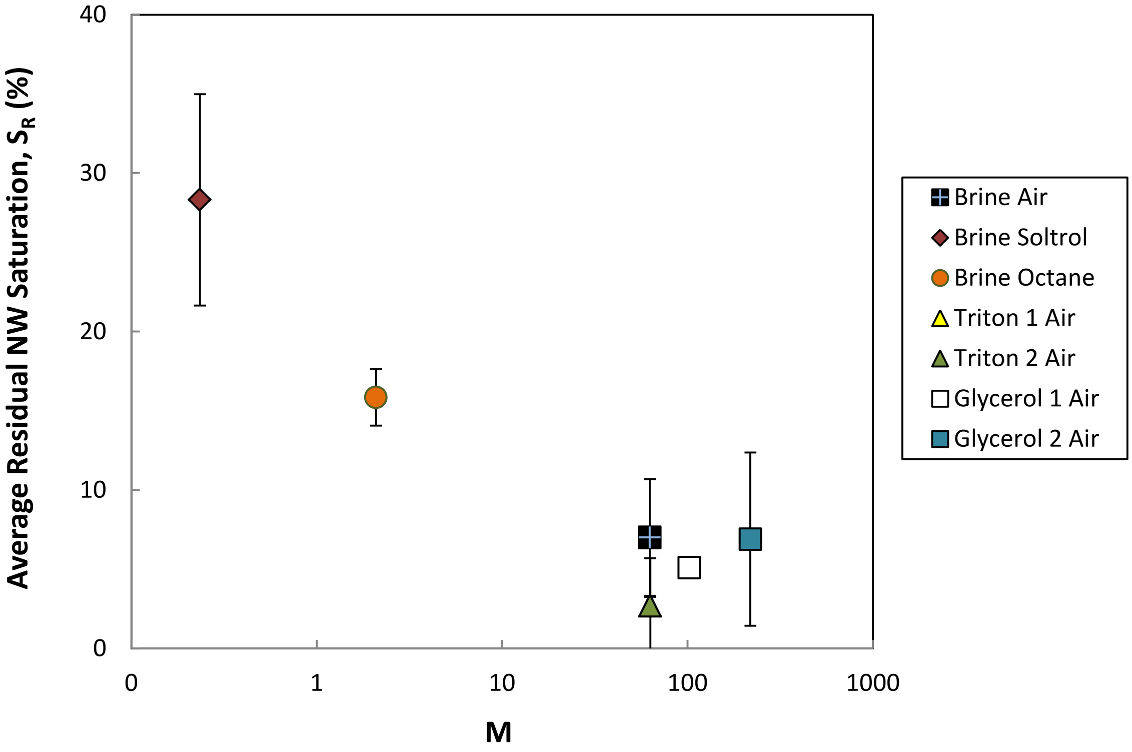

Figure 3-5. Residual nonwetting (NW) phase saturations as a function of experimental mobility ratio (M) of the imbibition process, defined as invading (wetting) phase viscosity (μ_{INV}) divided by defending (nonwetting) phase viscosity (μ_{DEF}) for seven proxy fluid pairs.

3.5.4 S_R vs. Individual Fluid Parameters

From the analysis of S_R as a function of the dimensionless ratios Ca, Bo, and M; the experimental system investigated here is dependent on all three capillary, viscous, and gravitational forces to varying extent. In this section we investigate fluid parameters individually to determine the dominant controls on the S_R response (Figure 3-6). Even if they are often used when reporting and analyzing the results of laboratory experiments, the dependence of residual trapping on these individual parameters (density, IFT, wetting and nonwetting phase viscosities) may become noisy and obscure due to the fact that, for the same value of one parameter, the interplay among the different forces may significantly vary.

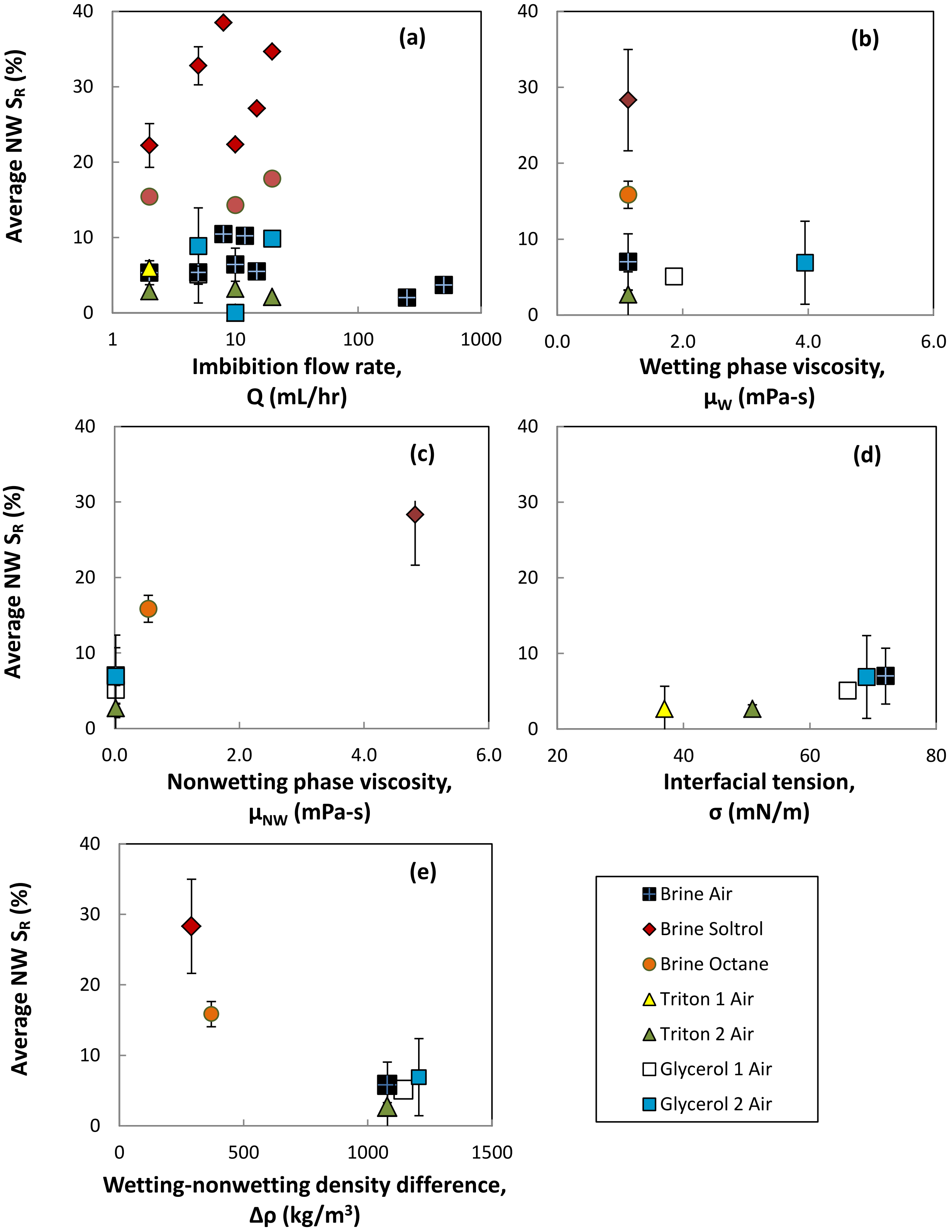

Figure 3-6. Average residual nonwetting (NW) phase saturation (S_R) as a function of (a) imbibition flow rate, (b) wetting (W) phase viscosity, (c) NW phase viscosity, (d) interfacial tension, and (e) W-NW density difference.

3.5.4.1 S_R vs. Imbibition Flow Rate

Contrary to findings of other studies (e.g. Bachu and Bennion [2008]; Herring et al. [2013]; Juanes et al. [2006]), injection flow rate did not have a distinct isolated impact on the amount of trapped residual nonwetting phase (Figure 3-6a). A t-test analysis on the linear regression of all data points of all fluid pairs comprising residual nonwetting saturation as a function of flow rate results in a p-value of 0.28, indicating no statistical significance of the relationship between the dependent (S_R) and independent (flow rate) variables (Table 3-3). If flow rate were increased beyond the parameters of this study, it is likely that desaturation of nonwetting phase would indeed occur.

3.5.4.2 S_R vs. Wetting Phase Viscosity

Glycerol was added to the brine solution to isolate the impact of wetting fluid viscosity on residual trapping. Two glycerol solutions (G1A and G2A) were prepared with viscosities that were approximately two and four times greater than the original brine solution, respectively. Figure 3-6b shows the wetting phase viscosities and the resulting S_R values.

The BA, BS, BO, T1A and T2A experiments all had wetting phase viscosities of 1.13 mPa-s. The G1A experiment had a viscosity of 1.86 mPa-s and a corresponding S_R of 5.10%, while the G2A experiment had a viscosity of 3.95 mPa-s and S_R values that ranged from 0-12.4%. Figure 3-6b shows that altering the wetting phase viscosity (by factors of two and four) does not increase trapping, i.e. the two glycerol solutions have a similar effect on residual trapping as the original brine solutions. Additionally, a t-test on the linear regression between S_R and wetting phase viscosity indicates that the relationship is not significant (p-value of 0.29, Table 3-3).

3.5.4.3 S_R vs. Nonwetting Phase Viscosity

Three nonwetting fluids with viscosities varying by two orders of magnitude were used in experiments; air at 0.018 mPa-s, octane at 0.54 mPa-s, and Soltrol at 4.82 mPa-s. Nonwetting phase S_R values are plotted against these nonwetting phase viscosities in Figure 3-6c.

All of the proxy fluid pairs using air as the nonwetting fluid (BA, T1A, T2A, G1A and G2A) resulted in low residual nonwetting phase saturations between 0-12.4%. The three BO experiments have distinctly higher residual saturations (14.3-17.8%), and at the highest nonwetting phase viscosity, the BS fluid pair produced the highest residual nonwetting saturations of 21-38.5%. Despite some noise in the data, a distinct trend of increasing nonwetting phase residual saturation with increasing nonwetting phase viscosity was observed (R^2 value of 80%). Notice, however, that the trend is dictated by the results of experiments in which the viscosity of the brine is constant (i.e. BO and BS experiments), such that the trend in nonwetting phase viscosity indeed corresponds to a trend in the viscosity ratio M, thus confirming the relevance of the latter to determine the amount of trapping.

The statistical significance of the linear regression line of nonwetting residual saturation as a function of nonwetting phase viscosity was also evaluated by a t-test. The resulting p-value was less than 0.001 (Table 3-3), indicating that the relationship between residual saturation and nonwetting phase viscosity is highly significant.

To further illustrate this trend, isosurfaces were created for the trapped nonwetting phase resulting from displacement using different nonwetting phase viscosities. Figure 3-7 shows this trapped nonwetting phase after secondary imbibition at 2 mL/hr in BA, BO and BS experiments. The residual saturations increase from 4.20% for BA to 20.9% for BS with increasing nonwetting phase viscosity, and the isosurfaces show that trapping is distributed uniformly throughout the (imaged section of the) core for all three viscosities, eliminating potential concerns about preferential flow paths that might emerge at higher nonwetting phase viscosity (or lower viscosity ratio).

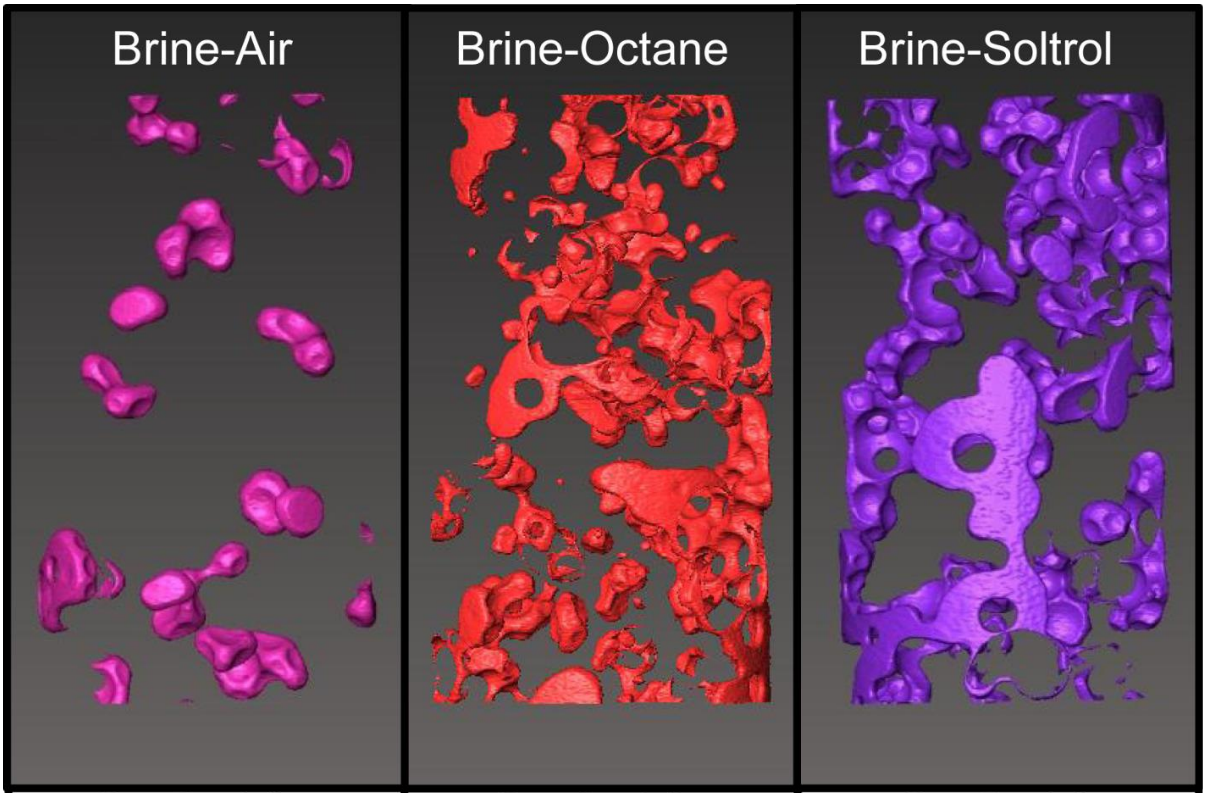

Q = 2 mL/hr σ = 72 mN/m μ_{NW} = 0.018 mPa-s Δρ = 1079 kg/m^3 S_R = 4.2%	Q = 2 mL/hr σ = 37 mN/m μ_{NW} = 0.54 mPa-s Δρ = 370 kg/m^3 S_R = 15.4%	Q = 2 mL/hr σ = 25 mN/m μ_{NW} = 4.82 mPa-s Δρ = 290 kg/m^3 S_R = 20.9%

Figure 3-7. Residual (capillary trapped) nonwetting (NW) phase isosurfaces for experiments with brine and air (BA), brine and octane (BO), and brine and soltrol (BS), for an imbibition flow rate (Q) of 2 mL/hr. Values for interfacial tension (IFT, σ), nonwetting phase viscosity (μ_{NW}), fluid pair density difference (Δρ), and residual saturation (S_R) are provided.

3.5.4.4 S_R vs. Interfacial Tension

The effect of IFT on nonwetting residual trapping (S_R) was also examined (Figure 3-6d). As stated above, wetting phase viscosity had no significant effect on trapping (Section 3.5.4.2) while nonwetting phase viscosity had a highly significant effect on trapping (Section 3.5.4.3); thus, fluid pairs with different nonwetting phase viscosity (i.e. BO and BS data) were excluded from this analysis. IFT values for the remaining five proxy fluid pairs (BA, T1A, T2A, G1A, and G2A) ranged 37 – 72 mN/m.

For systems with low IFT, capillary forces are reduced and NW phase can more easily pass through pore throats and therefore migrate through the sample; this is demonstrated by the slight increase in S_R with increasing IFT (Figure 3-6d). This trend is in agreement with Bennion and Bachu [2008] who found a modest increase in nonwetting phase trapping during imbibition with increasing IFT (note that in the experiments of Bennion and Bachu viscosity was altered simultaneously with IFT). However, the t-test analysis of the linear relationship between S_R and IFT results in a p-value of 0.46, indicating that the relationship is not statistically significant (Table 3-3).

To emphasize the necessity of consideration of fluid parameters other than IFT, isosurfaces of residually trapped nonwetting fluid are presented in Figure 3-8. The T1A and BO experiments both exhibit IFT of 37 mN/m; however, the fluid pairs exhibit distinct differences in trapped nonwetting volume and spatial arrangement; with S_R values of 5.91% and 15.4% at 2 mL/hr, and 2.12% and 17.8% a 20 ml/hr for the T1A and BO experiments, respectively. If IFT alone controlled residual trapping, then we would expect fluid pairs with the same IFT to produce similar nonwetting phase saturations; however, this was clearly not the case. Based on the lack of clear trend between S_R and IFT, as described above, we conclude that IFT alone is unable to explain the variations in residual saturations because viscous and gravity effects are important for the injection rates considered here.

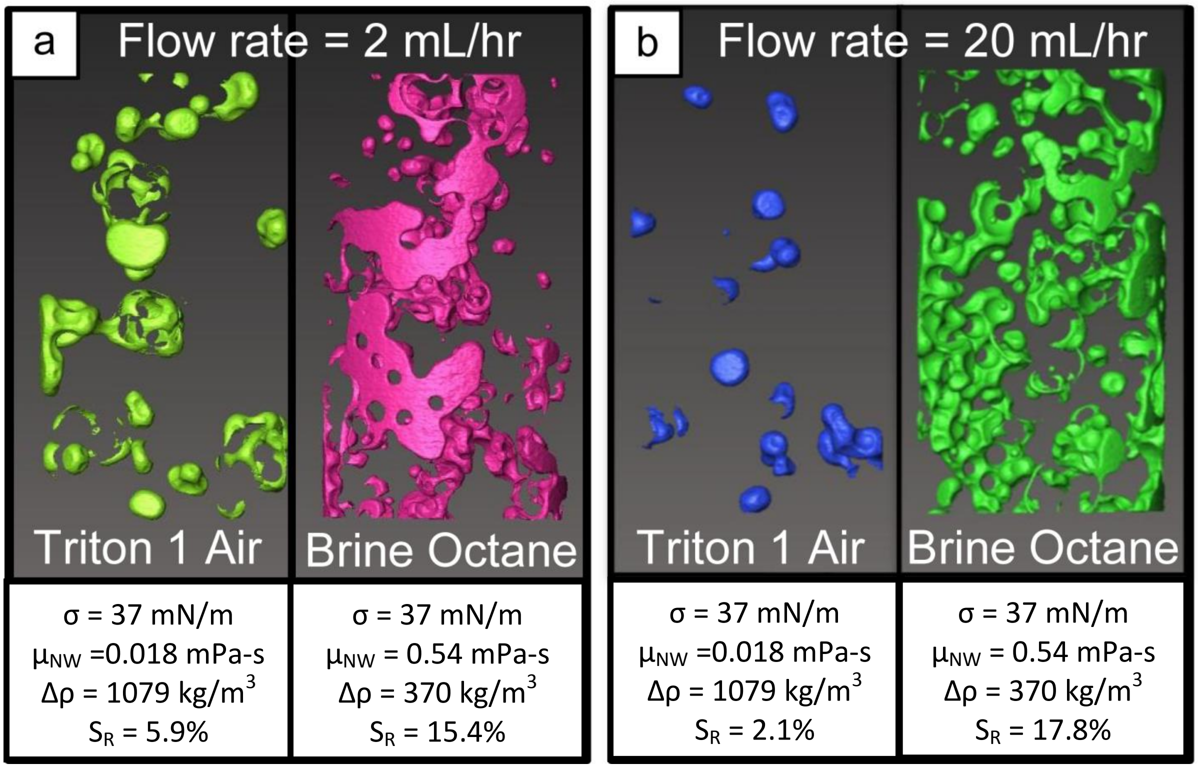

Figure 3-8. Residual (capillary trapped) nonwetting (NW) phase isosurfaces for experiments with Triton 1 and air (T1A) and brine and octane (BO), both of which exhibit an interfacial tension (IFT) of 37 mN/m. Experiments are shown for (a) flow rate of 2 mL/hr and (b) flow rate of 20 mL/hr. Values for interfacial tension (σ), nonwetting phase viscosity (μ_{NW}), fluid pair density difference (Δρ), and residual saturation (S_R) are provided.

3.5.4.5 S_R vs. Density Difference

Residual nonwetting phase saturation decreases as the difference in density between the two fluid pairs increases (Figure 3-6e). In these experiments, all nonwetting fluids were the less dense fluid of the proxy fluid pair investigated and the imbibition process was carried out in the upward vertical direction. Thus, as density difference between the fluids in each pair increases, nonwetting fluid is more likely to be mobilized upward, out of the column. This is analogous to a geologic CO_2 sequestration operation, where buoyant CO_2 will migrate upward in the storage reservoir.

A t-test analysis of the linear relationship between S_R and the wetting/nonwetting density difference results in a p-value <0.001, indicating that the relationship is strongly statistically significant (Table 3-3).

3.5.5 Discussion of the Interplay between the Three Forces

In these drainage-imbibition experiments in sintered glass bead columns, strong relationships were found between nonwetting phase residual trapping (S_R) and Bond number (Bo) and mobility ratio (M) of the experiments. When analyzing the effect of the individual parameters independently, as it is customary in many studies, nonwetting-phase viscosity and wetting/nonwetting fluid density difference appeared the most important physical parameters influencing residual trapping: volume of trapped nonwetting phase consistently increased with increasing nonwetting proxy fluid viscosity and with decreasing difference in fluid densities. Note that in these experiments nonwetting phase viscosity, density difference, and imbibition flow rate were altered by two orders of magnitude (from 0.0180 mPa-s to 4.82 mPa-s for nonwetting viscosity, 290 kg/m^3 to 1206 kg/m^3 for density difference, and 2 mL./hr to 500 mL/hr for imbibition flow rate); by comparison, viscosity of the wetting fluids were varied only between 1.13 mPa-s and 3.95 mPa-s, and IFT between 25 mN/m and 72 mN/m. The largest residual nonwetting phase saturation was approximately 40%, significantly higher than previously published saturations for sintered or loose-packed glass bead packs (e.g. Morrow et al. [1988] reported maximum S_R values of approximately 15% for Ca ranging from $10^{-4} – 10^{-2}$).

To further evaluate the dominant forces at play in the imbibition process, Figure 3-9 provides evaluation of the inverse Bond number (Bo^{-1}) and the capillary number. The product of the inverse Bond number (ratio of gravitational to viscous forces) and the capillary number (ratio of viscous to capillary forces) yields a ratio of viscous to gravitational forces (‘Bo^{-1}•Ca’); a similar analysis was previously presented by Polak et al. [2011] and Herring et al. [2014]. Since Bo is dependent on grain size, the median bead size of 850 μm was used in the Bo calculations represented by the data points in Figure 3-9. Polak et al. [2011] and Herring et al. [2014] used this type of plot to identify the relative dominance of capillary, viscous and gravitational forces. The dominance of each force is indicated by the force arrows in Figure 3-9.

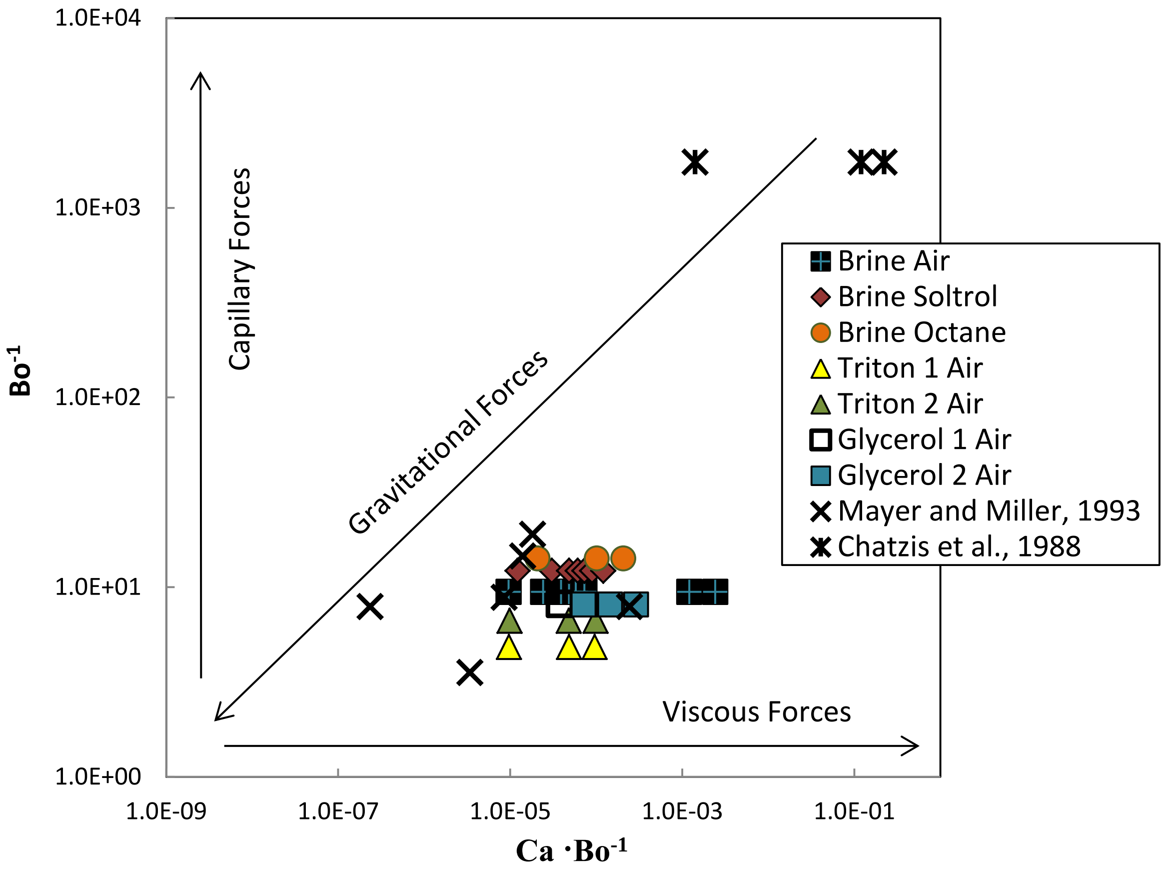

Figure 3-9. Force diagram showing the relative importance of capillary, viscous, and gravitational forces in an experimental system, with the experiments of this study (denoted as Harper et al. 2012) and two other studies from the literature presented. Inverse bond number (Bo^{-1}) represents the ratio of capillary to gravitational forces, and the product of capillary number to inverse Bond number ($Ca•Bo^{-1}$) represents the ratio of viscous to gravitational forces.

Findings from two additional fluid flow studies are also depicted in Figure 3-9. The Chatzis et al. [1988] data represents experiments conducted in consolidated sandstone cores and are located in the upper right-hand corner of the figure with relatively large Bo^{-1} and Bo^{-1}•Ca values (10^3 and 10^{-3} – 10^{-1}, respectively). The results obtained by Herring et al. [2013] in consolidated media (although not represented in Figure 3-9) show similar trends as Chatzis et al. [1988], with data located in the capillary and viscous dominated regimes. The second data set is from Mayer and Miller [1993] who performed fluid flow experiments in unconsolidated glass bead packs; the resulting Bo^{-1} and Bo^{-1}•Ca values from these experiments are located closer to our data towards the lower left-hand corner of Figure 3-9, indicating a slightly more gravity-dominated regime than our data. Our experimental results, which demonstrate significant dependence on nonwetting phase viscosity (or viscosity ratio) and wetting/nonwetting density differences (or Bond number), are perfectly complemented by Figure 3-9 which shows that our flow system spans the gravitational and viscous dominated regimes, with reduced influence due to capillarity (as is indicated by the limited effects of altering IFT).

3.6 Conclusions

The optimization of the capillary trapping mechanism was investigated by proxy fluid pair experiments in a mildly consolidated glass bead pack. Alterations were made to fluid flow rate, wetting and nonwetting fluid viscosity, nonwetting fluid density, and interfacial tension to determine the combined and individual effectiveness of these variables on residual nonwetting phase trapping efficiency.

The effects of the Capillary number on residual trapping have been extensively studied, observing, in general, that the trapped nonwetting phase will increase with decreasing capillary number. However, considering only capillary number does not provide a complete picture of the displacement process; the mobility ratio of the fluids involved also needs to be taken into account, particularly at relatively high capillary numbers, for which viscous effects dominate. In a three-dimensional (3D) system, gravitational forces must be considered as well. Our residual saturation data, which was collected from experiments that altered and isolated the individual elements of Capillary number and Bond number show that consideration of all three ratios of Ca, M, and Bo is necessary to provide a coherent explanation of the results. Contrary to other studies which show that capillary trapping is highly dependent on imbibition Ca and IFT [Bachu and Bennion, 2008], we find that our system is dominated by gravitational and viscous forces (Figure 3-9), exhibiting strong relationships between residual nonwetting phase saturation (S_R) and M and Bo. Further analysis demonstrates that nonwetting phase viscosity and wetting/nonwetting density difference are the most important factors affecting nonwetting phase capillary trapping; this shows that the most appropriate numbers to describe the flow are combination of Bo, Ca, and M. The fluid parameters which will have the most impact on capillary trapping of supercritical CO_2 in a geologic setting will likely vary, and depend on which forces dominate in a given system [Herring et al., 2014]. Therefore, it is always safer to characterize the flow by the dimensionless numbers, which describe the interplay among the forces.

Viscous forces have historically been manipulated to enhance the removal (or mobilization) of nonwetting phase fluids from formations through miscible fluid flooding events (e.g. enhanced oil recovery). However, based on the results presented here, we suggest that engineering a system in which viscous forces dominate (through alterations made to the nonwetting phase viscosity, or by altering the viscosity ratio) could also be advantageous for increased residual nonwetting phase trapping applications in mildly consolidated media, specifically geological CO_2 sequestration. Additionally, in a gravity-dominated system, consideration of difference in density between fluids must be considered.

In order to optimize the amount of CO_2 injected during a sequestration project in unconsolidated or mildly consolidated media (as for instance the Utsira formation at the Sleipner CCS injection site), alterations could be made to increase the viscosity or density of the CO_2, potentially beyond the values that can be achieved through changes in pressure and temperature in the supercritical range by using additives. Alternatively, in viscous dominated regimes, increased trapping can also be achieved by decreasing the mobility ratio of the fluids, i.e. by decreasing the viscosity of the wetting phase, but this is not feasible for reservoir brine. The use of CO_2 with engineered viscosity is already being explored, for instance nanoparticle-stabilized CO_2 for EOR [Worthen et al., 2012]. Decreasing the difference in density between CO_2 and brine can be achieved by increasing CO_2 density; this could be accomplished by increasing the pressure and/or decreasing the temperature of CO_2 injection [Bachu, 2003].

3.7 Acknowledgements

We thank Gabriel Iltis of Oregon State University for help with data processing. This work was made possible by funding from the Department of Energy (DOE) Basic Energy Sciences Award # DE-FG02-11ER16277 and from the National Science Foundation (NSF) EAR-0941299. Wildenschild was partially supported by a grant from the Los Alamos National Laboratory's LDRD program (project 20100025DR).

3.8 References

Al Mansoori, S., S. Iglauer, C. H. Pentland, B. Bijeljic, and M. J. Blunt (2009), Measurements of Non-Wetting Phase Trapping Applied to Carbon Dioxide Storage, Energy Procedia, 1(1), 3173-3180.

Bachu, S. (2003), Screening and ranking of sedimentary basins for sequestration of CO_2 in geological media in response to climate change, Environmental Geology, 44(3), 277-289.

Bachu, S., and D. B. Bennion (2008), Interfacial Tension between CO_2, Freshwater, and Brine in the Range of Pressure from (2 to 27) MPa, Temperature from (20 to 125) °C, and Water Salinity from (0 to 334 000) mg•L−1, Journal of Chemical & Engineering Data, 54(3), 765-775.

Bachu, S., and B. Bennion (2008), Effects of in-situ conditions on relative permeability characteristics of CO_2-brine systems, Environmental Geology, 54(8), 1707-1722.

Bennion, B., and S. Bachu (2005), Relative permeability characteristics for supercritical CO_2 displacing water in a variety of potential sequestration zones, paper presented at SPE Annual Technical Conference and Exhibition, Society of Petroleum Engineers.

Bennion, D. B., and S. Bachu (2006a), Supercritical CO_2 and H2S-Brine Drainage and Imbibition Relative Permeability Relationships for Intercrystalline Sandstone and Carbonate Formations, paper presented at SPE Europec/EAGE Annual Conference and Exhibition, Society of Petroleum Engineers.

Bennion, D. B., and S. Bachu (2006b), Dependence on Temperature Pressure and Salinity of the IFT and Relative Permeability Displacement Characteristics of CO_2 Injected in Deep Saline Aquifers, paper presented at SPE Annual Technical Conference and Exhibition, Society of Petroleum Engineers.

Bennion, D. B., and S. Bachu (2006c), The impact of interfacial tension and pore size distribution/capillary pressure character on CO_2 relative permeability at reservoir conditions in CO_2-brine systems, paper presented at SPE/DOE Symposium on Improved Oil Recovery, Society of Petroleum Engineers.

Blunt, M. J., and H. Scher (1995), Pore-level modeling of wetting, Physical Review E, 52(6), 6387.

Cense, A. W., and S. Berg (2009), The Viscous-Capillary Paradox in 2-Phase Flow in Porous Media, paper presented at International Symposium of the Society of Core Analysts, Shell International Exploration & Production, Noordwijk, The Netherlands, 27-30 September, 2009.

Chatzis, I., and N. R. Morrow (1984), Correlation of capillary number relationships for sandstone, Journal Name: SPEJ, Soc. Pet. Eng. J.; (United States); Journal Volume: 24:5, Medium: X; Size: Pages: 555-562.

Chatzis, I., M. S. Kuntamukkula, and N. R. Morrow (1988), Effect of capillary number on the microstructure of residual oil in strongly water-wet sandstones, Journal Name: SPE (Society of Petroleum Engineers) Reserv. Eng.; (United States); Journal Volume: 3:3, Medium: X; Size: Pages: 902-912.

Ding, M., and A. Kantzas (2007), Capillary number correlations for gas-liquid systems, 6 pp., Society of Petroleum Engineers, Calgary, CANADA.

Engelberts, W., and L. Klinkenberg (1951), Laboratory experiments on the displacement of oil by water from packs of granular material, paper presented at Proceedings 3rd World Petroleum Congress, The Hague.

Ferrari, A., and I. Lunati (2013), Direct numerical simulations of interface dynamics to link capillary pressure and total surface energy, Advances in Water Resources, 57, 19-31.

Harper, E. J. (2012), Optimization of Capillary Trapping for CO_2 Sequestration in Saline Aquifers, Oregon State University, Corvallis, Oregon.

Heiß, V., I. Neuweiler, S. Ochs, and A. Färber (2011), Experimental investigation on front morphology for two-phase flow in heterogeneous porous media, Water Resources Research, 47(10), W10528.

Herring, A. L., L. Andersson, S. Schlüter, A. Sheppard, and D. Wildenschild (2014), Efficiently Engineering Pore-Scale Processes: Force Balance and Topology During Nonwetting Phase Trapping in Porous Media, In prep.

Herring, A. L., E. J. Harper, L. Andersson, A. Sheppard, B. K. Bay, and D. Wildenschild (2013), Effect of fluid topology on residual nonwetting phase trapping: Implications for geologic CO_2 sequestration, Advances in Water Resources, 62, 47-58.

Iglauer, S., A. Paluszny, C. H. Pentland, and M. J. Blunt (2011), Residual CO_2 imaged with X-ray micro-tomography, Geophysical Research Letters, 38(21), L21403.

IPCC (2005), IPCC special report on carbon dioxide capture and storage.

Juanes, R., E. J. Spiteri, F. M. Orr, Jr., and M. J. Blunt (2006), Impact of relative permeability hysteresis on geological CO_2 storage, Water Resour. Res., 42(12), W12418.

Kantzas, A., M. Ding, and J. Lee (2001), Residual gas saturation revisited, SPE Reservoir Evaluation & Engineering, 4(06), 467-476.

Kumar, A., M. Noh, G. Pope, K. Sepehrnoori, S. Bryant, and L. Lake (2004), Reservoir simulation of CO_2 storage in deep saline aquifers, paper presented at SPE/DOE Symposium on Improved Oil Recovery, Society of Petroleum Engineers.

Lenormand, R., C. Zarcone, and A. Sarr (1983), Mechanisms of the displacement of one fluid by another in a network of capillary ducts, Journal of Fluid Mechanics, 135, 337-353.

Lenormand, R., E. Touboul, and C. Zarcone (1988), Numerical models and experiments on immiscible displacements in porous media, Journal of Fluid Mechanics, 189, 165-187.

Løvoll, G., Y. Méheust, K. J. Måløy, E. Aker, and J. Schmittbuhl (2005), Competition of gravity, capillary and viscous forces during drainage in a two-dimensional porous medium, a pore scale study, Energy, 30(6), 861-872.

Mayer, A. S., and C. T. Miller (1993), An experimental investigation of pore-scale distributions of nonaqueous phase liquids at residual saturation, Transp Porous Med, 10(1), 57-80.

Morrow, N. R., I. Chatzis, and J. T. Taber (1988), Entrapment and mobilization of residual oil in bead packs, Journal Name: SPE (Society of Petroleum Engineers) Reserv. Eng.; (United States); Journal Volume: 3:3, Medium: X; Size: Pages: 927-934.

Nguyen, V. H., A. P. Sheppard, M. A. Knackstedt, and W. Val Pinczewski (2006), The effect of displacement rate on imbibition relative permeability and residual saturation, Journal of Petroleum Science and Engineering, 52(1-4), 54-70.

Pentland, C. H., R. El-Maghraby, A. Georgiadis, S. Iglauer, and M. J. Blunt (2011), Immiscible Displacements and Capillary Trapping in CO_2 Storage, Energy Procedia, 4, 4969-4976.

Polak, S., Y. Cinar, T. Holt, and O. Torsæter (2011), An experimental investigation of the balance between capillary, viscous, and gravitational forces during CO_2 injection into saline aquifers, Energy Procedia, 4, 4395-4402.

Saeedi, A., and R. Rezaee (2012), Effect of residual natural gas saturation on multiphase flow behaviour during CO< sub> 2</sub> geo-sequestration in depleted natural gas reservoirs, Journal of Petroleum Science and Engineering, 82, 17-26.

Shen, P., B. Zhu, X.-B. Li, and Y.-S. Wu (2010), An Experimental Study of the Influence of Interfacial Tension on Water–Oil Two-Phase Relative Permeability, Transport in Porous Media, 85(2), 505-520.

Suekane, T., T. Nobuso, S. Hirai, and M. Kiyota (2008), Geological storage of carbon dioxide by residual gas and solubility trapping, International Journal of Greenhouse Gas Control, 2(1), 58-64.

Suekane, T., N. Zhou, T. Hosokawa, and T. Matsumoto (2010), Direct Observation of Trapped Gas Bubbles by Capillarity in Sandy Porous Media, Transport in Porous Media, 82(1), 111-122.

Suekane, T., N. H. Thanh, T. Matsumoto, M. Matsuda, M. Kiyota, and A. Ousaka (2009), Direct measurement of trapped gas bubbles by capillarity on the pore scale, Energy Procedia, 1(1), 3189-3196.

Tanino, Y., and M. J. Blunt (2012), Capillary trapping in sandstones and carbonates: Dependence on pore structure, Water Resources Research, 48(8).

Wang, Y., C. Zhang, N. Wei, M. Oostrom, T. W. Wietsma, X. Li, and A. Bonneville (2012), Experimental study of crossover from capillary to viscous fingering for supercritical CO_2–water displacement in a homogeneous pore network, Environmental Science & Technology, 47(1), 212-218.

Wildenschild, D., R. T. Armstrong, A. L. Herring, I. M. Young, and J. William Carey (2011), Exploring capillary trapping efficiency as a function of interfacial tension, viscosity, and flow rate, Energy Procedia, 4, 4945-4952.

Worthen, A., H. Bagaria, Y. Chen, S. L. Bryant, C. Huh, and K. P. Johnston (2012), Nanoparticle Stabilized Carbon Dioxide in Water Foams for Enhanced Oil Recovery, paper presented at SPE Improved Oil Recovery Symposium, Society of Petroleum Engineers.

Zhang, C., M. Oostrom, T. W. Wietsma, J. W. Grate, and M. G. Warner (2011), Influence of Viscous and Capillary Forces on Immiscible Fluid Displacement: Pore-Scale Experimental Study in a Water-Wet Micromodel Demonstrating Viscous and Capillary Fingering, Energy & Fuels, 25(8), 3493-3505.

3.9 Appendix

3.9.1 Materials and Methods

All of the primary imbibition, drainage and secondary imbibition scans were aligned to the dry scan such that the wetting and nonwetting fluid phases could be more easily isolated from the glass beads, which remain constant throughout each phase of the experiment. After the images were aligned, the reconstructed volumes were converted from 16-bit grayscale images (with voxel values ranging from 0 to 65535) to trinary segmented images in which each voxel is assigned a value of 0, 1 or 2, thus making the phases (and thereby wetting and nonwetting fluid saturations) more easily quantifiable.

To accurately and reliably threshold (and thus segment) the images, the upper and lower intensity values of the wetting and nonwetting fluids were first defined. In the following we refer to the dry scan as the “dry” volume and the primary imbibition, drainage, and secondary imbibition scans as the “wet” volumes. Figure 3-10 is a sample histogram showing voxel intensity information from example dry and wet scans. Voxel values represent x-ray absorption intensity and appear in the histogram according to the frequency in which they appear in each volume.

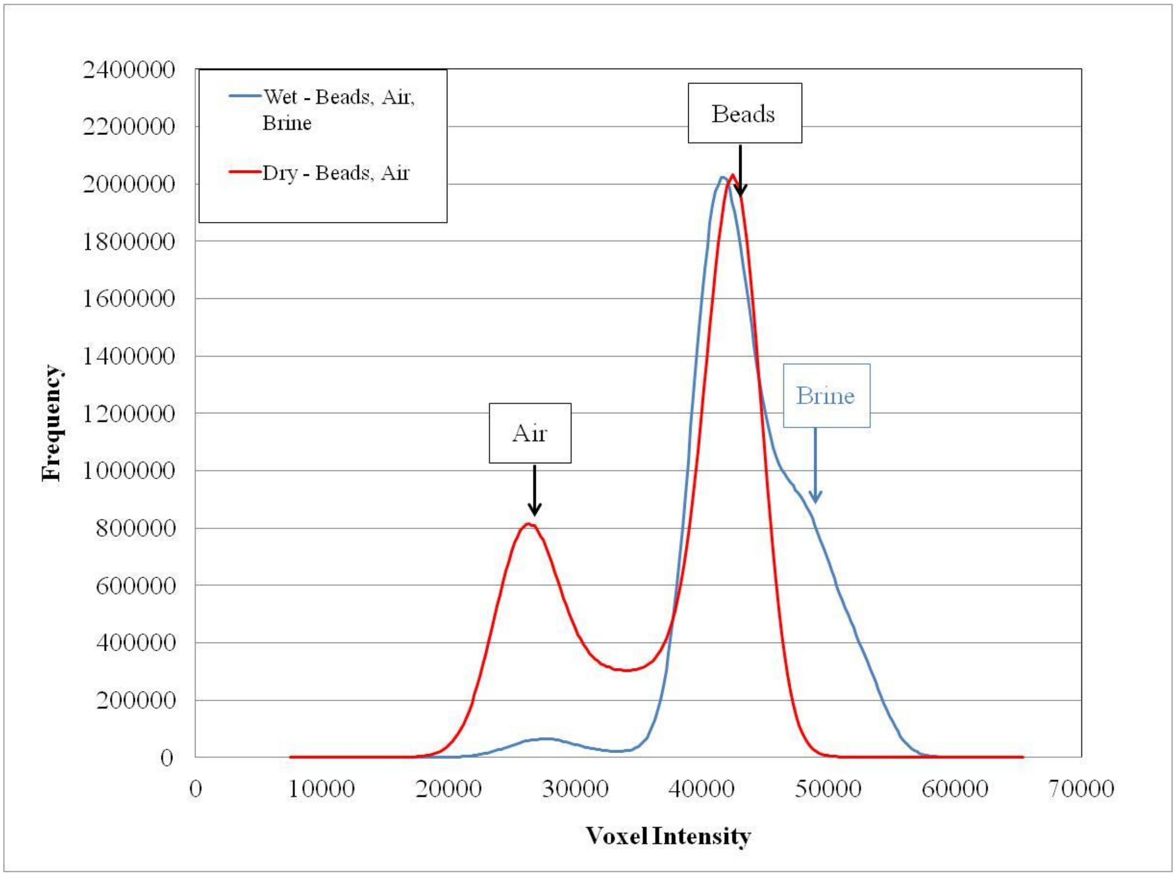

Figure 3-10. Sample histogram containing voxel intensity values and the frequency in which they occur in a dry and wet grayscale volume.

The dry volume, containing only nonwetting phase (air) and glass beads, has two distinct peaks, whereas the wet volume, containing nonwetting phase (air), wetting phase (brine) and glass beads, has three less well-defined peaks as shown by the histogram. The image threshold boundaries (i.e. binary limits) are associated with the first local minima of each curve (at approximately 34000 voxel intensity for the dry and wet scans in Figure 3-10).

The threshold boundaries for segmentation should be selected based on the identified local minima from image histograms. However, for our data, minima identification from a histogram does not produce accurately segmented images due to noise in the transition areas between the nonwetting, wetting and solid phases. This is evident in Figure 3-11 which shows a sample reconstructed grayscale image and a profile of the intensity values across the identified line. The resulting intensity profile shows that the difference between the intensity values associated with solid phase and wetting phase are not as distinct as the difference between the nonwetting phase and the solid phase.

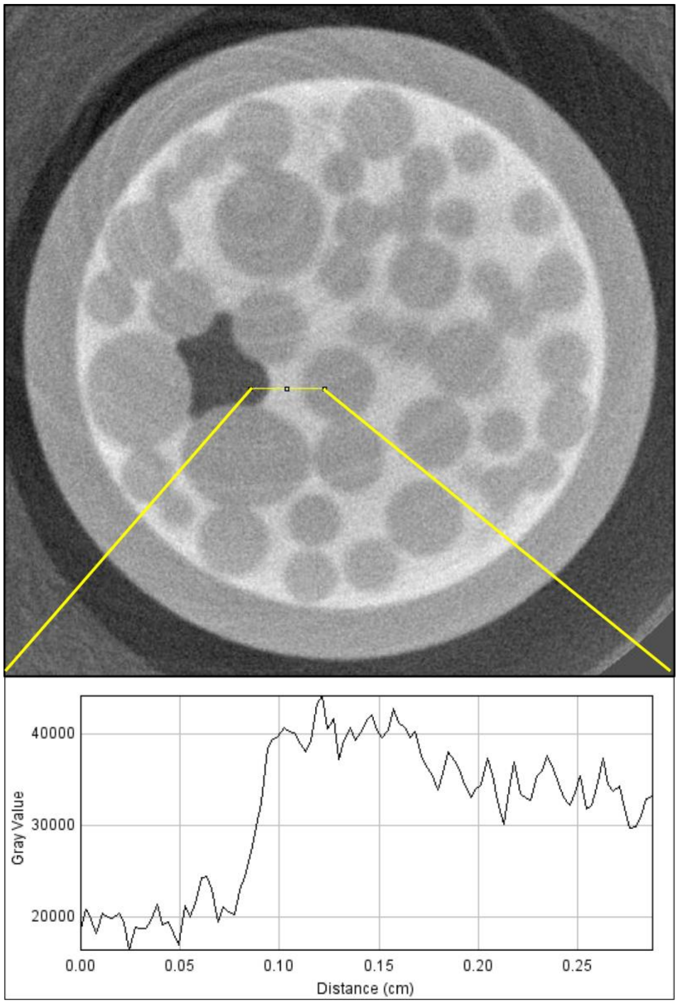

Figure 3-11. Plot profile of sample slice indicating the noise between the boundaries of the nonwetting, solid and wetting phases

Due to the ambiguity between the phases, the solid phase and wetting phase can potentially be misidentified during segmentation when only the local minima of the histogram are utilized ("*histogram minima segmentation"* method). Alternately, the local minima were manually located and adjusted to identify *only* the glass beads in the dry volume, and *all* of the wetting phase and some of the glass beads in the remaining wet volumes. This method ("*overestimation segmentation"*), while overestimating the location of the local minima slightly, ensured that the nonwetting phase was completely isolated in both the dry and wet images, thus reducing the possibility of misidentified phases and error during segmentation and, ultimately, in the final results. The difference between the two thresholding methods is shown by a comparison of two final segmented images of the same slice, along with the original grayscale image, in Figure 3-12.

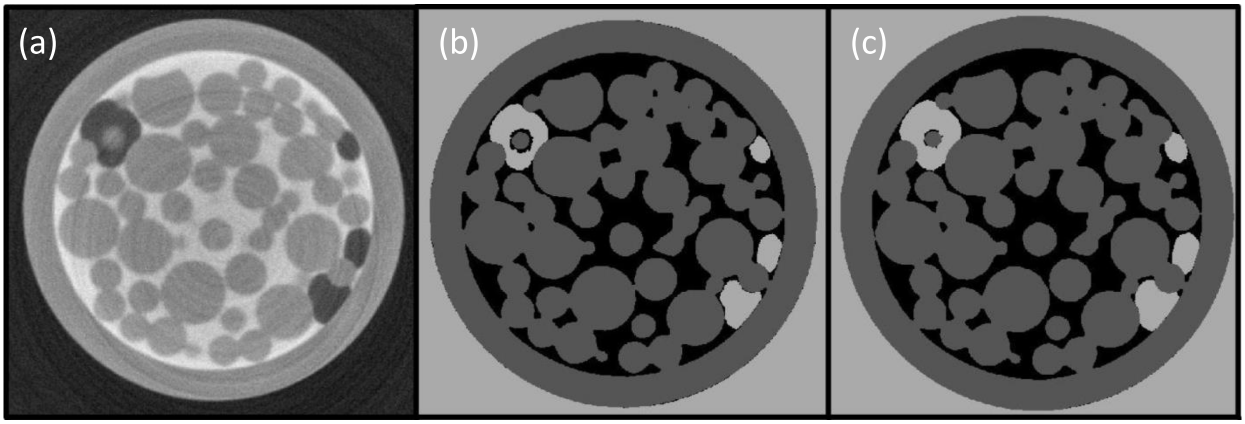

Figure 3-12. A grayscale image (a) segmented by both (b) the histogram minima segmentation method, and (c) the overestimation segmentation method.

An isolated glass bead in the upper left hand corner of the grayscale image in Figure 3-12a is surrounded by nonwetting phase in black (air). However, the histogram minima method in the middle image of Figure 3-12 misidentifies the phase surrounding the isolated bead as wetting phase (brine) shown in black. The final image (Figure 3-12c) is an example of the overestimation segmentation method. This method produced a more accurate nonwetting, wetting and solid phase segmentation.

All of the volumes were median filtered to remove noise in the data prior to being segmented. Once the dry and wet volumes were binarized, solid phase and the oversegmented nonwetting phase was combined to create an image with each phase being assigned a value of 0, 1, 2 or 3. The volumes are then processed to reassign oversegmented voxels to the correct value associated with the solid phase. A final segmented image with three distinct phases is thus produced.

After segmentation, the extra space surrounding the glass core was removed from the image. The remaining pixels were labeled and the total number of voxels associated with each of the three markers: glass beads, wetting phase and nonwetting phase were calculated.

3.9.2 Statistical Analysis

Linear relationships between residual nonwetting phase saturation and individual fluid parameters are evaluated by a two-tailed student's t-test, where the t-value is determined by Equation 3.4:

$$\boldsymbol{t = R\sqrt{\frac{n-2}{1-R^2}}} \qquad \textbf{(eqn. 3.4)}$$

where R^2 is the coefficient of regression of the linear trendline and n is the number of data points comprising the data set. In this study, a p-value of <0.001 is considered to be a strongly significant correlation.

Chapter 4. Efficiently Engineering Pore-Scale Processes: The Role of Force Dominance and Topology during Nonwetting Phase Trapping in Porous Media

Anna L. Herring[1], Linnéa Andersson[1], Steffen Schlüter[1,2], Adrian Sheppard[3], and Dorthe Wildenschild[1]

[1]School of Chemical, Biological and Environmental Engineering, Oregon State University, Corvallis, OR 97331, USA
[2]Helmholtz-Centre for Environmental Research-UFZ, Department of Soil Physics, Halle, Germany
[3]Department of Applied Mathematics, Research School of Physics and Engineering, Australian National University, Canberra, ACT 0200, Australia

Advances in Water Resources, Elsevier Ltd.
The Boulevard, Langford Lane, Kidlington, Oxford OX5 1GB, UK
Submitted August 22, 2014

4.1 Abstract

We investigate trapping of a nonwetting (NW) phase, air, within Bentheimer sandstone cores during drainage-imbibition flow experiments, as quantified on a three dimensional (3D) pore-scale basis via x-ray computed microtomography (x-ray CMT). The wetting (W) fluid in these experiments was deionized water doped with potassium iodide (1:6 by weight). We interpret these experiments based on the capillary-viscosity-gravity force dominance exhibited by the Bentheimer-air-brine system and compare to a wide range of previous drainage-imbibition experiments in different media and with different fluids. From this analysis, we conclude that viscous and capillary forces dominate in the Bentheimer-air-brine system as well as the sandstone-CO_2-brine system. In addition, we further develop the relationship between initial (post-drainage) NW phase connectivity and residual (post-imbibition) trapped NW phase saturation, while also taking into account initial NW phase saturation and imbibition capillary number. We quantify NW connectivity via a topological measure as well as by a statistical percolation metric. These metrics are evaluated for their utility and appropriateness in quantifying NW connectivity within porous media. Here, we find that there is a linear relationship between initial NW connectivity (as quantified by the normalized Euler number, $\hat{\chi}$) and capillary trapping efficiency; for a given imbibition capillary number, capillary trapping efficiency (residual NW saturation normalized by initial NW saturation) can decrease by up to 60% as initial NW phase connectivity increases from low connectivity ($\hat{\chi} \approx 0$) to very high connectivity ($\hat{\chi} \approx 1$). We propose that multiphase fluid-porous medium systems can be efficiently engineered to achieve a desired residual state (optimal NW phase saturation) by considering the dominant forces at play in the system along with the impacts of NW phase topology within the porous media, and we illustrate these concepts by considering supercritical CO_2 sequestration scenarios.

4.2 Introduction

During immiscible multiphase flow, drainage is the process of nonwetting (NW) fluid invading the pore space and displacing wetting (W) fluid, and imbibition is the process of W fluid invading the pore space and displacing NW fluid. Many engineered processes in the subsurface require fundamental understanding of drainage and imbibition processes and the resulting NW phase capillary trapping; for example, during oil recovery operations, remediation of nonaqueous phase liquid (NAPL) contaminants in the subsurface, and geologic sequestration of carbon dioxide (CO_2). In these examples, water is generally considered to be the W phase; while oil, NAPL, or CO_2 are considered to be the NW phase. Although there are abundant exceptions to this generality (e.g. intermediate-wet or oil-wet media), in this work we refer to water as the wetting phase for simplicity and consistency with previous work. In oil recovery and NAPL remediation processes the system already exists in the initial (post-drainage) state, i.e. both water and NW fluid (oil or NAPL) are already present in the system, and the bulk of previous research has focused on how to alter the imbibition (water flood) process to mobilize the maximum amount of trapped NW phase. Geologic CO_2 sequestration differs from oil recovery and NAPL remediation processes because both the drainage (i.e. CO_2 injection) and imbibition (i.e. water chase or groundwater flow) processes may be engineered, and the overall aim of the process is to trap, rather than mobilize, NW phase in the pore space of the geologic medium. Comparison between different studies and applications is complicated because fluid properties (e.g. density, viscosity, interfacial tension), medium properties (grain and pore size distributions, pore space connectivity, etc.), and flow properties (engineered injection or natural groundwater flow rates) vary widely depending on the application in question.

Recent focus on CO_2 sequestration as a global climate change mitigation strategy has prompted renewed study into the phenomena of capillary trapping in porous media (e.g. Juanes et al. [2006], Al Mansoori et al.[2010], Akbarabadi and Piri [2013], Andrew et al. [2013], among others). Capillary trapping of CO_2, wherein CO_2 is trapped by capillary forces in the pore bodies of a porous medium is a relatively secure form of trapping, as compared to “structural” or “hydrodynamic” trapping, where the buoyant CO_2 is contained by an impermeable caprock; in addition, capillary trapping occurs on relatively short timescales, as compared to dissolution trapping or mineral trapping [IPCC, 2005]. Thus, maximization of capillary trapping is important to ensure a safe and stable geologic carbon sequestration operation. Previous work has investigated NW phase capillary trapping over a wide range of fluid pairs, media types, and flow conditions for oil recovery and NAPL remediation applications. The results of these studies could greatly enhance fundamental knowledge that would benefit CO_2 sequestration studies if the results are appropriately compared and characterized. CO_2 is in a supercritical state at sequestration reservoir operations; relatively small variations in pressure, temperature, and salinity of the W phase have significant effects on the CO_2 density, CO_2 viscosity, and interfacial tension exhibited by the supercritical CO_2-brine system [Bachu and Bennion, 2008; Bachu and Bennion, 2009]. The variability of fluid properties complicates predictions of flow patterns and displacement mechanisms. Further, it has been shown that the initial (post-drainage) state of the reservoir has a substantial impact on the amount of residual capillary trapped NW phase present in the system after imbibition [Akbarabadi and Piri, 2012; Herring et al., 2013]. However, experimental work with supercritical fluids is a non-trivial exercise, necessitating methods to approximate supercritical conditions with ambient experiments; Herring et al. [2014] demonstrated that ambient condition micromodels were able to accurately predict the flow regime for a supercritical CO_2 drainage process in sandstone cores through application of a dimensional analysis.

We explore capillary trapping of NW phase from two perspectives. First, we investigate how consideration of the dominant forces at play via the pore-scale force balance in a system allows for comparison and better understanding of results from a wide range of experiments. The second study area results from the unique ability to engineer the drainage (CO_2 injection) process, and thus the initial (i.e. post-drainage) state. To this end, we use three dimensional (3D) metrics which can be used to describe NW fluid topology (connectivity) within porous media. In particular, we develop the relationship between initial NW fluid connectivity and the residual state of a system which was first investigated by Herring et al. [2013], with new analysis of a high quality data set collected via x-ray computed microtomography (x-ray CMT) experiments performed at the Advanced Photon Source at Argonne National Laboratory. Finally, we provide physical interpretation of these relationships.

Consideration of pore scale forces and fluid topology allow drainage and imbibition processes to be efficiently engineered to provide favorable residual conditions. Geologic CO_2 sequestration scenarios are used as an example to illustrate these concepts.

4.3 Background

4.3.1Pore scale forces

Considerable previous research has been conducted on the topic of residual (i.e. capillary trapped) NW saturation in porous media, with many different W and NW fluids, and in different media. To facilitate characterization of fluid flow over a range of properties, the experiments discussed in this work are characterized by the dimensionless ratios of capillary number (Ca) and Bond number (Bo).

Ca has been presented in several different forms, and has traditionally been defined from an oil extraction standpoint [Cense and Berg, 2009; Chatzis and Morrow, 1984; Jamaloei et al., 2012]. In general, Ca describes the balance between viscous forces and capillary forces with respect to the invading fluid (as opposed to the defending fluid). In this work, Ca is defined as:

$$Ca = \frac{\text{Viscous Force}}{\text{Capillary Force}} = \frac{\mu_{\text{INV}} v_{\text{INV}}}{\sigma} = \frac{\mu_{\text{INV}} \frac{Q}{A \cdot \eta}}{\sigma} \qquad \text{(eqn. 4.1)}$$

where μ_{INV} is the invading phase viscosity [mPa•s], v_{INV} is the invading phase Darcy velocity [m/s], and σ is the interfacial tension between the invading and defending fluid. The invading phase velocity is computed as the volumetric flow rate Q [m^3/s] divided by the cross-sectional area A [m^2] of the porous medium and the porosity η [-]. Note that while Ca is defined as a function of the invading fluid, and is thus dependent upon whether the system is undergoing imbibition (brine is the invading phase) or drainage (CO_2 is the invading phase).

Previous work has shown that under certain conditions, the Ca of the imbibition process determines the trapped NW saturation of the post-imbibition, residual state [Chatzis and Morrow, 1984; Chatzis et al., 1988; Morrow et al., 1988]. When a relationship between imbibition Ca and residual NW saturation is apparent, it is described by a constant residual saturation value for low imbibition Ca values with a sharp decrease in residual saturation as Ca of the imbibition process increases above the threshold or “critical” capillary number [Cense and Berg, 2009; Morrow et al., 1988]; this is shown in Figure 4-1 (modified from Cense and Berg [2009]).

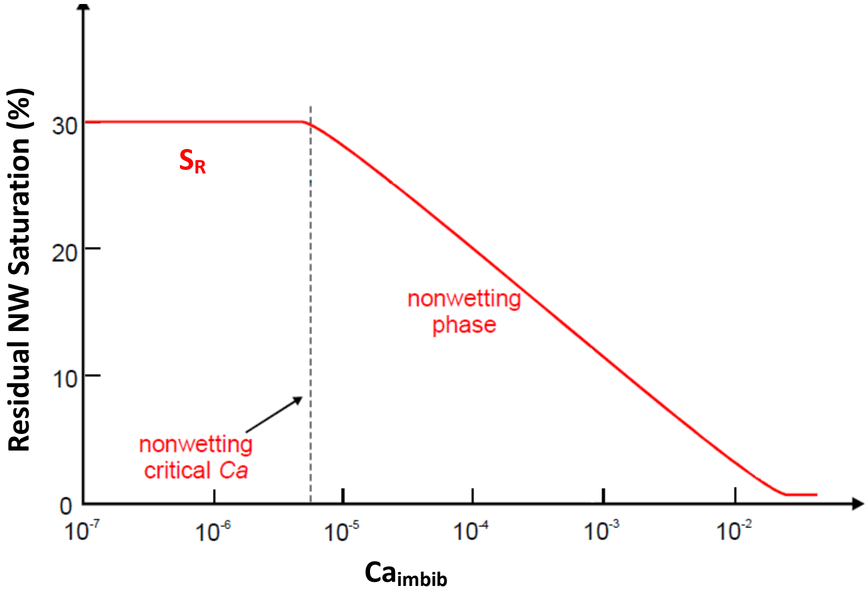

Figure 4-1. Capillary trapped residual nonwetting (NW) phase saturation (S_R) as a function of imbibition capillary number (Ca_{imbib}), modified from Cense and Berg (2009).

This relationship between Ca and NW saturation post-imbibition has been shown during NW desaturation experiments wherein the initial-state system (NW fluid is present in the medium) is water-flooded at increasing flow rates and the NW phase saturation in the core is measured as a function of Ca [Cense and Berg, 2009; Chatzis et al., 1988; Morrow et al., 1988; Suekane et al., 2010]; it is shown in sets of drainage-imbibition experiments conducted at different imbibition Ca [Chatzis et al., 1988; Herring et al., 2013] and has also been supported by modeling results [Hughes and Blunt, 2000; Nguyen et al., 2006]. Ca is not a complete descriptor of trapping in a porous medium, however, as the curves describing the dependence of residual saturation on Ca can shift due to changes in NW fluid properties [Ding and Kantzas, 2007] or medium properties [Nguyen et al., 2006]. Additionally, other experimental studies in different systems have found reduced or no dependence on Ca [Harper, *in prep*; Geistlinger, 2014; Mayer and Miller, 1993].

In a 3D system, the gravitational force is considered via the Bond number (Bo); which here is defined as:

$$Bo = \frac{\text{Gravity Force}}{\text{Capillary Force}} = \frac{\Delta\rho \cdot g \cdot d^2}{\sigma} \qquad \text{(eqn. 4.2)}$$

where $\Delta\rho$ is the density difference between the two fluids [kg/m^3], g is the acceleration of gravity [m/s^2], and d is the representative length scale [m]. Here, in order to emphasize that forces are examined from a pore-scale perspective, as well as for ease of comparison with other studies, d is defined as the median grain diameter (or equivalent grain diameter for a micromodel); this is in agreement with Mohammadian et al. [2014]. Note that while Ca is defined as a function of the invading fluid, and is thus dependent upon whether the system is undergoing imbibition or drainage, Bo is constant for a given fluid pair-porous medium system.

A combination of these two dimensionless numbers presents a description of the ratio of viscous to gravitational forces:

$$Ca \cdot Bo^{-1} = \frac{\text{Viscous Force}}{\text{Gravity Force}} = \frac{\mu_{\text{INV}} v_{\text{INV}}}{\Delta\rho \cdot g \cdot d^2} \qquad \text{(eqn. 4.3)}$$

Following Polak et al., [2011] we will use these dimensionless numbers to determine which forces are dominant during the imbibition process, on a pore-scale basis, in a 3D porous medium system; note that this analysis should be considered to be an “order of magnitude” approximation. Figure 4-2 shows the location of a number of existing 3D multiphase flow studies overlaid onto the pore scale force balance diagram. Note that medium topology and morphology (coordination number, pore-throat aspect ratio) and other media features (e.g. porosity, consolidated vs. unconsolidated, wettability) which may also be important to multiphase fluid flow are not well-represented by this model, nor is the defending fluid viscosity. As suggested by Polak et al. [2011], we suggest that the relative location of a system within the pore-scale force balance illustrates which force(s) has the greatest impact on flow processes. In their study, Polak and colleagues demonstrated the interplay of all three forces (capillary, viscous, and gravitational) resulting in a figure very similar to that shown in Figure 4-2; however, we have modified their original formulation via reformation of the representative length scale *d* in Bo in order to more easily accommodate comparison of a wider range of experimental studies and to emphasize that we examine these systems on a pore-scale basis.

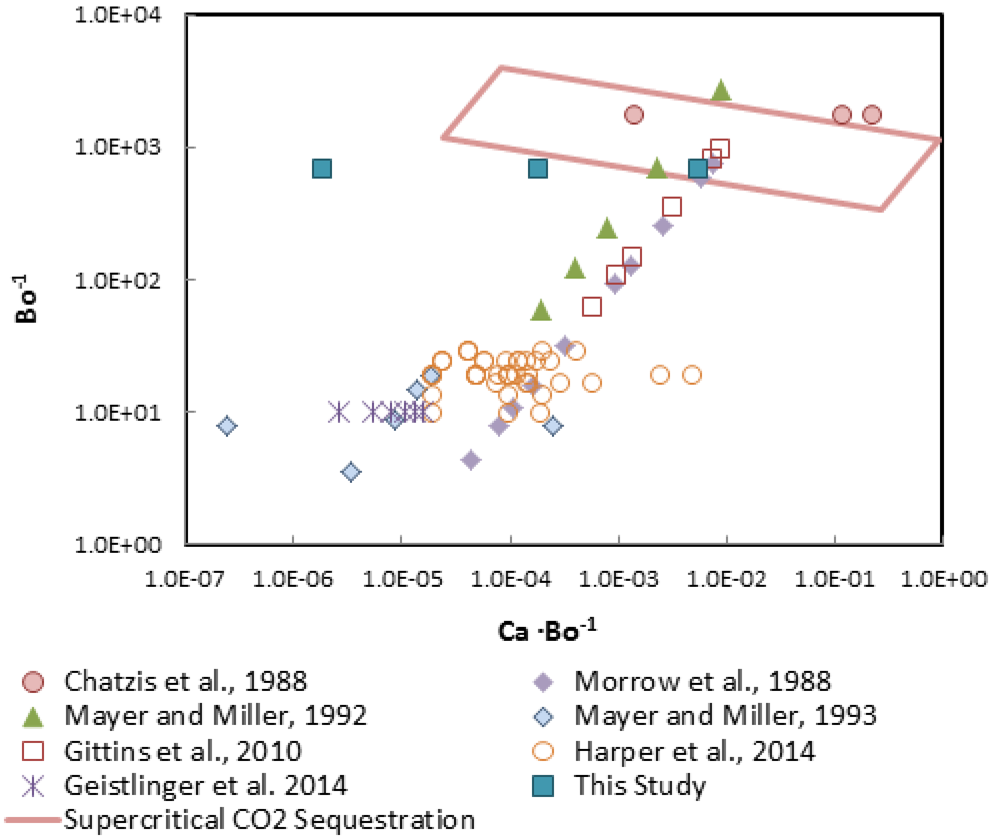

Figure 4-2. The locations of imbibition processes of previous works, the experiments of this study, and an approximate range for supercritical CO_2 sequestration (red rhomboid) within the pore scale force balance. Inverse Bond number (Bo^{-1}) describes the balance between capillary and gravitational forces, and the product of capillary number (Ca) and Bo^{-1} describes the balance between viscosity and gravitational forces.

The studies presented in Figure 4-2 lie within several general areas of force dominance. For studies with systems which lie in the upper right corner of the figure, both capillary and viscous forces are important; in this regime there is a transition between whether capillary and viscous forces dominate, and trends of residual saturation with Ca are evident; e.g. Chatzis et al. [1988] found that residual saturation and NW blob morphology after imbibition was a function of Ca. However, in this area of the figure, gravitational forces play a minor role, explaining the findings of Mayer and Miller [1992] and Gittins et al. [2010] which state that the bead/grain size (equivalent to d, a gravity force parameter) has no effect on the amount residual NW saturation. For experimental systems closer to the bottom left of the figure, gravity forces impact the experiments, e.g. the experiments of Morrow et al. [1988] range from the capillary-viscosity dominated regime to the gravity dominated regime, and the results of that study demonstrate a significant dependence on both Ca and Bo. Moving down Figure 4-2 (further away from the capillary dominated regime and into gravity dominated space), the experiments of Mayer and Miller [1993] showed that blob morphology exhibited a strong dependence on Bo, and only a very weak dependence on Ca. More recently, Harper et al. [*in prep*] found no correlation of residual NW saturation with Ca, but rather that Bo and defending phase viscosity were the most significant parameters. Similarly, Geistlinger et al. [2014] found no correlation of residual saturation with Ca, and rather that trapped NW phase is dependent on pore size distribution (again, a parameter with indicates gravity dependence).

This basic force dependence analysis explains the differences in findings of experimental studies with a large range of porous media, flow conditions, and fluid pairs; and resolves some of the seeming contradictions that have been observed by experimentalists. The location in the force dominance plot of the brine-air-Bentheimer sandstone experiments of this study are shown with the approximate location of supercritical CO_2 sequestration scenarios, given the range of supercritical CO_2 fluid properties attainable and assuming similar media to Bentheimer sandstone (Figure 4-2). In light of the above discussion, we expect capillary and viscous forces to dominate both the brine-air-Bentheimer ambient condition experimental system as well as a geologic supercritical CO_2 sequestration scenario.

4.3.2 Initial State Topology

Following Herring et al. [2013], we refer to a system uniformly saturated with W fluid to be in the original state; a post-drainage system (i.e. NW is introduced to the system) as being in the initial state; and a post-imbibition system as the residual state. The well-documented capillary pressure hysteresis present in multiphase systems (e.g. Morrow [1970]) dictates that the residual state (and thus, trapped NW saturation) is dependent on the initial state. The relationship between initial and residual NW saturation (S_I and S_R, respectively) in porous media has been investigated and described empirically by the so-called Land's model; it has been established that as initial NW saturation increases, residual NW saturation increases towards a plateau-like maximum [Al Mansoori et al., 2010; Land, 1968]. An alternate means to visualize this relationship is to examine the "trapping efficiency" (i.e. S_R/S_I) as a function of initial NW saturation: S_R/S_I is highest at relatively low S_I values, and decreases as S_I continues to increase [Akbarabadi and Piri, 2013]. While these empirical relationships are well characterized for a variety of porous media systems, the underlying physical mechanisms for this behavior remain relatively poorly understood. As originally suggested by Wardlaw and Yu [1988], and further examined by Herring et. al. [2013], we propose that the reason for the plateau in the Land's model description of trapping and the associated decrease in trapping efficiency at high S_I values is due to high connectivity of the NW phase at high NW saturation: as the NW fluid becomes highly interconnected via increasing numbers of pore throats, the pathways available for mobilization dramatically increase.

We have previously investigated this phenomenon by examining trapping efficiency as a function of initial NW phase topology, specifically, as quantified by the initial normalized NW Euler number ($\hat{\chi}$) [Herring et al., 2013]. Herein, we further develop and compare this approach to another quantitative descriptor of connectivity, the gamma function (Γ), which is a statistical percolation metric described by Renard and Allard [2013].

4.3.2.1 *Topological Invariants*

Topological invariants are properties of objects which are not changed by continuous deformations such as stretching, bending, and twisting; they are only changed when parts of an object are discontinuously deformed (i.e. "torn" or "glued together"). Topological invariants describe an object's connectivity; in comparison to an object's geometry, which describes its shape. The Euler number (χ) is a topological invariant defined as the alternating sum of the first three Betti numbers (β_0, β_1, β_2):

$$\chi = \beta_0 - \beta_1 + \beta_2 \qquad \text{(eqn. 4.4)}$$

where β_0 is the number of individual objects present, β_1 is the number of redundant loops or handles present (e.g. the handle on a coffee mug or the loop of a doughnut), and β_2 is the number of holes or hollows within the object(s) present. Applied to a fluid phase within a porous medium, β_0 can be thought of as the number of distinct, individual fluid clusters; β_1 is the number of redundant connections via pore throats within the clusters; and β_2 is the number of bubbles of a different fluid or solid particles suspended in the fluid. For this work, we investigate the topology of a less-dense NW fluid (air), which implies that β_2 will be zero (i.e. no “floating” water droplets or rock grains in the air phase). Thus $\beta_2=0$ for conversion between Euler number and Betti numbers; this is in agreement with analysis by Vogel [2002]. A topological description of the connectivity of a NW fluid phase in a porous medium is fairly intuitive; during a drainage process, for example, as fluid clusters coalesce and grow together, the number of individual NW objects (β_0) decreases; and as more and smaller pore throats are invaded, the number of redundant connections within the NW fluid clusters (β_1) increases. This leads to an overall decrease in Euler number; therefore, as Euler number becomes more and more negative, the NW phase fluid is becoming better connected. At some critical value of NW saturation, the NW phase will be connected across the domain; the transition from dominantly disconnected ($\chi>0$) to dominantly connected ($\chi<0$) is related to the percolation threshold for a given phase [Mecke and Wagner, 1991; H.J. Vogel, 2002] and the saturation at which the Euler number is exactly zero is an estimate of the saturation percolation threshold for NW phase flow.

The Euler number is an extensive property of a system in that the overall Euler number for a domain is the sum of the values of all subdomains within it. Therefore the Euler number depends on the scale over which they are averaged; the Betti numbers are also scale-dependent. Values of the Euler number or Betti numbers calculated on one section of an object are local (rather than global) values, and are therefore not representative of the total overall object, nor are they necessarily representative of other same-sized subsections of the object due to statistical variation or small-scale heterogeneities. However, appropriate normalization of the Euler or Betti values leads to a more representative metric. Herring et al. [2013] calculated Euler numbers for the entire pore space (i.e. Euler numbers for systems at 100% NW phase saturation), and normalized the Euler number for the system at a given saturation by the Euler number at 100% NW phase saturation:

$$\hat{\chi}_{NW} = \frac{\chi_{NW}}{\chi_{100\%NW}} \qquad \text{(eqn. 4.5)}$$

This normalization results in a connectivity metric with a maximum value (most connected) of 1.0, where negative values indicate disconnectedness. A representative elementary volume (REV) analysis (Appendix, Section 4.10.3) demonstrates that $\hat{\chi}_{NW}$ can be used as a representative measure of NW phase connectivity for a given sample. However, values of $\hat{\chi}_{NW}$

are highly dependent on the value of $\chi_{100\%NW}$, so accurate measurement of this parameter is essential.

4.3.2.2 Statistical Percolation Metrics

The term "percolation" refers to the transition from individual, disconnected clusters to one large cluster which spans the length of the porous domain; e.g. once a single NW phase pathway is established all the way through a porous medium, the NW fluid can be said to percolate through the media. The gamma function (Γ) is a probability-based percolation metric described by Renard and Allard [2013] and is defined here as a function of permeable phase saturation, p. In the context of NW phase fluid transport, we define the permeable phase p to be NW fluid. Thus, Γ(NW) is the ratio of pairs of individual NW voxels that are connected to all the possible pairs of NW voxels and can be computed directly from the cluster size distribution:

$$\Gamma(\mathrm{NW}) = \frac{1}{n_{NW}^2} \sum_{i=1}^{N(X_{NW})} n_i^2 \qquad \text{(eqn. 4.6)}$$

where n_{NW} is the total number of NW phase voxels in the set X_{NW}, N(X_{NW}) is the number of distinct clusters in the set X_{NW}, and n_i is the number of NW voxels in cluster i.

As Γ(NW) approaches 1.0, the fraction of the fluid that lies in a single cluster increases. In contrast to the local Euler values described above, this metric is global: by necessity, it must be computed over the entire domain of the system, and therefore describes the entire system. By value of being a probability metric, Γ(NW) can be assumed to be representative of a given sample without further manipulation or normalization (again assuming a representative elementary volume has been achieved, see Section 4.10.3 for REV analysis of Γ(NW)). Also note that the definition of Γ inherently weights clusters by their size, unlike the Euler number; with the result that Γ(NW) is much less susceptible to noise which would manifest as falsely labeled NW voxels.

4.4 Materials and Methods

The complete experimental set-up and process is similar to that of Herring et al. [2013] and only deviations from the previous study and the general process will be described here. Experiments were conducted with two 6.2 mm diameter Bentheimer sandstone cores of lengths of approximately 21 mm. Air was the NW fluid, and the W fluid was brine made of degassed millipore DI water doped with potassium iodide (KI), one part KI to six parts water by weight. The core was first vacuum-saturated with brine, and an x-ray tomographic scan was taken to characterize the original NW phase saturation (S_O) inside the core. Then brine was drained from the core to a predetermined initial NW phase saturation (S_I) value at a flow rate of 0.2 ml/hr, using a Harvard PHD2000 syringe pump (Harvard Apparatus, Holliston MA, United States), and another tomographic scan was collected. Finally, brine was imbibed into the core at one of three different flow rates (0.018 ml/hr, 1.8 ml/hr, or 54 ml/hr) and a scan was acquired of the residual NW phase saturation (S_R). For three experiments, the core was dried under vacuum resulting in relatively high NW saturation (e.g. 94%-100% NW saturation), and the imbibition process was performed on the dry core. A pressure transducer (Validyne Engineering, Northridge CA, United States) with a range of 14.0 kPa was connected in parallel with the brine flow line to measure capillary pressure response.

Tomographic imaging was performed at the bending magnet beam-line at sector 13 (GSECARS) at the Advanced Photon Source at Argonne National Laboratory; specifications for the beamline have previously been reported [Rivers et al., 1999; Wildenschild et al., 2005; Wildenschild et al., 2002]. Scans were performed at a monochromatic energy level of 33.269 keV, just above the K-shell photoelectric absorption edge of iodine (33.169 keV), resulting in x-ray attenuation by the KI-doped brine and thus allowing for separation of the wetting and non-wetting fluids in the reconstructed images. Images were captured at 720 angles, with a voxel resolution of 5.8 µm. After reconstruction, a cylindrical subsection of diameter 975 voxels and height 600 voxels (approximately 90 mm^3) was chosen which excludes the walls from the volumes (Figure 4-3a). This data size is larger than the determined REV for connectivity measures of 600 x 600 x 600 voxels, which is equivalent to a physical volume of 40 mm^3 (Appendix A). A median filter was applied to smooth the images and reduce random noise (Figure 4-3b), and a histogram of the grayscale values present in each volume was calculated. The histogram minimum separating those grayscale values representing air and those representing sandstone grains or brine were determined for each volume (Figure 4-3d), and the threshold value was set equivalent to this minimum value resulting in the final binarized data volume (Figure 4-3c). Finally, a size exclusion filter was applied which removed air-labeled clusters less than 125 voxels; this volume corresponds to a spherical pore of radius 18 μm which is smaller than the minimum pore size distribution of Bentheimer as measured by Maloney et al.[1990]. This process results in a binary image with only NW phase labeled. Avizo Fire TM was then used to quantify cluster volumes, cluster numbers, and Euler numbers.

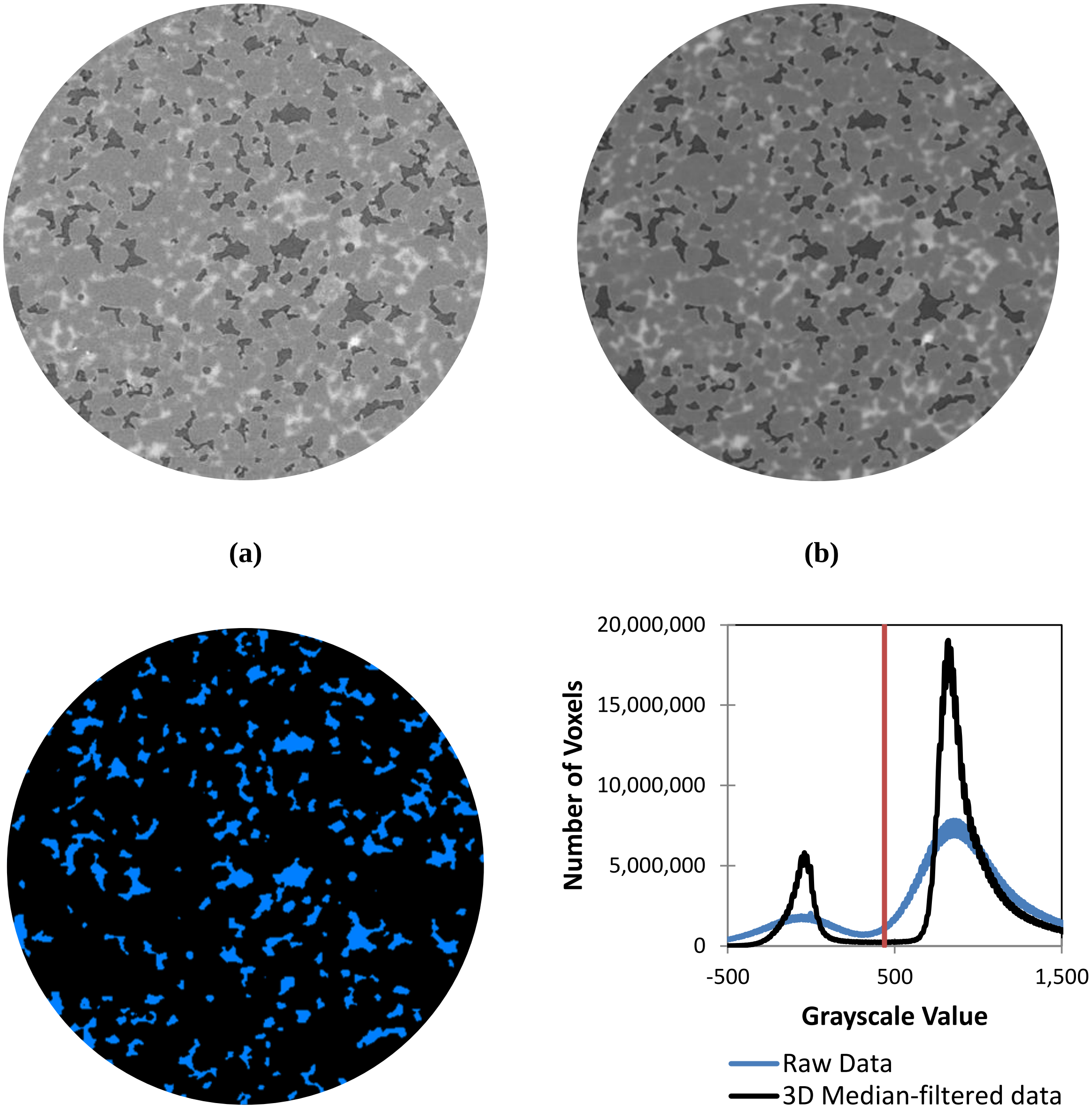

(a) **(b)**

(c) **(d)**

Figure 4-3. A cross-sectional slice of (a) raw data, (b) data after application of a three-dimensional (3D) median filter, and (c) binary data with the nonwetting (NW) phase identified. The grayscale histogram of the data volume for both raw and 3D median-filtered data is shown in (d) with the grayscale threshold value indicated by the red line.

4.5 Sensitivity of Connectivity Metrics to Image Quality

Given the dependence of connectivity metric calculations on very small features, image-derived connectivity metrics must be calculated on an REV and may be sensitive to various image quality parameters, for example: noise levels, data resolution, the type of filters applied to the data, segmentation method, and segmentation threshold values. An investigation into the sensitivity to these factors of both the normalized Euler value ($\hat{\chi}_{NW}$) and the gamma function (Γ(NW)) was conducted and is presented in Section 4.10; for brevity, only the results are highlighted here. In order to examine the sensitivity of these parameters on a wider range of image-based data, the relatively high quality data (with respect to phase contrast, noise, and voxel resolution) presented in this study which was collected at the Advanced Photon Source at Argonne National Lab at a resolution of 5.8 μm (denoted "APS" data) was compared to data presented in Herring et.al. [2013] which was collected via a polychromatic bench-top x-ray CMT system at Oregon State University at a resolution of approximately 10 μm (denoted "OSU" data). Image parameters for both data sets are shown in Table 4-1 in the appendix (Section 4.10). Based on the analysis of the two data sets, we established the following conclusions regarding the significance of these image quality parameters on the calculation of $\hat{\chi}_{NW}$ or Γ(NW):

- Noise which manifests as small, isolated, falsely labeled NW voxels has no significant impact on either Γ(NW) or $\hat{\chi}_{NW}$, as long as a minimum level of noise removal is applied. In the case of the high resolution APS data, noise reduction was achieved using a median filter on the grayscale image and by processing the segmented (binary) data to remove isolated NW clusters smaller than 52 voxels (equivalent to a sphere with a radius of 18 μm) was sufficient to provide consistent $\hat{\chi}_{NW}$ calculations.

- A representative elementary volume (REV) for the APS data is achieved at approximately 600 × 600 × 600 voxels (equivalent to a cube of 42.14 mm^3, or 3.48 mm per side) for both $\hat{\chi}_{NW}$ and Γ(NW) in Bentheimer sandstone. Use of an analytical volume smaller than the REV has a relatively small effect on the calculation of $\hat{\chi}_{NW}$, and a dramatic effect on the calculation of Γ(NW).

- Image resolution has minimal impact on calculation of both $\hat{\chi}_{NW}$ and Γ(NW) for the range of resolution investigated (5.8 µm and 10 µm).
- Data processing schemes (i.e. filters and threshold detection method applied) have a significant effect on both $\hat{\chi}_{NW}$ and Γ(NW). The OSU data presented in Herring et al. [2013] was originally processed using ROCK3DMA, an Indicator Kriging segmentation algorithm [Oh and Lindquist, 1999]. Comparison of the original OSU Indicator Kriging results with the APS data (which was smoothed using a median filter, denoised, and segmented via simple grayscale histogram thresholding as described in Section 4.4) demonstrates disagreement in the $\hat{\chi}_{NW}$-saturation and Γ(NW)-saturation relationships and in absolute $\hat{\chi}_{NW}$ and Γ(NW) values. Reprocessing the grayscale OSU data by the same process as the APS data resolves this disagreement in the calculation of $\hat{\chi}_{NW}$, but Γ(NW) remains inconsistent between the data sets. This highlights that different data sets must processed and evaluated carefully to ensure accurate comparison.
- For data with unfavorable grayscale histograms due to the lack of distinctive peaks or poorly defined minima between the NW and solid/W phases, the choice of grayscale segmentation threshold has a minor effect on the calculation of Γ(NW), but a significant effect on the calculation of $\hat{\chi}_{NW}$. For these grayscale images (16 bit precision), changing the threshold by ±100 grayscale values results in approximately a ±20% shift in $\hat{\chi}_{NW}$ (Table 4.2). For images with poorly defined histogram peaks, a consistent and objective threshold detection system is therefore necessary.

It is important to note that for the image quality parameters which are highly important to connectivity metric calculations (i.e. data processing procedure and threshold determination) the most significant impacts are imparted on the images with the most NW fluid present: the dry, 100% NW fluid filled scan of the porous medium. As indicated by Equation 3.6 and noted above, the determination of $\chi_{100\%NW}$has a large impact on the analysis of the entire data set. Accurate acquisition, processing, and analysis of the dry scan of the medium is of great importance in ensuring the relevance and applicability of the overall data analysis.

4.6 Results

4.6.1 Force Balance Analysis and Traditional Empirical Relationships

Traditionally, capillary trapping has been investigated by examining the various relationships between initial NW saturation (S_I), residual NW saturation (S_R), and imbibition capillary number (Ca); for example see Chatzis and Morrow [1984], Chatzis et al. [1988], Al Mansoori et al. [2010], and Land [1968]. Both capillary trapping efficiency (S_R/S_I) and total capillary trapping (S_R) are important parameters to CO_2 sequestration operations, and can be investigated as a function of S_I and imbibition Ca (Figure 4-4).

From the force balance analysis presented in Section 4.3.1, the Bentheimer-brine-air system is expected to be dominated by capillary and viscous forces, as is the sandstone- CO_2-brine system; thus, the residual state of both systems should depend on imbibition Ca. Bond number (Bo) values for the CO_2-brine-sandstone system are approximately an order of magnitude smaller than those for the Bentheimer-brine-air system (i.e. the CO_2-brine-sandstone system has less gravity force influence than the ambient condition experimental system); however, neither system exists in a gravity dominated regime, so we expect that the ambient Bentheimer-brine-air system will produce results that are similar to a geologic CO_2 sequestration operation.

As shown, the expected trends of decreased total NW capillary trapping (S_R) and decreased trapping efficiency (S_R/S_I) with increasing imbibition Ca are present (Figure 4-4a and 4-4b), as is the traditional Land’s model description of increasing residual NW saturation with increasing initial NW saturation (Figure 4-4c). However, there is a large amount of scatter in the data which is not resolved by normalizing the residual saturation by the initial saturation, or by grouping the data by the imbibition Ca value; this discrepancy is investigated in the next section.

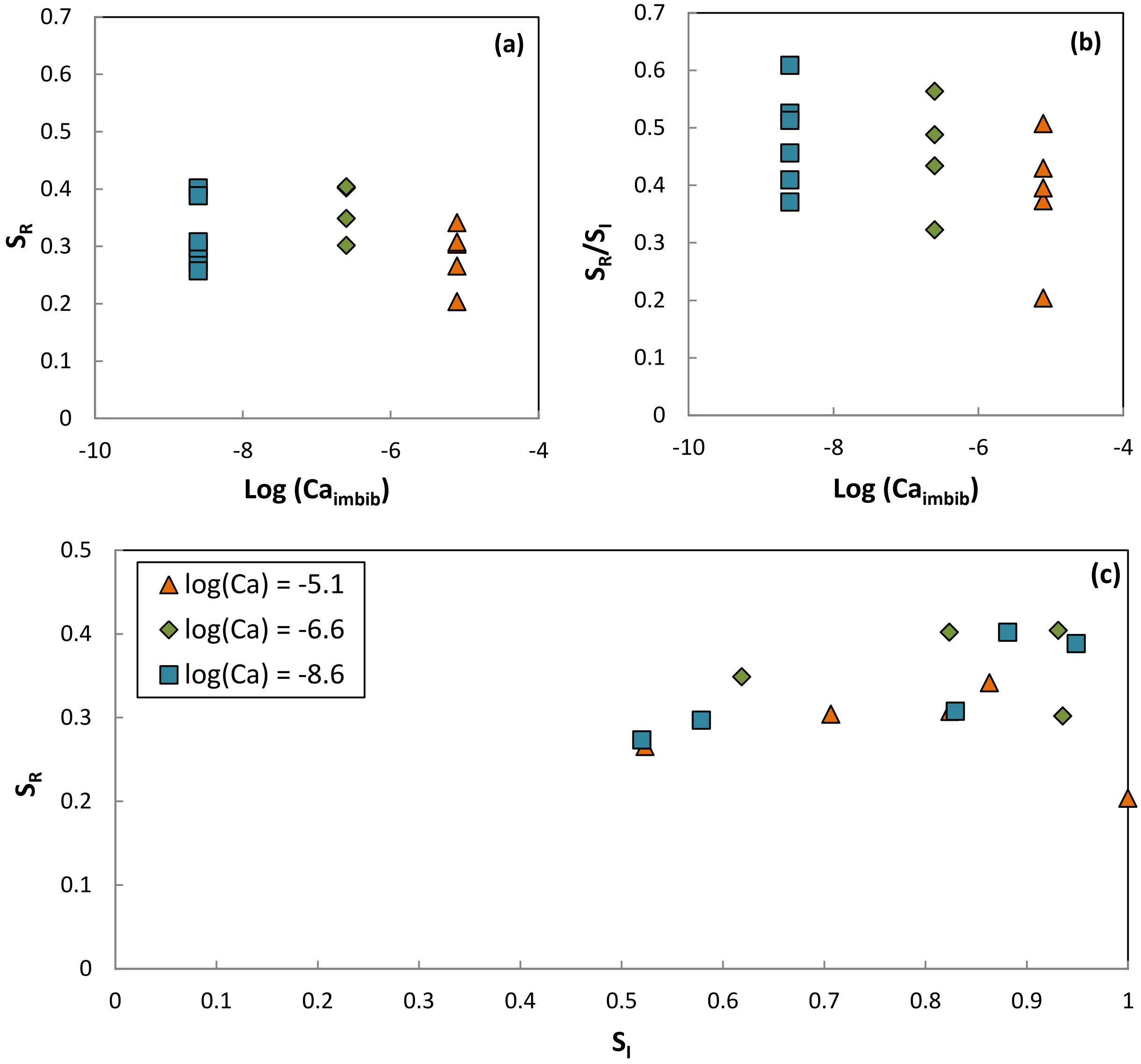

Figure 4-4. Results of drainage-imbibition experiments presented as (a) residual saturation (S_R) as a function of imbibition capillary number (Ca_{imbib}); (b) trapping efficiency, calculated as residual saturation normalized by initial saturation (S_I), as a function of imbibition Ca; and (c) residual saturation as a function of initial saturation (i.e. the traditional Land's model formulation [Al Mansoori et al., 2010; Land, 1968]) where experiments are classified by the imbibition Ca class as noted in the legend.

4.6.2 Inclusion of Connectivity

In order to understand the variability inherent in these results as described by the empirical models above, we consider how the connectivity of the nonwetting phase impacts trapping results. First, though, we investigate how the connectivity characteristics of the normalized Euler characteristic ($\hat{\chi}_{NW}$) and gamma function (Γ(NW)) manifest for NW fluid within porous media during the drainage process via the relationship between each connectivity metric and initial NW saturation (Figure 4-5).

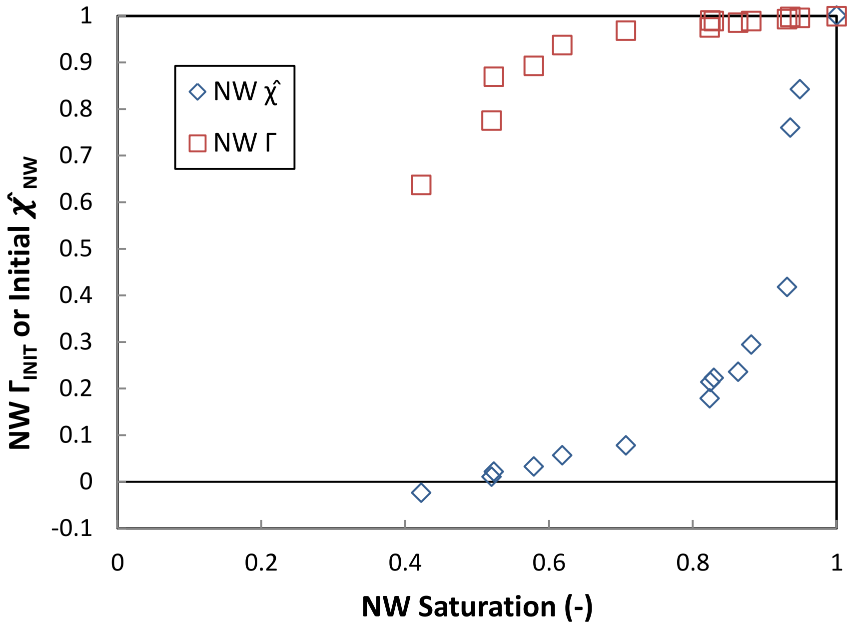

Figure 4-5. Initial nonwetting (NW) gamma function (Γ_{INIT}) and initial NW normalized Euler value ($\hat{\chi}_{NW}$) as a function of NW saturation within Bentheimer sandstone.

Here the differences in these connectivity metrics are dramatically apparent. Γ(NW) approaches a value of unity at relatively low saturation, implying that the majority of the nonwetting phase present is connected to the main cluster by at least one pore throat throughout the drainage process, with increasing probability that any isolated NW cluster will become connected to the main cluster as initial NW saturation increases. Above an initial NW saturation of approximately 80%, the variation in Γ(NW) is negligible; implying that at NW saturation at or above 80%, all NW phase is connected via at least one pore throat within the medium.

The $\hat{\chi}_{NW}$ value provides a fundamentally different quantitative description of the NW fluid connectivity. At initial NW saturation greater than 50%, the number of NW clusters (β_0) roughly matches the number of connections within individual clusters (β_1), as indicated by $\hat{\chi}_{NW} \approx 0$. In direct comparison to Γ(NW), $\hat{\chi}_{NW}$ shows the most dramatic growth at values greater than 80% NW saturation, i.e. long after the largest cluster has already formed as evaluated by Γ(NW).

Γ(NW) values show that above 80%, almost all NW fluid is already connected and distinct individual fluid clusters are minimized, thus, the increase in $\hat{\chi}_{NW}$ is due to the increase in redundant connections, β_1. Consideration of Γ(NW) and $\hat{\chi}_{NW}$ together demonstrates both the degree and manner of NW phase connectivity within the porous medium: for the post-drainage Bentheimer-air-brine system, the NW phase is largely connected via one large cluster; and as NW saturation increases, the NW phase invades additional pore throats within this single cluster. This interpretation is further demonstrated by the approximately linear relationship between $\hat{\chi}_{NW}$ and the equilibration capillary pressure (the difference in pressure between the NW phase and the W phase) at the end of the drainage process (Figure 4-6). As capillary pressure increases, more (and smaller) pore throats are invaded, and $\hat{\chi}_{NW}$ increases.

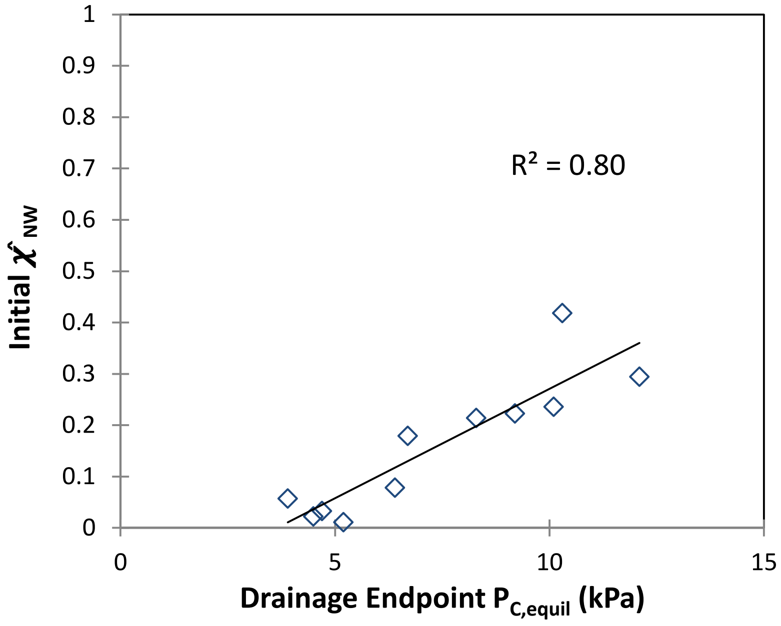

Figure 4-6. Initial nonwetting (NW) normalized Euler value ($\hat{\chi}_{NW}$) versus capillary pressure (P_C) after an equilibration period at the end of the drainage process within Bentheimer sandstone.

A $\hat{\chi}_{NW}$ value of zero provides an estimate of the percolation threshold; i.e. the NW saturation value at which NW phase fluid is connected throughout the porous medium, spanning the entirety of the domain [Mecke and Wagner, 1991; Vogel, 2002]. The relationship between initial $\hat{\chi}_{NW}$ and NW saturation demonstrated by the experimental data (Figure 4-5) shows that $\hat{\chi}_{NW}$=0 at NW saturation of approximately 50% within Bentheimer sandstone. A computational approach for predicting pressure-saturation curves in media was described by Hazlet [1995] and further by Hilpert and Miller [2001] wherein morphological opening with a sphere of incrementally increasing radius is performed on a binary representation of a porous medium (i.e. the dry image of the medium), and saturation and pressure values are calculated by simulation at each opening step. A similar process was applied here, wherein the opening procedure was performed on binary volumes of dry Bentheimer sandstone using Avizo Fire^{TM}. After each opening step, isolated NW fluid clusters (<10,000 voxels or a sphere of radius 77.5 µm) resulting from the opening process which were not connected to the main fluid clusters were removed. $\hat{\chi}_{NW}$ and saturation values were calculated for each successive opening; the results of this analysis are compared with the experimental data (Figure 4-7). The morphological opening procedure conducted on the dry images resembles the $\hat{\chi}_{NW}$ values at initial saturation to within a reasonable approximation, demonstrates that $\hat{\chi}_{NW}$=0 at NW phase saturation of 50% (providing additional evidence that the NW phase percolation threshold for Bentheimer sandstone is at a NW saturation of approximately 50%), and suggests that the $\hat{\chi}_{NW}$-saturation relationship for a given medium might be approximated from one high-quality (i.e. adequate resolution and low noise level) scan of a dry porous media rather than from multiple time-consuming experimental drainage observations.

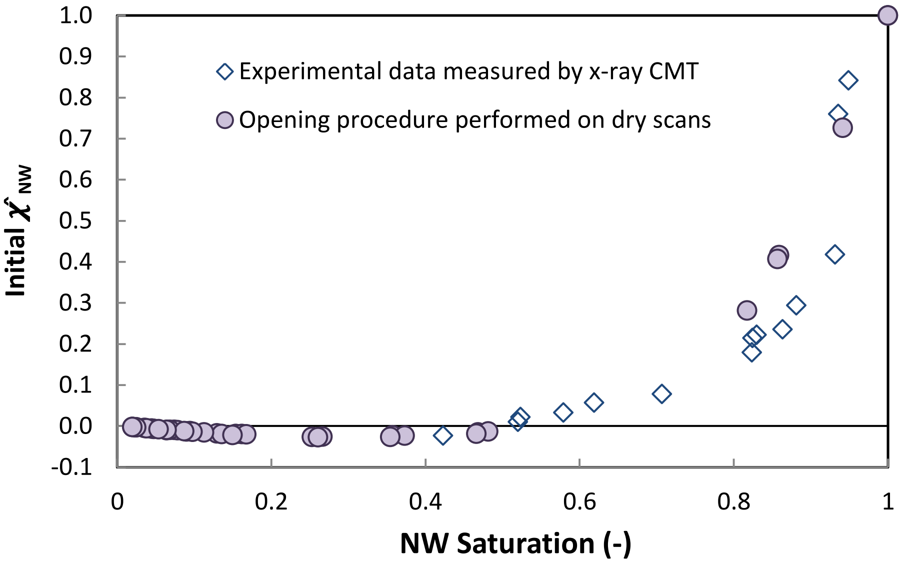

Figure 4-7. Initial nonwetting (NW) normalized Euler value ($\hat{\chi}_{NW}$) as a function of NW saturation within Bentheimer sandstone for experimental x-ray microtomography (x-ray CMT) data and for a computational morphological opening process performed on binary data of the dry sandstone.

Following Herring et al. [2013], we investigate the impact of connectivity on capillary trapping efficiency (Figure 4-8); these data are classified by the imbibition process Ca as in Figure 4-4c. While both Γ(NW) and $\hat{\chi}_{NW}$ plots show a relationship between capillary trapping efficiency and connectivity, the relationship between normalized initial $\hat{\chi}_{NW}$ and trapping efficiency shows a strong linear correlation (Figure 4-8a), compared to Γ(NW) (Figure 4-8b) where the trend is non-linear due to insensitivity of Γ(NW) in the high NW saturation range. This suggests that while NW trapping is certainly related to the general connectivity of the NW phase, the capillary trapping/mobilization process is directly related to the NW topology as described by the Euler characteristic. An increase in the number of redundant pore throats (β_1) which connect NW fluid within the fluid clusters, that is, a higher initial $\hat{\chi}_{NW}$ value, is equivalent to a higher number of potential pathways through which NW fluid can be mobilized, and results in decreased trapping efficiency. Note also that the high and intermediate imbibition Ca data show a relatively strong dependence on initial $\hat{\chi}_{NW}$ (slope of approximately -0.3 for both, R^2= 0.92 and 0.98 respectively) whereas low imbibition Ca experimental data exhibits much lower dependence (slope of -0.1, R^2=0.37). This suggests that fluid topology as described by $\hat{\chi}_{NW}$ plays a strong role in fluid mobilization during flow dominated by viscous forces, but has reduced impact during capillary dominated flow. This is consistent with standard understanding of displacement mechanisms. At sufficiently low flow rates the small pore throats that provide improved NW connectivity become water-filled by the process of “snap-off” early in the imbibition process. At higher flow rates snap-off is suppressed (e.g. Hughes and Blunt [2000]), so the connections through small pore throats remain open for longer and therefore have a bigger effect on the residual saturation.

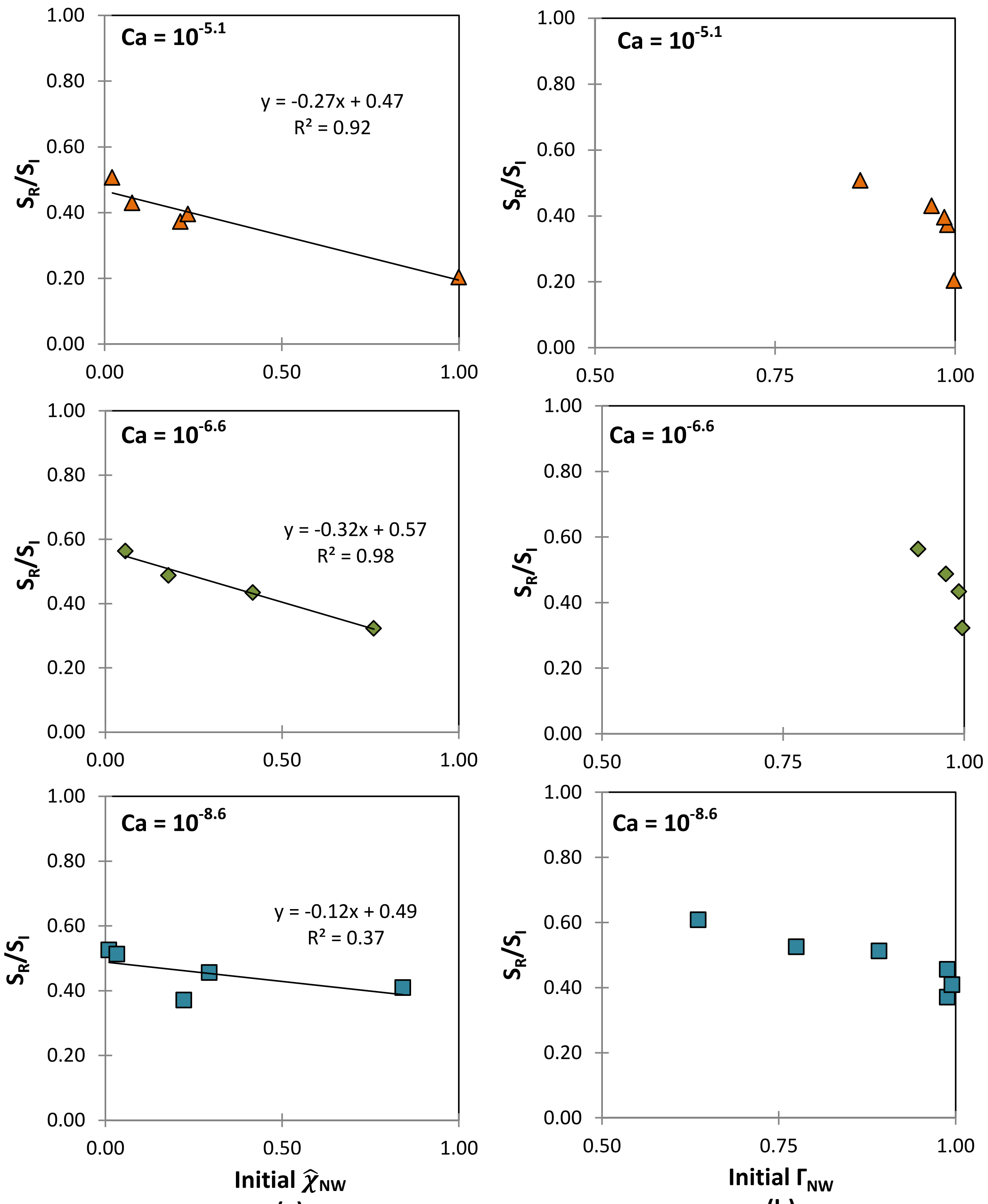

(a) (b)

Figure 4-8. Capillary trapping efficiency of nonwetting (NW) phase, as described by residual NW saturation (S_R) normalized by initial NW saturation (S_I), as a function of (a) normalized initial NW Euler value ($\widehat{\chi}_{NW}$) and (b) initial gamma value (Γ_{NW}). Data are classified by the experimental imbibition capillary number (Ca).

The relationship between residual trapping (S_R) and initial $\hat{\chi}_{NW}$ illustrates these results from a slightly different perspective (Figure 4-9); here a parabolic trend is evident for each imbibition Ca category. Maximum residual NW saturation, i.e. the maximum trapping capacity of the medium, is reached at a moderate initial $\hat{\chi}_{NW}$ value ($\hat{\chi}_{NW} \approx 0.4$) for both high ($10^{-5.1}$) and intermediate ($10^{-6.6}$) Ca imbibition values, and trapping capacity is unaffected by the initial $\hat{\chi}_{NW}$ for low ($10^{-8.6}$) Ca imbibition.

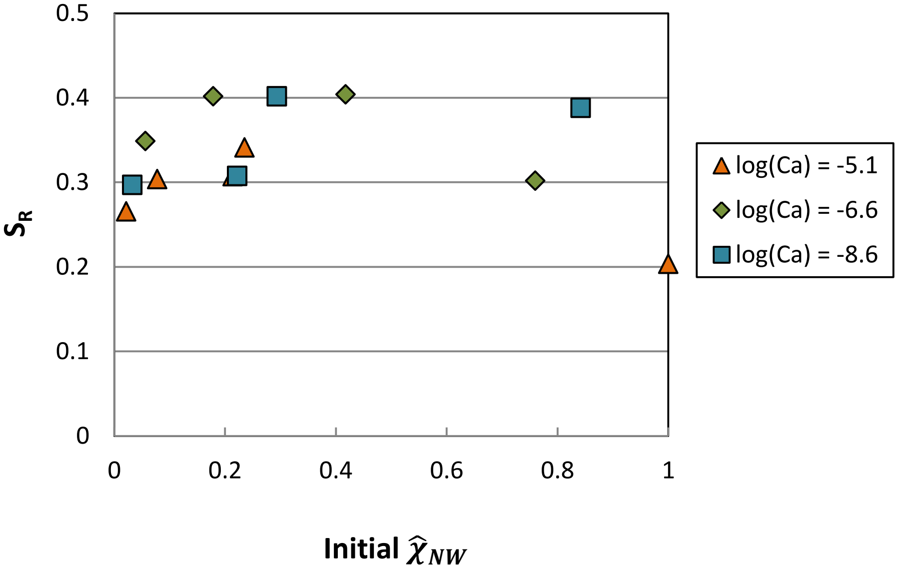

Figure 4-9. Residual capillary trapped nonwetting (NW) phase (S_R) as a function of normalized initial NW Euler value ($\hat{\chi}_{NW}$). Data are classified by the experimental imbibition capillary number (Ca).

4.7 Conclusion and Application to CO_2 sequestration

This work has presented the results of x-ray CMT quantified experiments of drainage and imbibition with a wetting (W) phase of 1:6 by weight KI brine and nonwetting (NW) phase of air within Bentheimer sandstone. We have determined, based on a pore-scale force analysis, that capillary and viscous forces will dominate the system rather than gravity forces. We have shown experimentally that the residual state of the system is indeed sensitive to changes in capillary number (Ca), which describes the relative importance of capillary and viscous forces in a multiphase system. We have also investigated two different quantitative connectivity metrics and shown that nonwetting phase trapping and mobilization is well described by the normalized

Euler number ($\hat{\chi}$) of the NW phase after drainage: a more highly connected NW phase is connected by a high number of redundant pore throats, which allows for more NW phase to be mobilized, thus resulting in reduced NW phase capillary trapping efficiency. The dependence of capillary trapping on NW phase $\hat{\chi}$ is more pronounced for systems in a viscosity dominated regime; for capillary-dominated systems (low Ca), the NW phase connectivity has less impact on the final NW trapping.

Sedimentary reservoirs are proposed to be optimal storage sites for CO_2 sequestration due to the stratigraphy of porous, permeable sandstone and carbonate layers (which act as storage layers) and relatively impermeable silt and shale stone layers (which act as caprocks) [Bachu, 2003; Gunter et al., 2004]. Given the range of supercritical CO_2 fluid properties attainable in a sequestration operation, and in similar media to Bentheimer sandstone, the supercritical CO_2-brine-sandstone system will be dominated by capillary and viscous forces at the pore scale (Figure 4-2), and fall in the same general area of the force balance plot as the air-brine-Bentheimer experiments presented here. Thus, we expect that pore scale capillary trapping and mobilization of supercritical CO_2 during sequestration to behave similarly to the air-brine-Bentheimer system examined here. Indeed, Herring, et al. [2014] found that micromodel studies of ambient-state NW phase invasion were able to accurately predict the flow pattern of supercritical CO_2 during drainage in Bentheimer sandstone by consideration and proper dimensional analysis of fluid properties.

Comparison of Figure 4-4c with a typical Land's model curve (e.g. Al Mansoori et al. [2010]) demonstrates that the plateau in NW S_R values that is apparent above approximately 50% initial NW saturation is due to the percolation threshold being exceeded during the drainage process. Further, the data presented here shows that for a system at an initial NW saturation approaching 100% (and thus, maximum NW connectivity, $\hat{\chi}_{nw}$=1.0), capillary trapping is further suppressed and NW S_R actually decreases. This has important implications for CO_2 sequestration operations, where high CO_2 saturations may exist near the injection site, and where dry-out conditions may occur [Pruess and Müller, 2009]. Dry-out occurs when CO_2 which is in chemical non-equilibrium with brine is injected into the subsurface, causing the resident brine to dissolve into the CO_2 phase and creating subsurface areas where NW phase saturation approaches 100%; if brine salinity is sufficiently high, dry-out may cause salt precipitation leading to reduced permeability [Pruess and Müller, 2009].

In the example of a geologic CO_2 sequestration operation, Figures 4-8a and 4-9 imply that two distinct methodologies could be used to maximize capillary trapping, depending on the desired result. To maximize capillary trapping efficiency (S_R/S_I), and ensure that the largest fraction of injected CO_2 is immobilized in the pore space of the reservoir, the CO_2 injection should be engineered to result in low initial $\hat{\chi}_{nw}$ (e.g. $\hat{\chi}_{nw} \leq 0.1$, or $S_I \leq 0.75$). This would provide for additional storage security beyond relying on a structural/stratigraphic trapping layer. In contrast, in order to utilize the maximum trapping capacity of the pore space, CO_2 injection should be engineered to result in moderate initial $\hat{\chi}_{nw}$ (e.g. $\hat{\chi}_{nw}$=0.4, or $S_I \approx 0.85$). For either goal, dry-out conditions should be avoided. Manipulation of initial $\hat{\chi}_{nw}$ could potentially be accomplished via use of a water-alternating-gas scheme (as proposed by Spiteri et al. [2005]), which may have significant water use impacts; or via manipulation of injection patterns to inject to intermediate saturations. For example, one suggestion would be to have a shorter vertical injection interval in the injection well: injection only into the lower portions of the aquifer would allow for vertical migration and might prevent the CO_2 plume from approaching high saturation levels at the injection point. Alternatively, the subsequent imbibition process should be carried out at very low Ca regime, where NW topology does not impact residual saturation or capillary trapping efficiency. Manipulation of far-from-wellbore saturation can be achieved for well-characterized aquifers by designing the injection program in conjunction with large-scale simulation.

4.8 Acknowledgements

This material is based upon work supported by the U.S. Department of Energy, Basic Energy Sciences, Geosciences Program under award number DE-FG02-11ER16277, and also through the LANL/LDRD Program (#20100025DR). This research used resources of the Advanced Photon Source which is a DOE Office of Science User Facility. We acknowledge the support of GeoSoilEnviroCARS (Sector 13), which is supported by the National Science Foundation - Earth Sciences (EAR-1128799), and the Department of Energy, Geosciences (DE-FG02-94ER14466). We are grateful to the GSECARS staff for technical support during beam-time, in particular Dr. Mark Rivers. L. Andersson wishes to acknowledge funding from the Swedish Science Council.

The research of Adrian Sheppard is supported by an Australian Research Council Future Fellowship (FT100100470).

4.9 References

Akbarabadi, M., and M. Piri (2013), Relative permeability hysteresis and capillary trapping characteristics of supercritical CO_2/brine systems: An experimental study at reservoir conditions, Advances in Water Resources, 52, 190-206.

Al Mansoori, S. K., E. Itsekiri, S. Iglauer, C. H. Pentland, B. Bijeljic, and M. J. Blunt (2010), Measurements of non-wetting phase trapping applied to carbon dioxide storage, International Journal of Greenhouse Gas Control, 4(2), 283-288.

Andrew, M., B. Bijeljic, and M. J. Blunt (2013), Pore-scale imaging of geological carbon dioxide storage under in situ conditions, Geophysical Research Letters, 40(15), 3915-3918.

Bachu, S. (2003), Screening and ranking of sedimentary basins for sequestration of CO_2 in geological media in response to climate change, Environmental Geology, 44(3), 277-289.

Bachu, S., and D. B. Bennion (2008), Interfacial Tension between CO_2, Freshwater, and Brine in the Range of Pressure from (2 to 27) MPa, Temperature from (20 to 125) °C, and Water Salinity from (0 to 334 000) mg•L−1, Journal of Chemical & Engineering Data, 54(3), 765-775.

Bachu, S., and B. Bennion (2008), Effects of in-situ conditions on relative permeability characteristics of CO_2-brine systems, Environmental Geology, 54(8), 1707-1722.

Bachu, S., and D. Brant Bennion (2009), Dependence of CO_2 -brine interfacial tension on aquifer pressure, temperature and water salinity, Energy Procedia, 1(1), 3157-3164.

Cense, A. W., and S. Berg (2009), The Viscous-Capillary Paradox in 2-Phase Flow in Porous Media, paper presented at International Symposium of the Society of Core Analysts, Shell International Exploration & Production, Noordwijk, The Netherlands, 27-30 September, 2009.

Chatzis, I., and N. R. Morrow (1984), Correlation of capillary number relationships for sandstone, Journal Name: SPEJ, Soc. Pet. Eng. J.; (United States); Journal Volume: 24:5, Medium: X; Size: Pages: 555-562.

Chatzis, I., M. S. Kuntamukkula, and N. R. Morrow (1988), Effect of capillary number on the microstructure of residual oil in strongly water-wet sandstones, Journal Name: SPE (Society of Petroleum Engineers) Reserv. Eng.; (United States); Journal Volume: 3:3, Medium: X; Size: Pages: 902-912.

Ding, M., and A. Kantzas (2007), Capillary number correlations for gas-liquid systems, 6 pp., Society of Petroleum Engineers, Calgary, CANADA.

Gittins, P., S. Iglauer, C. H. Pentland, S. Al-Mansoori, S. Al-Sayari, B. Bijeljic, and M. J. Blunt (2010), Nonwetting phase residual saturation in sand packs, Journal of Porous Media, 13(7), 591-599.

Geistlinger, H., Mohammadian, S., Schlueter, S., & Vogel, H.-J. (2014). Quantification of capillary trapping of gas clusters using X-ray microtomography. *Water Resources Research*, *50*(5), 4514–4529. doi:10.1002/2013WR014657

Gunter, W. D., S. Bachu, and S. Benson (2004), The role of hydrogeological and geochemical trapping in sedimentary basins for secure geological storage of carbon dioxide, Geological Society, London, Special Publications, 233(1), 129-145.

Harper, E. J. Herring, A.L.; Armstrong, R.T.; Lunati, I.; Bay, B.K.; Wildenschild, D. On the Optimization of Capillary Trapping during Geologic CO_2 Sequestration, *In prep*.

Hazlett, R. (1995), Simulation of capillary-dominated displacements in microtomographic images of reservoir rocks, Transp Porous Med, 20(1-2), 21-35.

Helmut Geistlinger, S. M., Steffen Schlüter, Hans-Jörg Vogel (accepted), Quantification of Gas Phase Trapping within the Capillary Fringe Using Micro-CT, Water Resources Research.

Herring, A. L., E. J. Harper, L. Andersson, A. Sheppard, B. K. Bay, and D. Wildenschild (2013), Effect of fluid topology on residual nonwetting phase trapping: Implications for geologic CO_2 sequestration, Advances in Water Resources, 62, 47-58.

Herring, A. L., L. Andersson, D.L. Newell, J.W. Carey, D. Wildenschild (2014), Pore-scale observations of supercritical CO_2 drainage in Bentheimer sandstone by synchrotron x-ray imaging, International Journal of Greenhouse Gas Control, In Press.

Hilpert, M., and C. T. Miller (2001), Pore-morphology-based simulation of drainage in totally wetting porous media, Advances in Water Resources, 24(3–4), 243-255.

Hughes, R. G., and M. J. Blunt (2000), Pore Scale Modeling of Rate Effects in Imbibition, Transport in Porous Media, 40(3), 295-322.

IPCC (2005), IPCC special report on carbon dioxide capture and storage.

Jamaloei, B. Y., K. Asghari, and R. Kharrat (2012), The investigation of suitability of different capillary number definitions for flow behavior characterization of surfactant-based chemical flooding in heavy oil reservoirs, Journal of Petroleum Science and Engineering, 90–91(0), 48-55.

Juanes, R., E. J. Spiteri, F. M. Orr, Jr., and M. J. Blunt (2006), Impact of relative permeability hysteresis on geological CO_2 storage, Water Resour. Res., 42(12), W12418.

Land, C. (1968), Calculation of imbibition relative permeability for two-and three-phase flow from rock properties, Old SPE Journal, 8(2), 149-156.

Maloney, D. R., M. M. Honarpour, and A. D. Brinkmeyer (1990), The effects of rock characteristics on relative permeabilityRep. NIPER-441; Other: ON: DE90000212 United StatesOther: ON: DE90000212Wed Feb 06 15:58:38 EST 2008NTIS, PC A03/MF A01 - OSTI; GPO Dep.NETL; EDB-90-031427; NTS-90-009616; ERA-15-015946English, Medium: X; Size: Pages: (29 p) pp.

Mayer, A. S., and C. T. Miller (1992), The influence of porous medium characteristics and measurement scale on pore-scale distributions of residual nonaqueous-phase liquids, Journal of Contaminant Hydrology, 11(3), 189-213.

Mayer, A. S., and C. T. Miller (1993), An experimental investigation of pore-scale distributions of nonaqueous phase liquids at residual saturation, Transp Porous Med, 10(1), 57-80.

Mecke, K., and H. Wagner (1991), Euler characteristic and related measures for random geometric sets, Journal of statistical physics, 64(3-4), 843-850.

Mohammadian, S., Geistlinger, H., & Vogel, H.-J. (2014). Quantification of Gas Phase Trapping within the Capillary Fringe Using Micro-CT. *Vadose Zone Journal*. doi:10.2136/vzj2014.06.0063

Morrow, N. R. (1970), Physics and Thermodynamics of Capillary Action in Porous Media, Industrial & Engineering Chemistry, 62(6), 32-56.

Morrow, N. R., I. Chatzis, and J. T. Taber (1988), Entrapment and mobilization of residual oil in bead packs, Journal Name: SPE (Society of Petroleum Engineers) Reserv. Eng.; (United States); Journal Volume: 3:3, Medium: X; Size: Pages: 927-934.

Nguyen, V. H., A. P. Sheppard, M. A. Knackstedt, and W. Val Pinczewski (2006), The effect of displacement rate on imbibition relative permeability and residual saturation, Journal of Petroleum Science and Engineering, 52(1-4), 54-70.

Oh, W., and B. Lindquist (1999), Image thresholding by indicator kriging, Pattern Analysis and Machine Intelligence, IEEE Transactions on, 21(7), 590-602.

Polak, S., Y. Cinar, T. Holt, and O. Torsæter (2011), An experimental investigation of the balance between capillary, viscous, and gravitational forces during CO_2 injection into saline aquifers, Energy Procedia, 4, 4395-4402.

Pruess, K., and N. Müller (2009), Formation dry-out from CO_2 injection into saline aquifers: 1. Effects of solids precipitation and their mitigation, Water Resources Research, 45(3), W03402.

Renard, P., and D. Allard (2013), Connectivity metrics for subsurface flow and transport, Advances in Water Resources, 51, 168-196.

Rivers, M. L., S. R. Sutton, and P. J. Eng (1999), Geoscience applications of x-ray computed microtomography, paper presented at SPIE's International Symposium on Optical Science, Engineering, and Instrumentation, International Society for Optics and Photonics.

Spiteri, E., R. Juanes, M. J. Blunt, and F. M. Orr (2005), Relative-Permeability Hysteresis: Trapping Models and Application to Geological CO_2 Sequestration, paper presented at SPE Annual Technical Conference and Exhibition, Society of Petroleum Engineers.

Suekane, T., N. Zhou, T. Hosokawa, and T. Matsumoto (2010), Direct Observation of Trapped Gas Bubbles by Capillarity in Sandy Porous Media, Transport in Porous Media, 82(1), 111-122.

Vogel, H. J. (2002), Topological characterization of porous media, Morphology of Condensed Matter, 75-92.

Vogel, H. J., U. Weller, and S. Schlüter (2010), Quantification of soil structure based on Minkowski functions, Computers & Geosciences, 36(10), 1236-1245.

Wardlaw, N. C., and L. Yu (1988), Fluid topology, pore size and aspect ratio during imbibition, Transp Porous Med, 3(1), 17-34.

Wildenschild, D., J. Hopmans, M. Rivers, and A. Kent (2005), Quantitative analysis of flow processes in a sand using synchrotron-based X-ray microtomography, Vadose Zone Journal, 4(1), 112-126.

Wildenschild, D., C. M. P. Vaz, M. L. Rivers, D. Rikard, and B. S. B. Christensen (2002), Using X-ray computed tomography in hydrology: systems, resolutions, and limitations, Journal of Hydrology, 267(3–4), 285-297.

4.10 Appendix

4.10.1 Limitations of Connectivity Metrics

Due to the dependence of connectivity metric calculations on very small features, image-derived connectivity metrics are susceptible to various image quality parameters; for example, noise levels, whether the analyzed data volume comprises a representative elementary volume (REV), data resolution, the type of filters applied to the data, segmentation method, and threshold detection method. These factors are examined in the following section in order to assess the practical applicability of the normalized Euler number ($\hat{\chi}$) and gamma function (Γ) connectivity metrics as measures of nonwetting (NW) phase connectivity. In order to facilitate comparison, the data from this study (denoted "APS" data) will be compared to data presented in Herring et.al. [2013] (denoted "OSU" data) which was collected via a polychromatic bench-top x-ray CMT system at Oregon State University (OSU) at a resolution of approximately 10 µm.

4.10.2 Effect of Noise

As noted in section 4.3.2, a limitation of use of the Euler number as a measure of connectivity is that it is sensitive to noise that manifests as incorrectly labeled small isolated NW fluid clusters; the gamma function is a more robust statistical measure in this regard because it incorporates the size of clusters as well as the number. The noise dependence of $\hat{\chi}$ is investigated in Figure 4-10, where different size exclusion filters have been applied to both the binary (segmented) NW data from this study, APS, and the data investigated in Herring et al. [2013], OSU. The relationship between the size exclusion filters of the different data is shown in Table 4-1; the noise removal level used for analysis in Herring et al [2013] and this work is bolded and starred. As shown, despite differences in image resolution and potential noise sources, the size of the applied exclusion filter has no significant effect on either the $\hat{\chi}$-saturation curve or Γ-saturation curves for either data set (Figure 4-10), as long as a minimum level of noise control is applied (e.g. for the high quality APS data, isolated NW clusters of volume less than 52 voxels, or a sphere of radius 13 µm, are removed). Small objects close to the image resolution limit are most prone to segmentation error, and should be removed anyway [H. J. Vogel et al., 2010]. This implies that $\hat{\chi}$ is less sensitive to noise than might be expected, although we note that the impact of noise may become more significant for data of reduced quality.

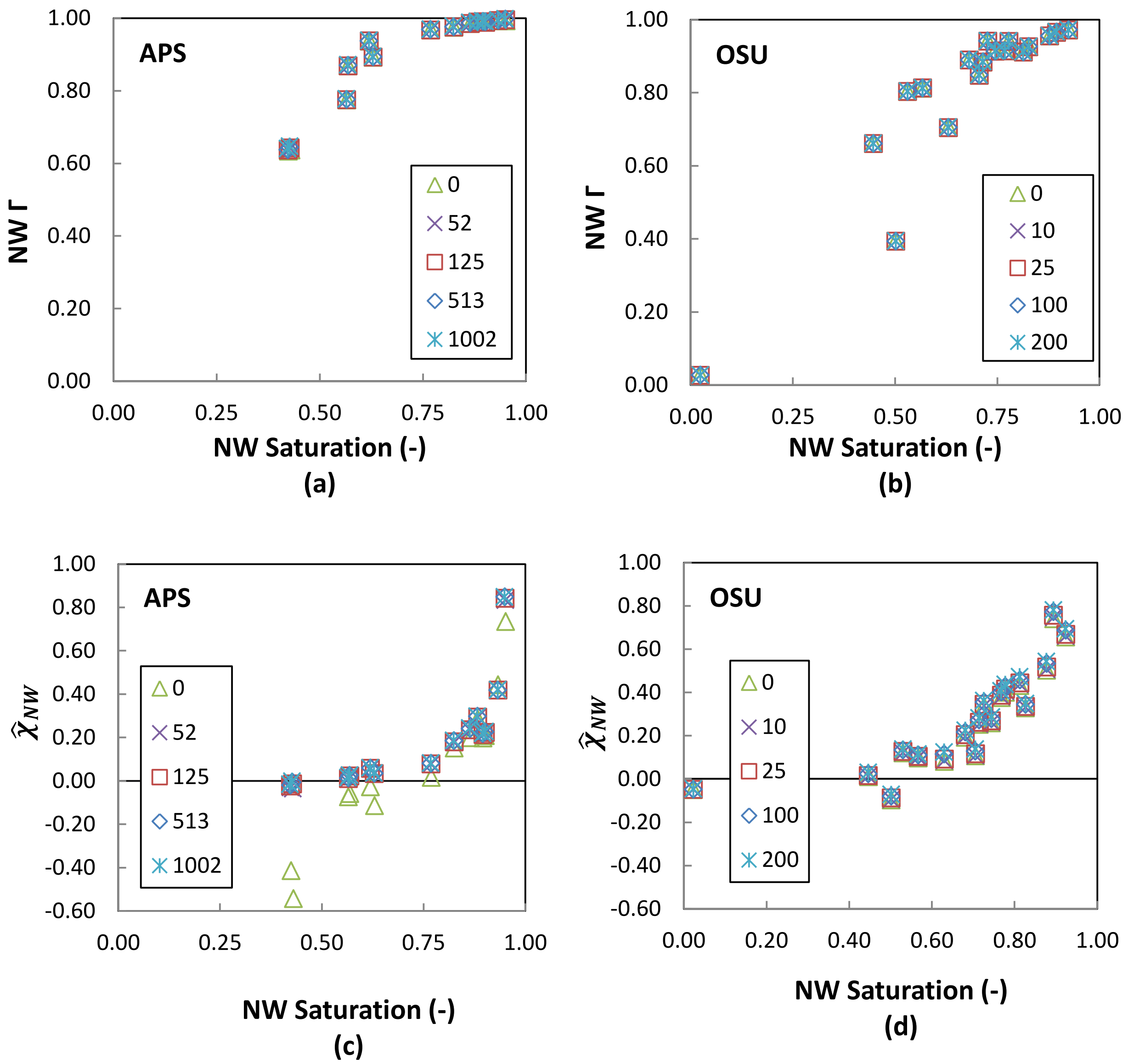

Figure 4-10. Nonwetting (NW) gamma function (Γ) as a function of saturation for (a) APS data and (b) OSU data, and normalized NW Euler value ($\hat{\chi}$) as a function of NW saturation for (c) APS data and (d) OSU data. The relationships are recalculated for different noise removal levels; the size of the applied isolated cluster removal filter, in voxels, is indicated by legend.

Table 4-1. Summary of image quality parameters and size of noise exclusion filters applied to binary data.

	Herring et al, 2013	**This study**
Image Resolution (μm)	10	5.8
Beam Type	Polychromatic	Monochromatic
Data size (voxels)	Cube of 350^3 voxels	Cylinder of 975 voxel diameter, 600 voxel tall
Data size (mm^3)	43	90
Noise Exclusion Filter		
Radius of equivalent spherical volume (μm)	Size of Applied Noise Removal Filter (*voxels*)	
0	0	0
13	10	52
18	25	**125***
29	**100***	513
36	200	1002

*Size of noise exclusion filter applied to data in publication (Herring, Harper et al. 2013) and this work.

4.10.3 Representative Elementary Volume Analysis

Renard & Allard [2013] point out that the Euler characteristic is a local property that is sensitive to the regularity of a structure, i.e. the degree of small-scale heterogeneity or noise which leads to a high number of small objects and holes. Only if the underlying structure exhibits high regularity will the Euler number be a good indicator for global connectivity. However, normalization with the Euler number of the dry data set of the same sample diminishes the requirement of regularity and increases the explanatory power of $\hat{\chi}$ on connectivity. However, connectivity calculations must still be performed on a representative elementary volume (REV) in order to be assumed representative of the overall sample.

Figure 4-11 shows the $\hat{\chi}$ and Γ values for data volumes of increasing size for a range of sample types, including a dry scan, and high and low saturation data for both initial and residual saturations. As shown, a representative elementary volume (REV) for both NW $\hat{\chi}$ and NW Γ is established at approximately 600 x 600 x 600 voxels (x, y, z), equivalent to a physical volume of

40 mm^3. We propose that the normalization procedure thus addresses the local vs. global concerns raised by Renard and Allard [2013].

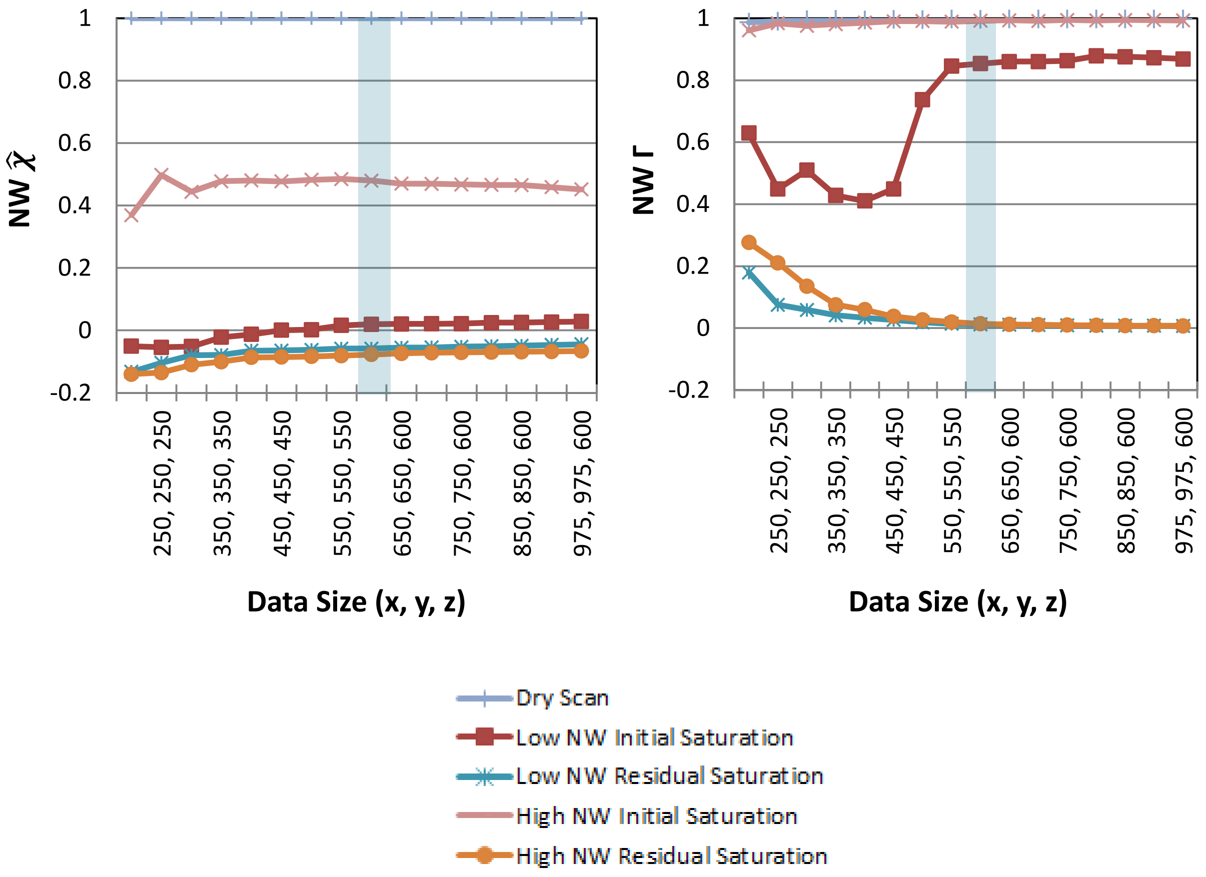

Figure 4-11. (a) Normalized nonwetting (NW) Euler value ($\hat{\chi}$) and (b) NW gamma function (Γ) calculated as a function of data size for a dry sample, as well as data sets representative of high and low nonwetting (NW) saturations at both initial and residual stages of experiment. A representative elementary volume (REV) is achieved at the highlighted data sizes.

4.10.4 Effect of Image Processing and Segmentation Type

To investigate the effect of segmentation method on connectivity parameters, the original OSU data of 350^3 voxel cubes segmented using Indicator Kriging [Oh and Lindquist, 1999] are compared to a reprocessed data set composed of cylindrical subsections (diameter of 706 voxels, height of 1123 voxels) of the raw data with a median filter applied. The same size exclusion filter (100 voxels, or 29 µm spherical radius) was applied to both versions of the binary segmented data to reduce noise which manifests as falsely labeled NW voxels. $\hat{\chi}$-saturation and Γ-saturation curves are shown for both versions of OSU data and compared to the APS data, which was processed via application of a median filter and size exclusion filter of 125 voxels, equivalent to 18 µm spherical radius (Figure 4-12). Using the same processing method produces consistent $\hat{\chi}$-saturation curves for APS and OSU data; however, Γ-saturation curves are different for the APS data and both versions of the OSU data. Both $\hat{\chi}$ and Γ values are sensitive to image processing and segmentation routine; we propose that the higher quality data (in this case, the APS data) be considered to provide a more accurate values.

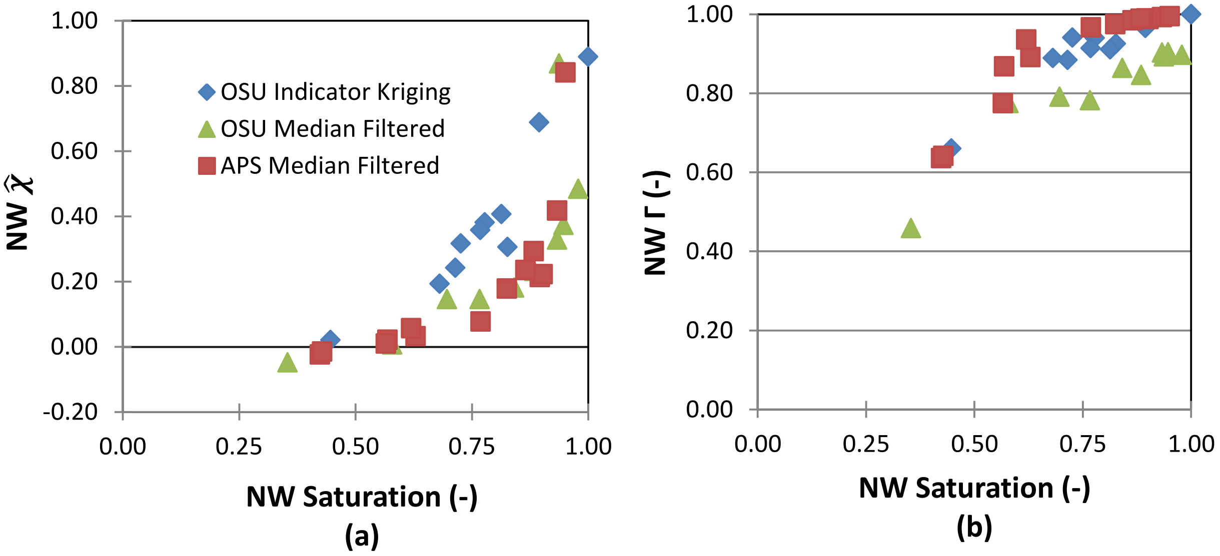

(a)

(b)

Figure 4-12. (a) Normalized nonwetting (NW) Euler value ($\hat{\chi}$) and (b) NW gamma function (Γ) calculated as a function of NW saturation for the median filtered APS data set (resolution of 5.8 µm), the OSU data set published in Herring et al. (2013) which was unfiltered and segmented via Indicator Kriging (10 µm), and the OSU data which was reprocessed by application of a median filter to the original raw data (10 µm).

4.10.5 Effect of Image Resolution

To investigate the impact of resolution on these connectivity metrics, the high-resolution APS data (5.8 µm) can be compared to the relatively low-resolution OSU data (approx. 10 µm). As shown in Figure 4-12, for data sets which have been processed in the same manner as described in Chapter 4.10.2, the shape of the $\hat{\chi}$-saturation curve is not greatly affected by the difference in resolution; however, there is a discrepancy between the Γ-saturation curves for the APS and OSU data.

One aspect of normalization of the Euler characteristic requiring special consideration is the choice of $\chi_{100\%NW}$. In theory, $\chi_{100\%NW}$ should be calculated from an image of a completely dry sample at the same resolution and processed under identical protocol as samples with both W and NW fluid present. The shape of the $\hat{\chi}$-saturation curve is highly sensitive to the value of $\chi_{100\%NW}$, and thus comparison of data sets with different resolutions may lead to inconsistent results. This analysis implies that comparison of connectivity metrics between data sets of different resolution should be approached very carefully. Generally, the image resolution has to be high enough to capture all pore throats that might be drained at high NW saturations with sufficient detail.

4.10.6 Effect of Segmentation Threshold

Some data sets do not exhibit definite peaks in the grayscale histogram, making threshold detection difficult; e.g. the OSU data set (Figure 4-13). For these data sets, the threshold for NW fluid was determined via visual inspection of the data. Figure 4-14 illustrates the deviation in $\hat{\chi}_{NW}$ and NW Γ values for four data sets at initial (drained) state with a range of saturation values. Within a reasonable range (e.g. ±100 grayscale values) NW Γ values exhibit a change of approximately ±5% relative to the nominal grayscale threshold, while $\hat{\chi}_{NW}$ values exhibit a change of ±20% (Table 4-2). For NW $\hat{\chi}$ values, changing threshold value has the most impact on the dry scan, $\chi_{100\%NW}$, for which all pores of sizes close to the image resolution are filled with the NW phase (as compared to scans with wetting fluid present). This reinforces the necessity of accurately processing and segmenting the dry scan, as this value has a major impact on the NW $\hat{\chi}$ calculation of the entirety of the data set.

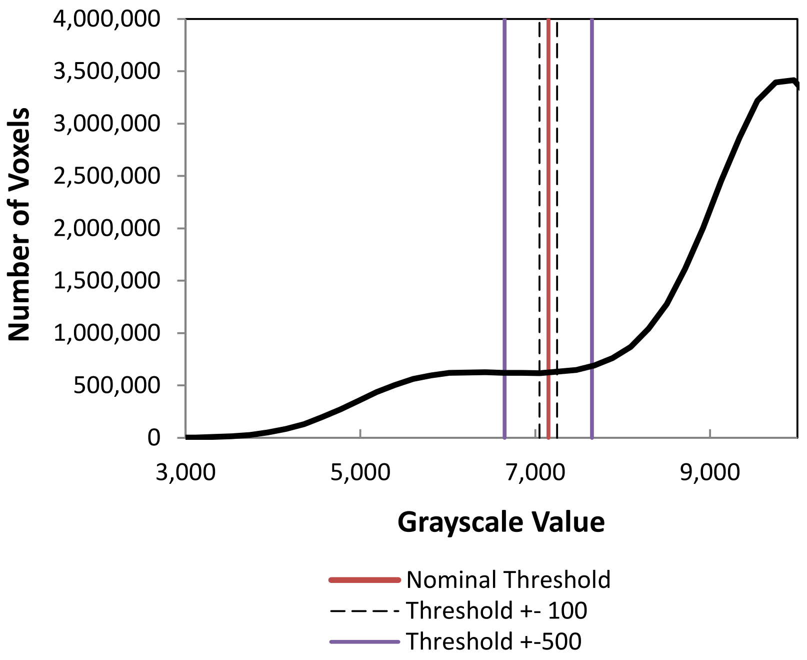

Figure 4-13. Grayscale histogram of example OSU data set. The selected threshold is shown, as are the grayscale values ±100 and ±500 from the selected threshold value.

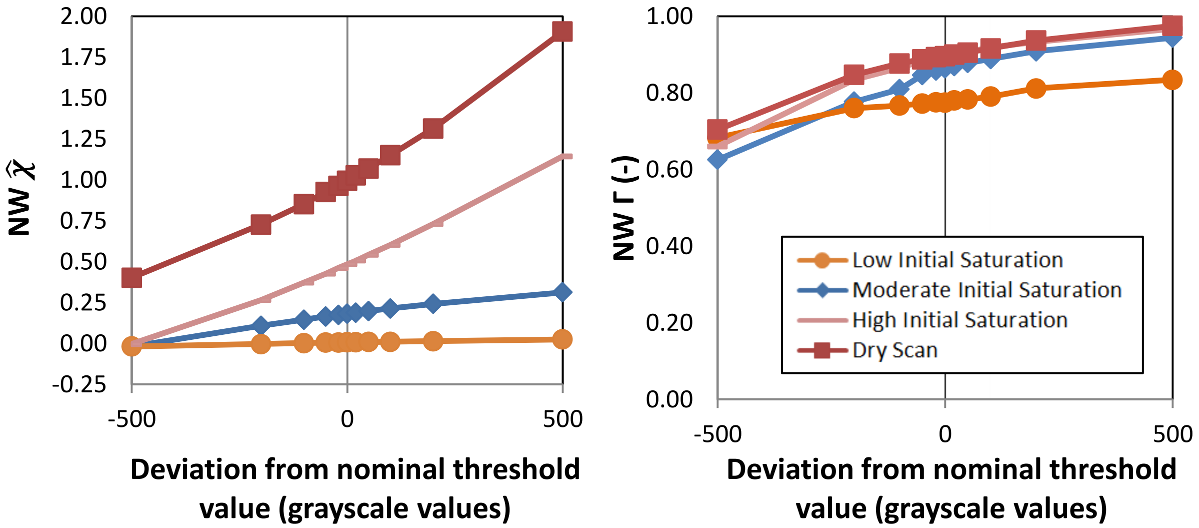

Figure 4-14. The deviations of (a) Normalized nonwetting (NW) Euler value ($\hat{\chi}$) and (b) NW gamma function (Γ) calculated from four different OSU data volumes where the grayscale segmentation threshold has been changed from the predetermined nominal threshold.

Table 4-2. Percent error in connectivity metrics relative to nominal threshold value for OSU data.

Deviation from Nominal Threshold	**-500**	**-200**	**-100**	**-50**	**-20**	**0**	**20**	**50**	**100**	**200**	**500**
Scan Type						**NW Γ (-)**					
High Initial Saturation	-24%	-6%	-3%	-1%	-1%	0%	0%	1%	2%	4%	7%
Moderate Initial Saturation	-24%	-9%	-5%	-2%	-1%	0%	1%	1%	2%	4%	8%
Low Initial Saturation	-9%	-2%	-1%	0%	0%	0%	1%	1%	2%	4%	6%
Dry Scan	-19%	-5%	-2%	-1%	0%	0%	0%	1%	2%	4%	8%
						NW $\hat{\chi}$ (-)					
High Initial Saturation	-62%	-28%	-14%	-7%	-3%	0%	3%	7%	15%	31%	83%
Moderate Initial Saturation	-25%	-9%	-4%	-2%	-1%	0%	1%	2%	4%	8%	17%
Low Initial Saturation	-3%	-1%	-1%	0%	0%	0%	0%	0%	0%	1%	2%
Dry Scan	-75%	-34%	-18%	-9%	-4%	0%	4%	10%	20%	41%	116%

Chapter 5. Impact of Wettability Alteration on Three Dimensional Nonwetting Phase Trapping and Transport

Anna L. Herring[1], Adrian Sheppard[2], and Dorthe Wildenschild[1]

[1]*School of Chemical, Biological and Environmental Engineering, Oregon State University, Corvallis, OR 97331, USA*
[2]*Research School of Physics and Engineering, Australian National University, Canberra, ACT 0200, Australia*

Geophysical Research Letters
2000 Florida Ave. NW, Washington, DC 20009
Submittal expected January 2015

5.1 Abstract

We investigate air and brine capillary trapping and fluid migration via x-ray computed microtomography (x-ray CMT) in Bentheimer sandstone cores which have been treated to exhibit varying wettability. X-ray CMT scans were acquired at multiple steps during the drainage and imbibition processes, as well as at the endpoints; allowing for assessment of the impact of wettability on air saturation, morphology, connectivity, topology, and efficiency of trapping. We find that Bentheimer cores treated with Tetramethoxylsilane (TMS) were rendered weakly water-wet, and cores treated with Octadecyltrichlorosilane (OTS) demonstrate intermediate-wet characteristics. As apparent contact angle increases, residual trapping and trapping efficiency decrease and buoyancy plays a larger role; this may have significant implications for CO_2 migration and trapping during CO_2 sequestration operations.

5.2 Introduction

Geologic sequestration of CO_2 in subsurface reservoirs is a climate change mitigation strategy which prevents carbon emissions to the atmosphere. Sequestration involves capture of CO_2 from the effluent of a large power production point source, pressurization of the CO_2 to reservoir conditions (resulting in a phase transition of the CO_2 to a supercritical fluid), and injection of the supercritical-phase CO_2 ($scCO_2$) into a subsurface storage reservoir. During injection, the CO_2 phase displaces the resident brine of the geologic formation, i.e. a brine drainage process. Subsequently, upward travel of the buoyant CO_2 plume allows for brine imbibition as the brine re-enters the pore space. Accurate prediction of transport and trapping of subsurface CO_2 is necessary to ensure the safety, security, and effectiveness of a CO_2 sequestration operation.

Multiple trapping mechanisms have been identified which prevent CO_2 migration and release at the surface [IPCC, 2005]; one such mechanism is capillary (or residual) trapping, wherein CO_2 is held by capillary forces within the pore structure of the geologic matrix. Capillary trapping decreases the risk of inadvertent leakage of CO_2 (a risk associated with structural trapping); this mechanism also breaks up the injected CO_2 plume into small bubbles, increasing the surface area to volume ratio of the CO_2 and enhancing subsequent dissolution and precipitation reactions. Accordingly, understanding capillary trapping is critical for engineered geologic sequestration. However, current capillary trapping models are based on the premise that the storage rock is primarily water-wet. When exposed to hydrocarbons, or potentially supercritical CO_2, parts of the geologic formation may become intermediate-wet or oil/scCO_2-wet (i.e. hydrophobic); this has implications for storage in depleted oil reservoirs as well as long term storage in saline sedimentary formations [Wan et al., 2014].

Wettability is defined as the affinity of a solid surface for one fluid in the presence of other immiscible fluids. From a pore-scale perspective, wettability can be measured by the contact angle (θ) created by the intersection of the fluid-fluid and fluid-solid interfaces. As measured through the aqueous phase, a contact angle between 0-75^o is considered water-wet, 75-105^o is intermediate-wet, and measurements of 105-180^o are oil/scCO_2-wet [Treiber and Owens, 1972; Anderson, 1987a]. The wettability of a porous medium determines the distribution of wetting and non-wetting fluids within the pore structure and can have a dramatic effect on permeability and connectivity of fluids. Depending on the saturation state of the medium, non-wetting phase fluid clusters tend to occupy the larger pores, while wetting fluid will exist in thin layers throughout the smallest throats and within crevices and roughness on the surface of the medium. As fluids redistribute in a water-wet medium due to changes in saturation or capillary pressure, the non-wetting phase can become isolated and trapped via “snap-off”; this occurs during imbibition, when encroaching wetting fluid film surrounds a nonwetting fluid element in a pore body and the wetting fluid menisci touch as the pore throat constricts. This mechanism will be very different, and potentially completely absent if the system wettability is altered to more oil-wet (or scCO_2-wet). Thus, wettability is a dominant factor controlling the occurrence of snap-off (wetting films are only present in strongly-wetting systems), as well as the morphology and topology of fluid phases within the porous medium, and, it is therefore crucial to understand the degree to which wettability will affect residual trapping of the non-wetting phase for application in CO_2 sequestration scenarios.

The wettability state of a scCO_2-brine-rock system is dependent on complex geochemical, ionic, and physical chemistry interactions, and there is currently no real consensus regarding how interaction with scCO_2 will impact rock surfaces in geologic systems [Wan et al., 2014]. Transition to intermediate wettability after exposure to supercritical CO_2 and brine has been reported for shale minerals [Chiquet et al., 2005], silica micromodels [Kim et al., 2012], sand columns [Plug and Bruining, 2007], and sandstones [Iglauer et al., 2011; Akbarabadi and Piri, 2013; Berg et al., 2013]; however, other studies have reported relative permeability curves [Pini and Benson, 2013], or significant residual trapping of $scCO_2$ during drainage-imbibition studies [Pentland et al., 2011; Krevor et al., 2012] in Berea sandstone, indicative of a water-wet system. In carbonate rocks, Andrew et al. [2014] measured a supercritical CO_2-brine in-situ average contact angle of approximately 45^o, while El-Maghraby and Blunt [2013] report that experiments with Indiana Limestone show increased levels of residual trapping of CO_2 under elevated temperature and pressure; they deduce that geochemical reactions force the system to a more strongly water-wet state than the same system at lower pressure. Given the range of observed wetting behavior, it seems prudent to further explore how wettability alteration affects CO_2 migration and capillary trapping.

A number of previous studies have investigated the impact of wettability on oil recovery. A pattern of minimum residual oil saturation at intermediate rock wettability and increased residual oil saturation at strongly water-wet and strongly oil-wet conditions is established in a review by Anderson [1987] (which presents the experimental results of Lorenz et al. [1974], Kennedy et al. [1955]; and Amott [1959]); as well as in more recent experimental work by Morrow [1990]. This pattern is due to a combination of several factors. Snap-off dominates in water-wet conditions, leading to high residual oil saturations. Under intermediate conditions, both fluids can easily flow through small constrictions; snap-off is suppressed [Mahmud and Nguyen, 2006], and oil can remain connected via smaller pore throats and drain to low residual saturation. Under oil-wet conditions, snap-off with respect to the oil-phase does not occur, but oil resides in the small pore spaces and throats of the media, again resulting in relatively high residual oil saturations. Blunt [1998] performed numerical simulations which demonstrate a similar pattern to the experimental results described above, but also indicate reduced residual saturations in strongly oil-wet ($\theta>135^o$) media due to the formation of oil films which allow oil to drain to very low saturations.

Supercritical CO_2 is less viscous than brine, resulting in inverted viscosity ratio (sometimes called mobility ratio) as compared to oil-brine systems. Additionally, gravity/buoyancy forces are generally stronger for $scCO_2$-brine systems due to the relatively large density difference between $scCO_2$ and brine; these differences in fluid properties limit the applicability of oil recovery literature to $scCO_2$-brine systems. Flow patterns have been studied for a wide range of viscosity ratios and capillary number in water-wet two dimensional (2D) systems [Lenormand et al., 1988; Zhang et al., 2011]; however, similar flow regimes are not well-defined for systems of intermediate wettability, or for three dimensional (3D) systems which are affected by gravity forces. In one of only a few supercritical condition studies, Chaudhary et al. [2013] measured residual saturation of supercritical CO_2 in glass (water-wet) and teflon ($scCO_2$-wet) bead cores, and found that residual trapping was greatly reduced in the $scCO_2$-wet system; however, the bead systems used in that study have large pore spaces, the size of which impacts the relative importance of snap-off and fluid-solid adhesive forces, and thus may not be directly applicable to natural geologic systems.

The impact of wettability alteration on capillary trapping of $scCO_2$ during geologic sequestration operations is difficult to investigate due to the inherent difficulty involved in conducting and quantifying wettability during supercritical-condition experiments. In this work we use an ambient-condition system of air, brine, and Bentheimer sandstone. This experimental system approximates the capillary, gravitational, and viscous forces present in a $scCO_2$-brine-sandstone system [Herring et al., 2014]; provides an unstable viscosity ratio during drainage, as in a $scCO_2$-brine system; and also allows for investigation of buoyancy driven flow. Bentheimer sandstone cores were treated to produce three wettability states: water-wet (plasma cleaned, but otherwise untreated sandstone core), weakly water-wet (cores treated with Tetramethoxylsilane, denoted “TMS”), and intermediate-wet (cores treated with Octadecyltrichlorosilane, denoted “OTS”). For consistency, we refer to “drainage” as brine withdrawal from the core, “imbibition” as brine entering the core, and air is described as the nonwetting phase, regardless of the actual wettability state. Nonwetting phase (air) saturation and distribution is quantified via x-ray computed microtomography (x-ray CMT), and paired with capillary pressure measurements obtained throughout the flow process.

5.3 Materials and Methods

5.3.1 Sandstone Cores and Silane Treatment

All experiments are conducted on Bentheimer sandstone cores with a diameter of 4.9 mm and lengths ranging 8.5-10.0 mm, which were cleaned via radio-frequency plasma treatment for at least 5 minutes at 50 watts and approximately 0.15 torr [Liston, 1989]. TMS treatment was applied to cores via vapor-phase deposition, under low vacuum conditions, for a period of at least 12 hours. For liquid-phase deposition with OTS, cores were first saturated under vacuum with dodecane for 25 minutes; then approximately 15 pore volumes of a solution of 5% by mass OTS/dodecane was flushed through the core several times over a period of 24 hours. After the OTS/dodecane flushing stage was complete, 30 pore volumes of toluene was flushed through the core to remove the OTS/dodecane solution from the pore space, and the core was placed under vacuum to volatize toluene from the core. In addition to these silane-treated cores, flow experiments were also conducted on non-treated (plasma cleaned) water-wet (WW) cores. For each treatment type, a glass slide was subjected to the same treatment for contact angle measurement, which was accomplished using the sessile drop method in a goniometer.

Air-water contact angles are measured for the glass slides and assumed to represent idealized conditions within the pore space of the rock; this assumption is checked subsequently via inspection of pressure-saturation curves and tomographic data. After treatment, rock cores were wrapped with one layer of Teflon tape, and stored in vials filled with MilliQ water when not in use.

5.3.2 Core Holder Assembly and Flow Processes

All experiments are imaged in a titanium core holder (manufactured in-house at the Australian National University, ANU) which allows for favorable x-ray penetration (wall thickness of 0.120 mm). The sandstone sample was wrapped in Teflon tape and inserted into the core holder onto a circular hydrophilic nylon membrane with pore size of 1.2 μm (General Electric Company, Fairfield CT, United States), which is mounted on top of a Buna-N nitrile o-ring. The semi-permeable membrane, set flush to the bottom of the core, prevented air breakthrough through the core and into the lines below the sample. The fluid flow lines (made of PEEK material) are connected in series to a Keller Series 35X pressure transmitter with a range of 0 - 1.2 bar and accuracy of 0.1 mbar (Keller America, Inc., Newport News, VA, United States) and a Harvard PHD2000 syringe pump (Harvard Apparatus, Holliston MA, United States).

During experiments, a Bentheimer sandstone core was first saturated under vacuum with brine to establish conditions representative of a reservoir prior to injection, and a scan was acquired to ensure complete brine saturation was achieved; all experiments began with an original air saturation (S_O) of 0%. A small flexible air-tight air reservoir was placed over the top of the core holder to reduce evaporation from the core. Brine was then withdrawn at 0.3 µl/min while air entered the sample from the top of the core (drainage) to the initial NW phase saturation endpoint (S_I). Subsequently, brine was pumped into the bottom of the core (imbibition) at 0.3 µl/min until negative capillary pressure readings indicated residual conditions (S_R). Scans were collected at S_O, S_I, and S_R points; additionally, the pump was halted and intermediate scans were acquired at multiple points throughout the drainage and imbibition flow processes, providing information about fluid configurations at transitional points.

5.3.3 X-ray Microtomographic Imaging and Processing

X-ray CMT scans were acquired at the ANU µCT facility. X-rays are generated by a GE-Phoenix xs180nf micro-focus x-ray source, and radiographs are captured by a 2048 x 2048 pixel Perkin Elmer XRD 1621 CNES amorphous silicon flat-panel x-ray detector, coated with a cesium iodide scintillator. Depending on sample placement relative to the detector, each data set had a slightly different voxel resolution value, ranging from 3.2 µm to 3.8 µm per voxel edge. X-ray tube settings were 80 kV and 110 µA for all scans except one OTS data set, which was mistakenly imaged at a much lower accelerating voltage of just 30 kV. Depending on energy settings and height of the imaged section, scans typically required 1.5-2.5 hours to collect at least 6000 projection angles on a helical scanning trajectory at 0.14 degree angle spacing. The precise number of projections depended on the length of the core plug. Reconstruction was accomplished using helical cone-beam filtered backprojection [Varslot et al., 2011]. Figure 5-1 provides an example of the data processing procedure: For each grayscale data volume (Figure 5-1a), a cylindrical subsection of the center of the core, approximately 4 mm in diameter, was chosen to exclude influence on flow and trapping from the core holder walls, and three iterations of a three-dimensional (3D) median filter were applied (Figure 5-1b). The segmentation threshold was set to the grayscale value corresponding to the local minimum separating the air and combined solid/brine phases in the grayscale histogram (Figure 5-1c). The resulting segmented volumes were denoised to exclude falsely-labeled air phase voxels by removing isolated air phase features smaller than 700 voxels (equivalent to a sphere with a radius of approximately 20 µm), this is consistent with the pore size distribution of Bentheimer sandstone reported by Maloney et al. [1990]. All reported quantitative measures are calculated on this final binary image of air phase (Figure 5-1d).

To add additional information to the study, the data obtained with the µCT at ANU was also compared with existing data from similar drainage experiments in untreated, water-wet Bentheimer sandstone cores (labeled "WW APS"), details of which were reported by Herring et al. [2014]. The WW APS data was collected at the Advanced Photon Source (APS) at Argonne National Laboratory from experiments conducted with a significantly higher drainage flow rate (3.3 µl/min) than the new data presented here.

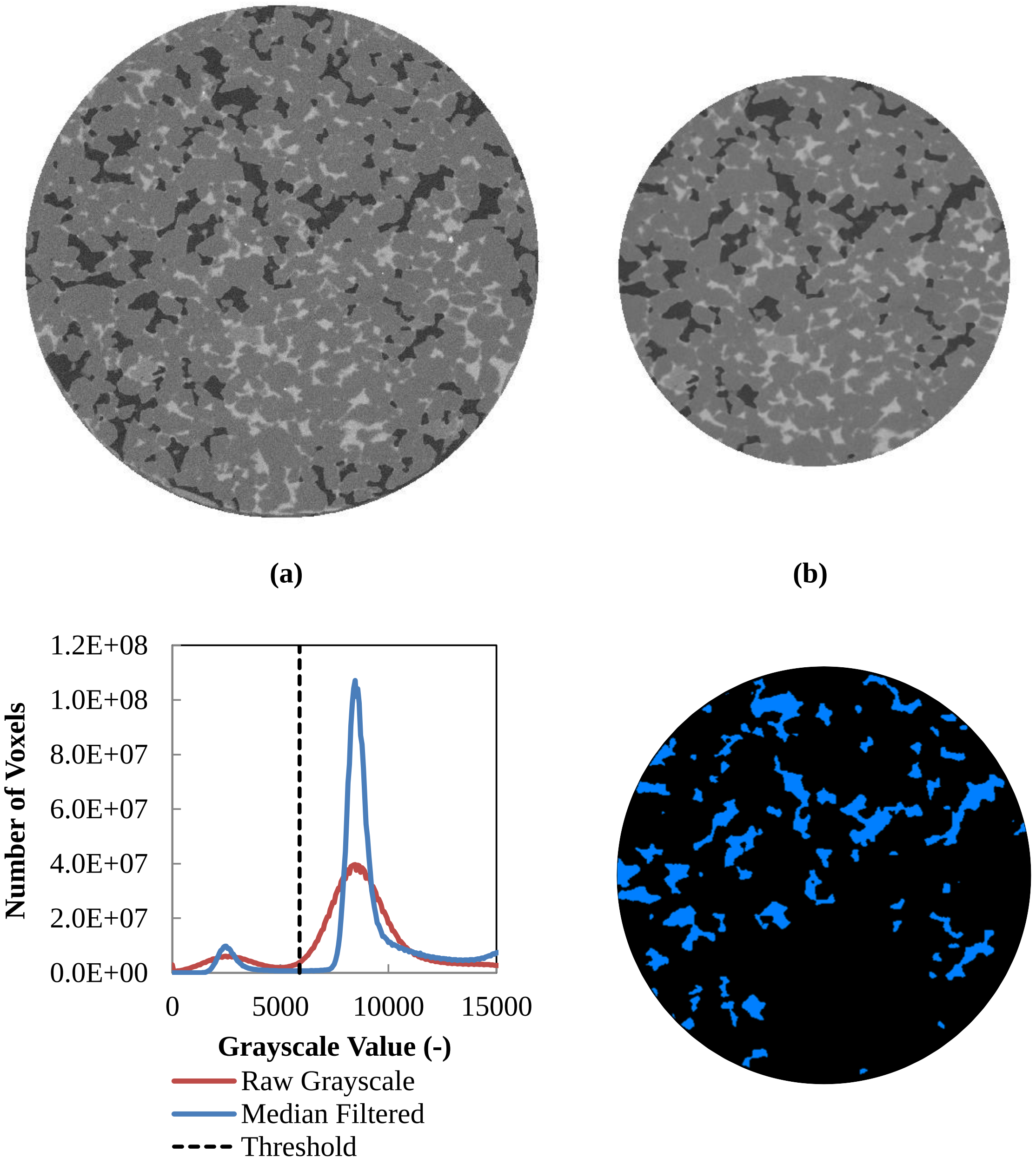

(a)

(b)

(c)

(d)

Figure 5-1. Data processing procedure for x-ray microtomographic data. Grayscale data (a) is cropped and filtered with three iterations of a three dimensional (3D) median filter (b), after which the grayscale histogram minimum between the air phase and solid phase is determined (c). This minimum value is the threshold value which defines which voxels represent air phase (d), upon which all subsequent quantitative measures are calculated.

5.4 Results

5.4.1 Effect of Wettability Treatment

Representative capillary pressure-saturation (P_c-S) drainage curves for the three treatments are presented in Figure 5-2; air saturation values are measured from x-ray CMT data and paired with average pressure readings measured during the time of the scan. As shown, for the drainage process (Figure 5-2) the capillary pressure is relatively high for untreated (water-wet, WW) cores, while weakly water-wet (TMS) and intermediate wet (OTS) cores demonstrate significantly lower capillary pressures for a given saturation. Additionally, TMS and OTS cores exhibit significantly higher irreducible water saturations relative to the WW core. These characteristics are indicative of increased contact angle [McDougall and Sorbie, 1995; Bradford et al., 1997; Chalbaud et al., 2007].

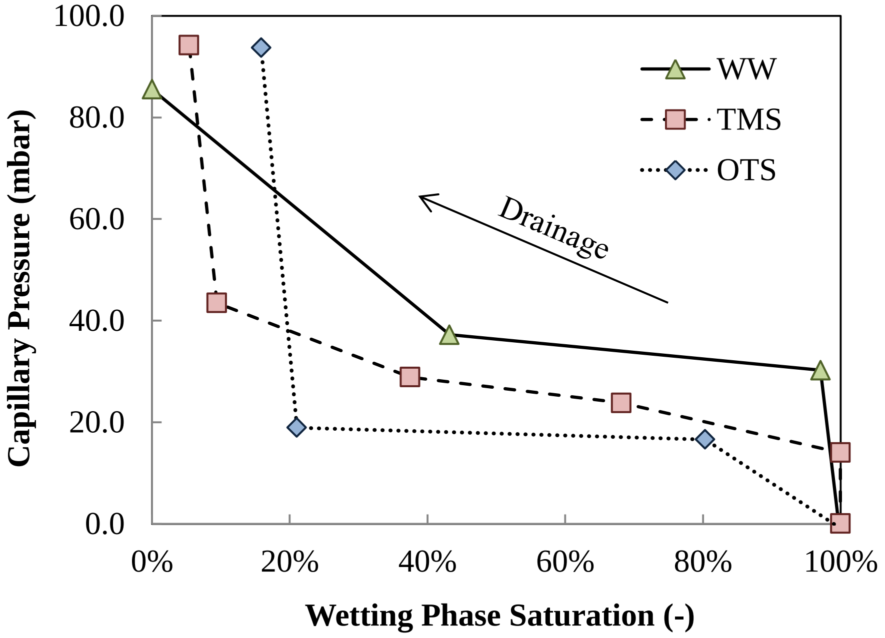

Figure 5-2. Measured capillary pressure paired with x-ray tomographic image derived saturation values for the brine drainage process in wettability-altered Bentheimer sandstone cores. Wettability is classified as water-wet (WW), weakly water-wet (TMS), and intermediate-wet (OTS).

Contact angles of the treated cores are estimated from drainage P_c-S curves using the Young-Laplace equation:

$$P_c = \frac{2\sigma}{r} cos\theta$$

$$\theta_i = cos^{-1}\left(\frac{P_{C,i}}{P_{C,WW}}\ cos\theta_{WW}\right) \qquad \text{eqn. 5.1}$$

Where P_c is the capillary pressure (the difference between the air and brine pressure), σ is the interfacial tension between air and brine, and r the radius of the interface between the two phases, and θ is the contact angle, measured through the aqueous phase. Values of estimated contact angle are presented in Table 5-1, these values are calculated from capillary pressure values at approximately 60% air saturation (40% brine saturation). This estimation assumes σ and r are constant for the cores, and that the water-wet contact angle for the sandstone cores, $\theta_{WW} \approx 5^o$. Also presented in Table 5-1 are the contact angle values measured from treated glass slides.

Table 5-1. Contact angle measurements for Bentheimer sandstone and glass slide surfaces treated with Tetramethoxylsilane (TMS), Octadecyltrichlorosilane (OTS), compared to an plasma cleaned, untreated (WW) surfaces.

	Estimated from drainage P_c-S curve	**Average measure from treated* glass slide**		**Wettability Designation**
		Advancing	*Receding*	
WW	-	5^o	5^o	Strongly water-wet
TMS	42^o	73^o	69^o	Weakly Water-wet
OTS	60^o	108^o	96^o	Intermediate-wet

*Treatment of WW glass slide consisted of radio-frequency plasma cleaning only

The contact angles estimated from the P_c-S curves are shifted toward water-wet by 30^o (for TMS) and 40^o (for OTS) relative to the values measured on the treated glass slides. This inconsistency could be due to treatment constraints: the silanization treatment is limited by diffusive transport within the sandstone pore-space, while the glass slide surface is easily accessible to the OTS and TMS molecules. In addition, Bentheimer is not pure quartz and so the surfaces being coated are not exclusively silica. These factors may result in reduced coverage of the pore space with silane as compared to the glass slides. The OTS glass slide contact angle measurements agree with a value of 106^o reported by Araujo et al. [1995], while the values estimated from the P_c-S curve is in good agreement with values reported by Bradford and Leij [1995] (64.9^o advancing and 38.0^o receding) who also estimated contact angle from P_c-S data of OTS treated media. For further interpretation of the data, contact angles are assumed to be equivalent to those estimated from P_c-S curves; untreated cores are considered to represent water-wet conditions (labeled "WW"), TMS treated cores are considered to be weakly water-wet ("TMS"), and OTS treated cores represent intermediate-wet conditions ("OTS").

5.4.2 Evolution of NW phase During Drainage

The topology of the nonwetting phase after drainage has been shown to have a distinct impact on the mobilization (trapping) of nonwetting phase after imbibition [Herring et al., 2013, 2014]. A metric of topology, the Euler number, relates the number of individual, independent fluid clusters to the number of redundant connections (e.g. pore throats) within fluid clusters. Herring et al. [2013, 2014] divide the Euler number of each data volume by the Euler number of the same medium at 100% nonwetting phase saturation, resulting in a normalized Euler number ($\hat{\chi}_{NW}$) which ranges from negative values (indicating disconnected nonwetting phase) to a maximum value of 1.0 (indicating maximum interconnectivity of nonwetting phase). The relationship between nonwetting phase-normalized Euler number and nonwetting phase saturation ($\hat{\chi}_{NW}$-S) is shown in Figure 5-3; for comparison, "WW APS" data [Herring et al., 2014] is also presented.

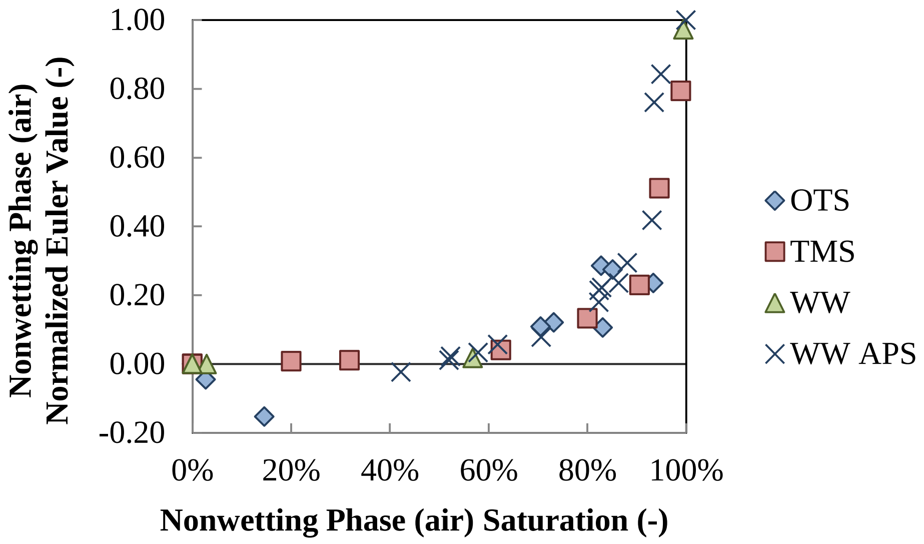

Figure 5-3. Normalized nonwetting Euler values ($\hat{\chi}_{NW}$) during brine drainage as a function of nonwetting phase saturation in Bentheimer sandstone of intermediate wettability ("OTS"), weakly water-wet wettability ("TMS"), and water-wet wettability ("WW" and "WW APS"). All drainage experiments were performed at a brine drainage flow rate of 0.3 µl/min, with the exception of the WW APS data set, which was drained at 3.3 µl/min.

The WW, OTS, TMS, and WW APS data all follow the same $\hat{\chi}_{NW}$-S relationship, up to approximately 80% air saturation, at which point OTS data points deviate from the rest of the data. This implies that the evolution of nonwetting phase topology with nonwetting phase saturation is independent of flow rate, as the results of this study (flow rate of 0.3 µl/min) agree well with the WW-APS data (flow rate of 3.3 µl/min). However, our data suggests that wettability does impact nonwetting phase topology. OTS data reaches a maximum $\hat{\chi}_{NW}$ value of approximately 0.3 during drainage even though a relatively high capillary pressure value is achieved (Figure 5-2); this can be attributed to the absence of water films in the intermediate-wet system: all brine which remains in the sandstone pore space is disconnected and lacks a path to drain from the sample. Our experimental set-up controls capillary pressure by decreasing the brine-phase pressure (rather than by increasing the air-phase pressure), so disconnected brine remains stable in the pore space, and air is unable to invade the pore throats required to reach high $\hat{\chi}_{NW}$ values; resulting in the cluster of OTS points at approximately $\hat{\chi}_{NW}$ of 0.3 and 80% air saturation.

An alternative measure of nonwetting phase connectivity is the gamma function (Γ), which describes the likelihood that a nonwetting-labeled fluid voxel is connected to all other nonwetting fluid voxels [Renard and Allard, 2013; Herring et al., 2014]. As Γ approaches 1.0, the likelihood that all nonwetting fluid clusters are connected to each other increases. Figure 5-4 presents Γ as a function of air phase saturation during drainage. As shown, for low to moderate (0-60%) air phase saturation, air invasion in the cores follows a trend of Γ of OTS>TMS>WW. This connectivity analysis quantitatively demonstrates that NW fluid migration patterns are dependent on wettability.

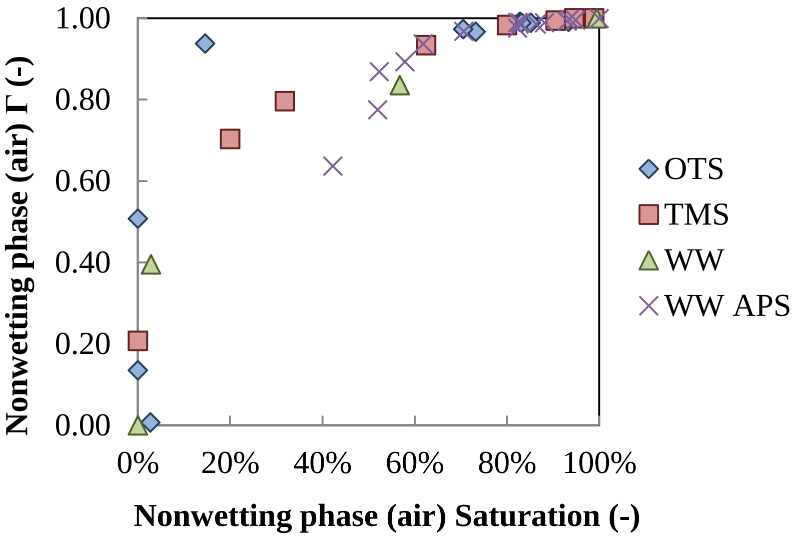

Figure 5-4. Connectivity of nonwetting phase (air) during brine drainage as quantified by the gamma value (***Γ***) as a function of nonwetting phase saturation in Bentheimer sandstone cores of intermediate wettability ("OTS"), weakly water-wet wettability ("TMS"), and water-wet wettability ("WW" and "WW APS"). All drainage experiments were performed at a brine drainage flow rate of 0.3 µl/min, with the exception of the WW APS data set, which was drained at 3.3 µl/min.

For qualitative comparison, we present 2D vertical cross-sections of air intrusion in the cores at 15% and 20% air saturation for OTS and TMS cores (Figure 5-5); unfortunately, no tomographic images of similar low saturation levels were obtained for WW cores, since the exact saturation at which the tomographic snapshot were taken depended on difficult-to-control experimental parameters. Visually, air flow in the OTS core is more compact, while the TMS data volume exhibits longer fingering.

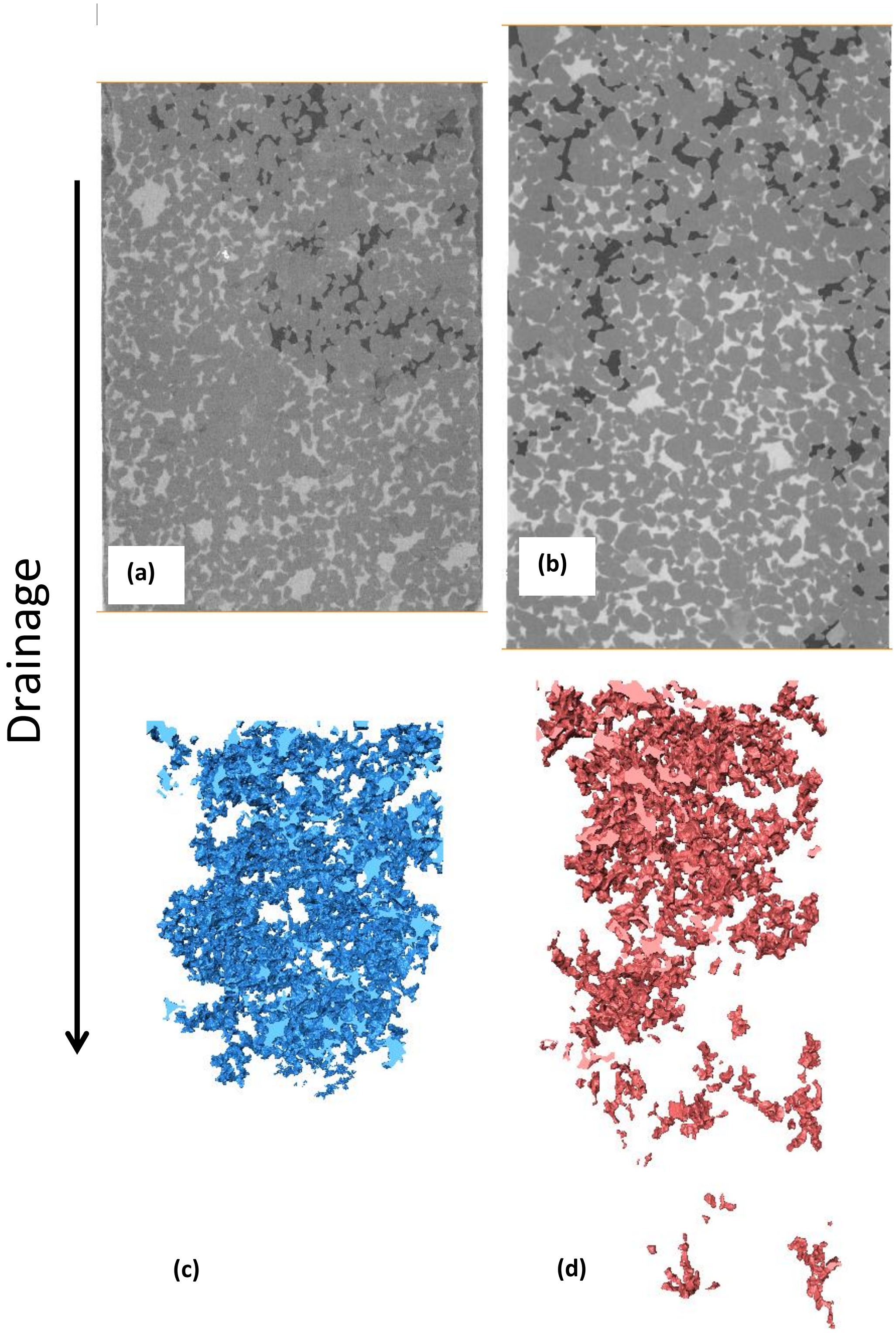

Figure 5-5. Vertical cross-sections of x-ray microtomography images of air intrusion into (a) an intermediate-wet, OTS core and (b) a weakly water-wet, TMS core; along with three-dimensional (3D) renderings of air intrusion for the same (c) OTS core at 15% air saturation, and (d) TMS core at 20% air saturation.

The vertical distributions of air saturation for these treated volumes are shown in Figure 5-6. We recognize that the two profiles represent a 5% difference in air saturation, however, this is a relatively small difference and both represent an early-stage drainage regime where the air phase is not yet well-connected. The OTS volume exhibits a sharp decrease in air saturation approximately 3.5 mm from the top of the core, and the slope of the linear regression of the OTS data is less steep and less linear (lower R^2 value), which quantitatively demonstrates a sharper drainage front.

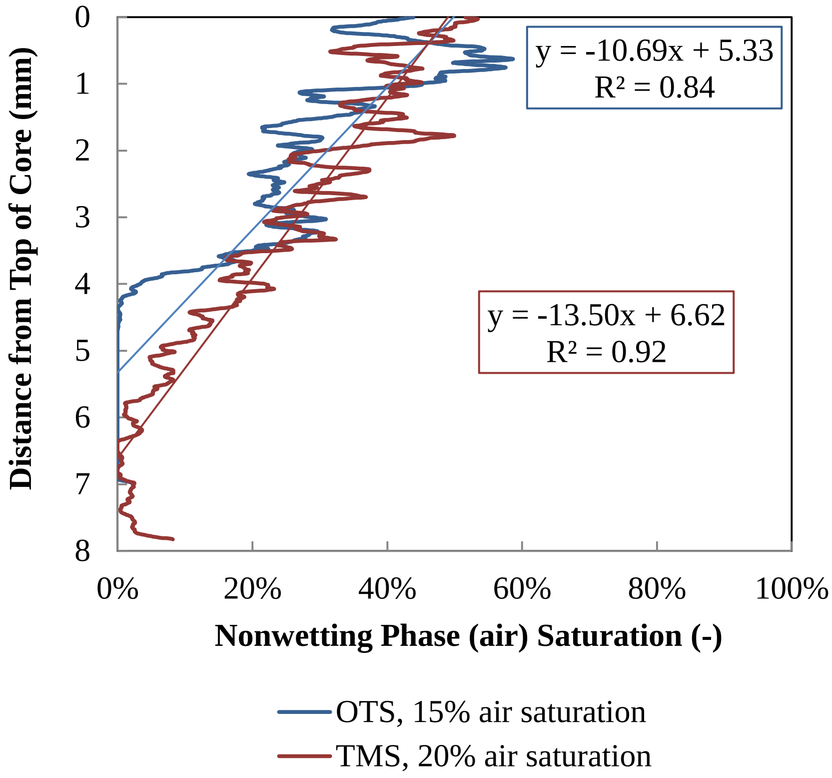

Figure 5-6. Vertical distribution of air saturation measured at early drainage conditions for an intermediate-wet OTS core (overall air saturation of 15%), and a weakly water-wet TMS core (20% overall air saturation).

These differences in flow pattern are not predicted by standard flow regime models. Previous experimental work in 2D micromodels has led to the development of flow regimes as a function of mobility ratio (ratio of invading to defending phase viscosities, $M = \mu_{INV}/\mu_{DEF}$) and capillary number (Ca) [Lenormand et al., 1988; Zhang et al., 2011]. Capillary number is sometimes defined to include contact angle (e.g. Jamaloei et al. [2012]):

$$Ca = \frac{\mu_{INV} v_{INV}}{\sigma \cos\theta} \qquad \text{eqn. 5.2}$$

where μ_{INV} is the invading phase viscosity and v_{INV} is the invading phase velocity. Using this definition of capillary number, and using contact angle values as estimated from the P_c-S curves (Figure 5-2 and Table 5-1), the experiments of this study are shown on the previously developed phase diagram, after Lenormand et al. [1988] and Zhang et al. [2011] (Figure 5-7). Based on this description of flow pattern regimes, the OTS, TMS, and WW data should exhibit similar flow patterns in capillary fingering regime. However, the connectivity analysis (Figure 5-4) and the visualization and distribution of flow presented in Figures 5-5 and 5-6 contradicts this supposition.

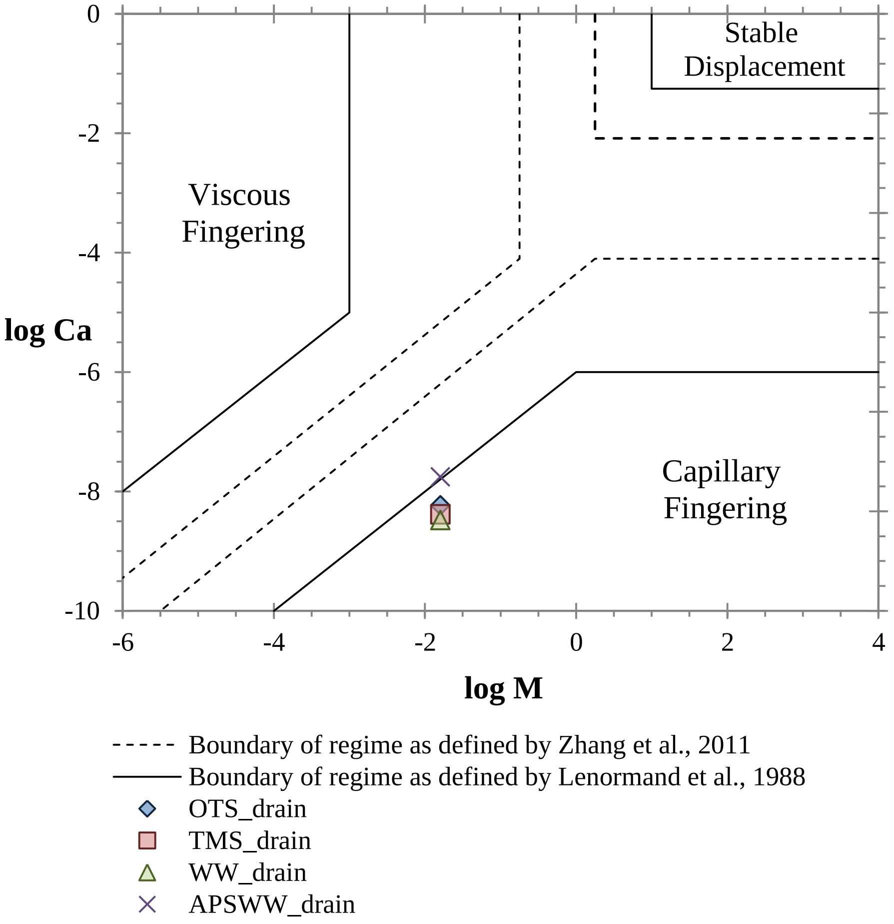

Figure 5-7. Classification of drainage flow regime in Bentheimer sandstone as a function of capillary number (as defined in equation 2) and mobility ratio (ration of invading to defending phase viscosities, $M = \frac{\mu_{INV}}{\mu_{DEF}}$), after Lenormand et al. [1988] and Zhang et al. [2011]. Wettability is classified as water-wet (WW and WW APS), weakly water-wet (TMS), and intermediate-wet (OTS).

We suggest that the observed flow patterns are due to a decrease in capillary forces, and relative increase in gravity forces. The Bond number defines the relative importance of gravitational to capillary forces and does not traditionally include contact angle; however, in this study we define the Bond number as:

$$Bo = \frac{\Delta\rho \cdot g \cdot d^2}{\sigma \cdot \cos\theta} \qquad (0^o \leq \theta < 90^o) \qquad eqn. 5.2$$

where Δρ is the difference in density between fluids, g is the gravitational constant, and d is a length scale (in this case we use the average grain diameter). The inclusion of contact angle in this formulation is a necessary change for finite contact angles since the strength of capillary forces, which form the denominator, are proportional to $\sigma \cdot \cos\theta \,/\, d$. As contact angle increases to intermediate wet conditions (90^o), Bond number increases, indicating a transition to buoyancy driven flow.

Conceptually, the observed air flow patterns are due to a combination of factors. For a water-wet (or weakly water-wet) medium, nonwetting fluid preferentially travels through larger pore bodies and throats due to capillary interactions, causing fingering; however, in an intermediate-wet medium, flow is less dependent on the pathway size. Additionally, contact angle increases result in higher Bond number values, causing gravity separation and contributing to the relatively sharp delineation between the more buoyant air phase and the aqueous brine phase below. The range of Bond numbers of these experiments (1.5×10^{-3} to 2.9×10^{-3}) is similar to that of supercritical CO_2-brine-sandstone systems (as per analysis by Herring et al. [2014]), indicating that potential wettability changes could have a surprisingly large effect on CO_2 migration due to buoyancy influencing pore scale displacement patterns for intermediate-wet systems.

The quantitative connectivity analysis (Figure 5-4), along with qualitative visualization (Figure 5-5), indicate that the shape of the drainage front is strongly dependent on wettability state and the resulting relative importance of capillary and gravity forces.

5.4.3 Trapping Trends

The effect of wettability state on (a) residual air saturation, S_R, and (b) trapping efficiency (residual nonwetting saturation, S_R, normalized by initial nonwetting saturation, S_I) is presented in Figure 5-8. As noted above, air distribution in OTS cores is strongly dependent on buoyancy forces, and so the single OTS data volume is presented as air saturation of the top 3 mm of the core, bottom 3 mm, and whole core. Residual saturation and trapping efficiency is highest in the upper 3 mm of OTS treated cores, followed by WW untreated cores and TMS treated cores, with the bottom 3 mm of OTS treated cores showing the lowest trapping efficiency. Duplicates of the WW and TMS experiments demonstrate that these experiments are highly repeatable; however, only one OTS experiment was completed through the full drainage and imbibition cycle due to experimental complications.

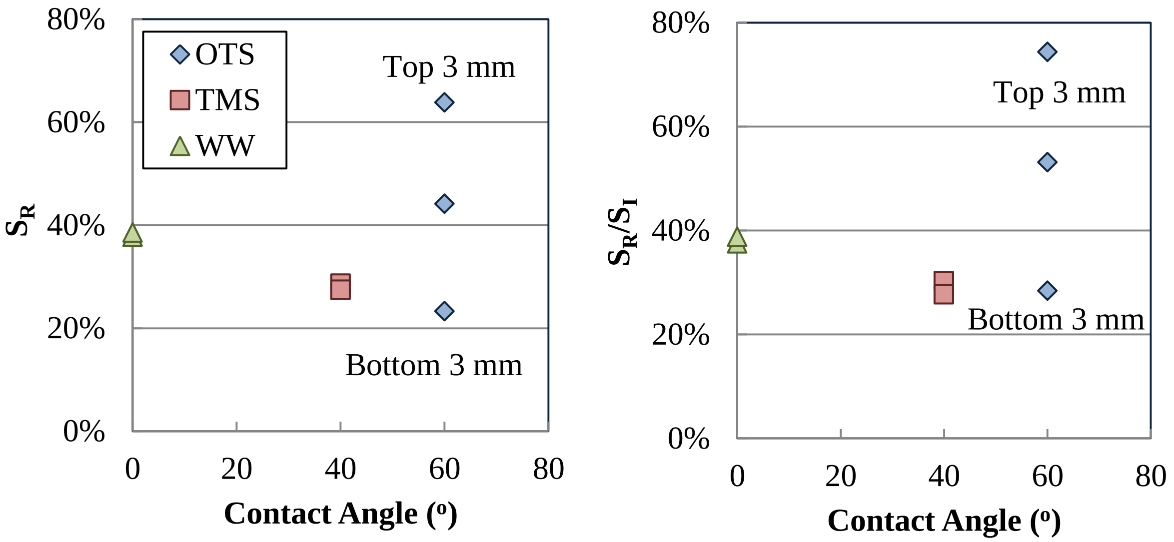

Figure 5-8. (a) Residual trapping (S_R), and (b) trapping efficiency (residual saturation normalized by initial saturation, S_I) of air as a function of contact angle (estimated from the capillary pressure-saturation curves of drainage) of Bentheimer sandstone cores of intermediate wettability ("OTS"), weakly water-wet wettability ("TMS"), and water-wet wettability ("WW"). The data from the OTS experiment is shown as the saturation calculated from the upper 3 mm of the core, the bottom 3 mm of the core, and the whole core (unlabeled). WW and TMS data are whole core values.

Vertical distributions of residual air saturation in WW and TMS experiments are uniform with depth; however, the vertical distribution of air in the OTS core is highly variable and depth dependent (Figure 5-9).

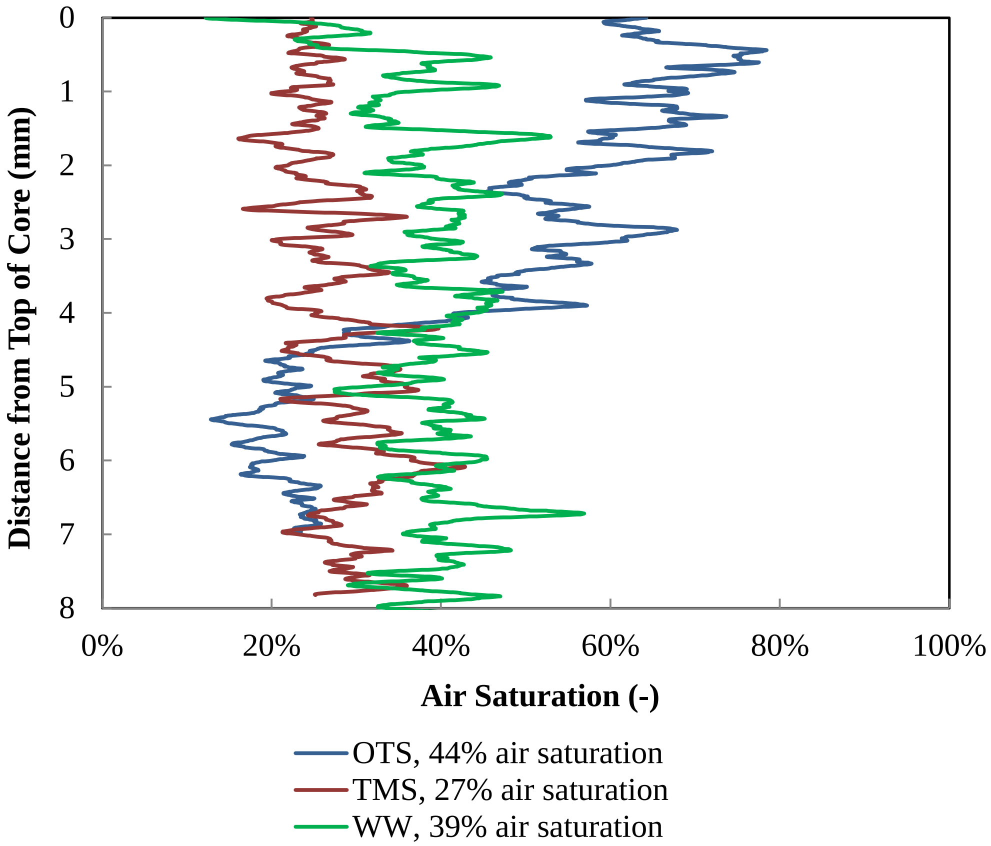

Figure 5-9. Vertical distribution of air saturation measured at the end of imbibition for a water-wet WW core (overall air saturation of 39%), a weakly water-wet TMS core (27% overall air saturation), and an intermediate-wet OTS core (overall air saturation of 44%).

The relative uniformity of residual air in WW and TMS cores, and nonuniformity of air distribution of the OTS core is also visible in air-phase isosurfaces of the residual state (Figure 5-10).

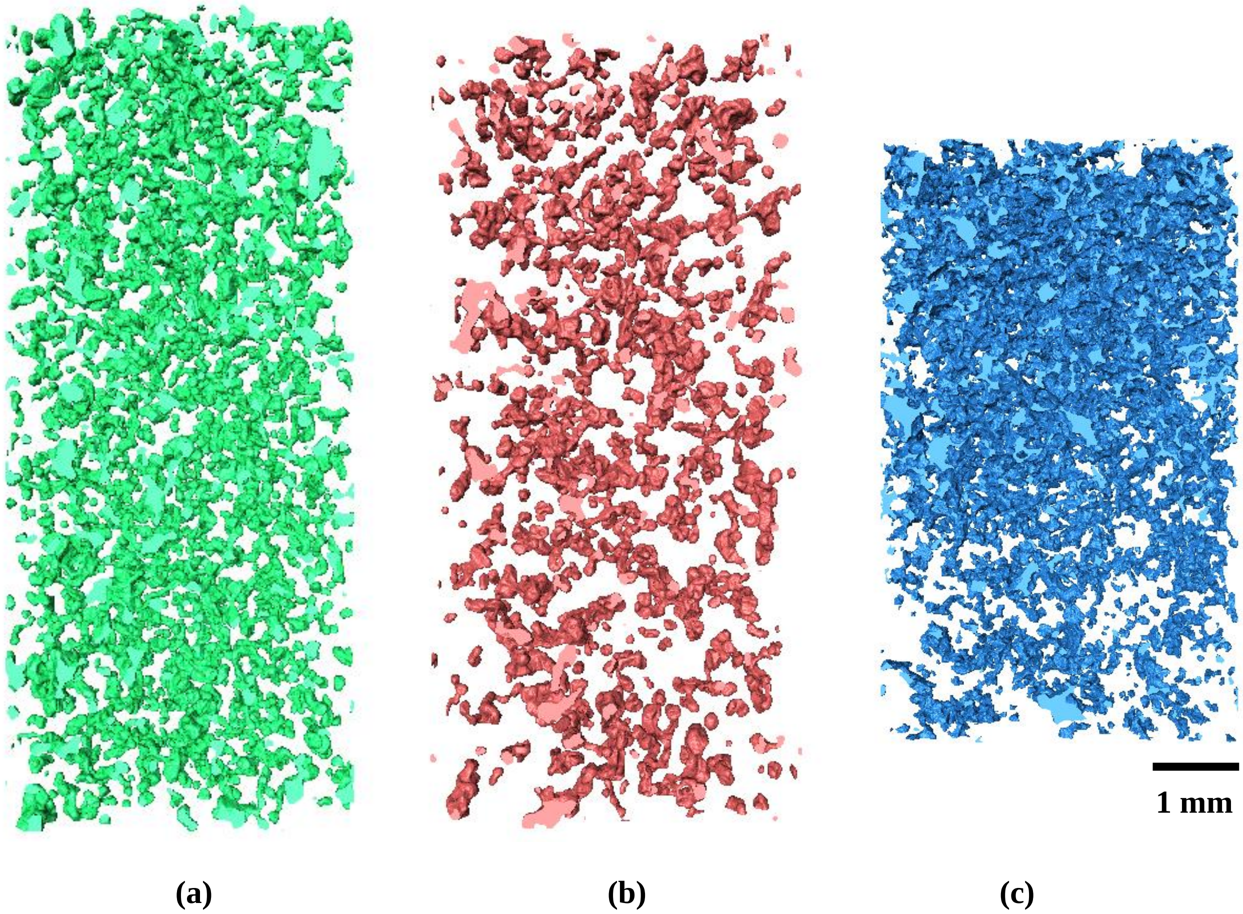

Figure 5-10. Isosurfaces of residual air clusters in Bentheimer sandstone cores at the end of imbibition for (a) a water-wet WW core (overall air saturation of 39%), (b) a weakly water-wet TMS core (27% overall air saturation), and (c) an intermediate-wet OTS core (overall air saturation of 44%).

Imbibition endpoint for the OTS experiment was reached based on visual confirmation of brine above the sample and P_c-S data, indicating that the observed vertical distribution of air was stable for the OTS system. No straightforward explanation was found for the elevated air saturation of the upper 3 mm of the OTS core. Evaporation of water from the top of the core during scanning is possible, despite measures taken to prevent evaporation in these experiments. In order to neglect these potential boundary condition effects, only data from the lower 3 mm of the OTS experiment is considered to be representative of trapping behavior in wettability altered systems.

Thus, considering only the lower 3 mm OTS data, the data indicates reduced trapping as contact angle increases (Figure 5-8); this is very similar to trends reported in oil recovery literature [Kennedy et al., 1955; Amott, 1959; Lorenz et al., 1974; Morrow, 1990], and to $scCO_2$-brine experiments conducted in water-wet and $scCO_2$-wet bead pack [Chaudhary et al., 2013].

The cluster size distributions of the residually trapped air phase are shown in Figure 5-11. Residual air phase clusters in the OTS sample occupy smaller pore spaces relative to those in the WW and TMS samples. Additionally, there is a higher frequency of small clusters in the lower 3 mm of the OTS core compared to the upper 3 mm of the same core, despite a much higher air saturation in the upper section; this is due to the presence of one large cluster which comprises most of the air volume (approx. 5 mm^3, not shown in Figure 5-11) in the upper 3 mm of the OTS core. This distribution of cluster sizes as a function of wettability state is supported by the imaging studies of Iglauer et al. [2012] who reported that there are more small clusters of residual oil under oil-wet vs. water-wet conditions.

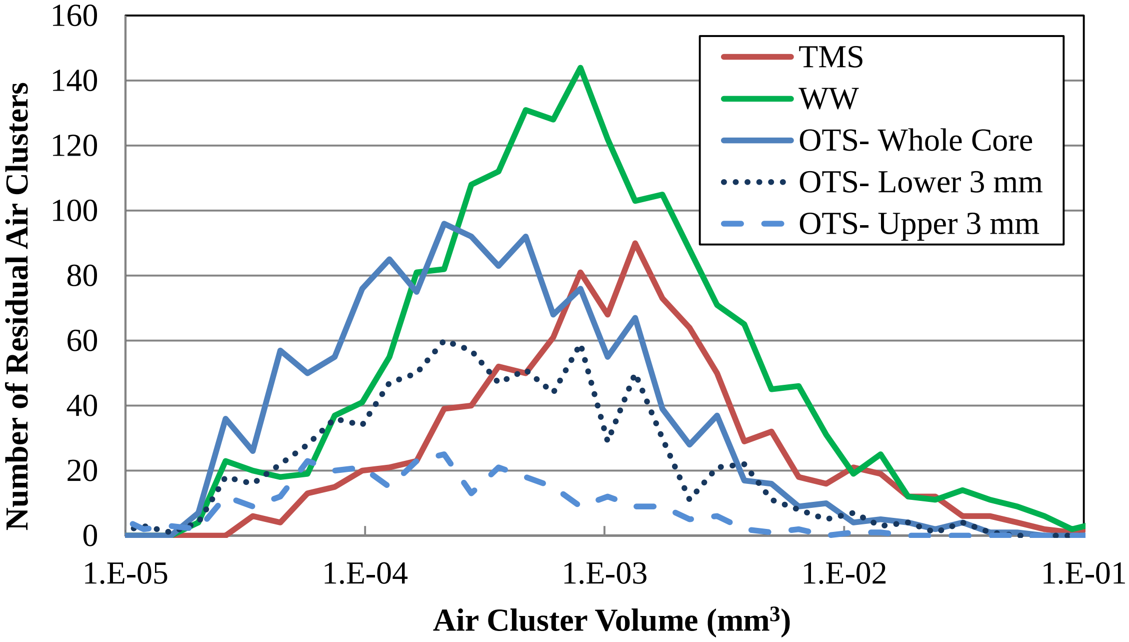

Figure 5-11. Representative histograms of frequency of residual air clusters present for a given cluster volume in a water-wet (WW) Bentheimer sandstone core, weakly water-wet (TMS) core, and three sections of an intermediate-wet (OTS) core. The OTS data is displayed as whole core, Lower 3 mm, and Upper 3 mm, depending on which vertical section of the core was analyzed.

5.5 Conclusions

We have qualitatively and quantitatively investigated the impact of wettability on drainage flow patterns and residual trapping of air (CO_2 proxy) in an air-brine-Bentheimer sandstone system, using cores of 4.9 mm diameter and 8.5-10.0 mm height. Capillary pressure-saturation curves, measured concurrently with x-ray CMT imaging studies, indicate that TMS vapor-phase treatment renders the (originally water-wet) sandstone cores to be weakly water-wet, while OTS liquid-phase treatment produces intermediate-wet cores.

Visual investigation of OTS and TMS cores (Figure 5-5) and vertical air distribution (Figure 5-6), along with quantitaive analysis of the air connectivity during drainage (Figure 5-3), imply that different wettability states produce distinctly different drainage flow regimes. Further, the flow regimes are distinct from those predicted by studies of water-wet systems of Lenormand et al. [1988] and Zhang et al. [2011], since these works neglect the role of gravity. We find that as contact angle increases, capillary effects decrease and buoyancy effects dominate flow patterns. Further work needs to be done in order to clearly delineate flow regimes in 3D, intermediate-wet systems.

Residual air saturation was highest in the upper imaged section of the intermediate-wet OTS core; however, this is likely due to enhanced boundary condition effects due to the increased contact angle; and is not expected to be representative of overall trapping behavior. We conclude that residual air saturation is highest in WW cores (average S_R and S_R/S_I values of 38%), followed by weakly water-wet TMS cores (average S_R of 29%, average S_R/S_I of 28%), with the lowest 3 mm region of intermediate-wet OTS cores demonstrating reduced trapping (average S_R of 23%, average S_R/S_I of 28%). Trapped air clusters in WW and TMS cores are present as larger clusters relative to the OTS trapped cluster distribution. These results are supported by the literature, as discussed previously.

For application to residual trapping of supercritical CO_2 in geologic sequestration operations, this study indicates that further research is needed in order to develop accurate models for the flow of CO_2 in media of different wettability; especially in flow regimes where buoyancy forces are important. Systems that exhibit a wettability change to higher contact angle due to exposure to supercritical CO_2 will likely demonstrate reduced residual trapping efficiency.

However, even under intermediate-wet conditions, significant trapping (e.g. S_R of 23% and S_R/S_I of approximately 28%) was still evident for our low capillary-number imbibition experiments.

5.6 Acknowledgements

This material is based upon work supported by the National Science Foundation under Grant No. IIA–1209476, as part of the East Asia and Pacific Summer Institute (EAPSI); as well as the U.S. Department of Energy, Basic Energy Sciences, Geosciences Program under award number DE-FG02-11ER16277. The EAPSI program is supported by the Australian Government and managed by the Australian Academy of Science. Adrian Sheppard is the recipient of an Australian Research Council Future Fellowship (project number FT100100470).

5.7 References

Akbarabadi, M., and M. Piri (2013), Relative permeability hysteresis and capillary trapping characteristics of supercritical CO_2/brine systems: An experimental study at reservoir conditions, Adv. Water Resour., 52, 190–206.

Amott, E. (1959), Observations Relating to the Wettability of Porous Rock.

Anderson, W. G. (1987a), Wettability Literature Survey- Part 4: Effects of Wettability on Capillary Pressure, J. Pet. Technol., 39(10), 1283–1300, doi:10.2118/15271-PA.

Anderson, W. G. (1987b), Wettability Literature Survey-Part 6: The Effects of Wettability on Waterflooding, J. Pet. Technol., 39(12), 1605–1622, doi:10.2118/16471-PA.

Andrew, M., B. Bijeljic, and M. J. Blunt (2014), Pore-scale contact angle measurements at reservoir conditions using X-ray microtomography, Adv. Water Resour., 68, 24–31, doi:10.1016/j.advwatres.2014.02.014.

Araujo, Y. C., P. G. Toledo, V. Leon, and H. Y. Gonzalez (1995), Wettability of Silane-Treated Glass Slides as Determined from X-Ray Photoelectron Spectroscopy, J. Colloid Interface Sci., 176(2), 485–490, doi:10.1006/jcis.1995.9942.

Berg, S., S. Oedai, and H. Ott (2013), Displacement and mass transfer between saturated and unsaturated CO_2–brine systems in sandstone, Int. J. Greenh. Gas Control, 12, 478–492, doi:10.1016/j.ijggc.2011.04.005.

Blunt, M. J. (1998), Physically-based network modeling of multiphase flow in intermediate-wet porous media, J. Pet. Sci. Eng., 20(3-4), 117–125, doi:10.1016/S0920-4105(98)00010-2.

Bradford, S. a., and F. J. Leij (1995), Fractional wettability effects on two-and three-fluid capillary pressure-saturation relations, J. Contam. Hydrol., 20(1-2), 89–109, doi:10.1016/0169-7722(95)00027-S.

Bradford, S. a., L. M. Abriola, and F. J. Leij (1997), Wettability effects on two- and three-fluid relative permeabilities, J. Contam. Hydrol., 28(1-2), 171–191, doi:10.1016/S0169-7722(97)00024-7.

Chalbaud, C., M. Robin, S. Bekri, and P. Egermann (2007), Wettability impact on CO_2 storage in aquifers: visualisation and quantification using micromodel tests, pore network model and reservoir simulations, in International symposium of the society of core analysts, Calgary, Canada.

Chaudhary, K., M. Bayani Cardenas, W. W. Wolfe, J. A. Maisano, R. A. Ketcham, and P. C. Bennett (2013), Pore-scale trapping of supercritical CO_2 and the role of grain wettability and shape, Geophys. Res. Lett., 40(15), 3878–3882.

Chiquet, P., D. Broseta, F. Complexes, U. Pau, and S. Thibeau (2005), SPE 94183 Capillary Alteration of Shaly Caprocks by Carbon Dioxide, , (1), 1–10.

El-Maghraby, R. M., and M. J. Blunt (2013), Residual CO_2 trapping in Indiana limestone., Environ. Sci. Technol., 47(1), 227–33, doi:10.1021/es304166u.

Herring, A. L., E. J. Harper, L. Andersson, A. Sheppard, B. K. Bay, and D. Wildenschild (2013), Effect of fluid topology on residual nonwetting phase trapping: Implications for geologic CO_2 sequestration, Adv. Water Resour., 62, 47–58, doi:10.1016/j.advwatres.2013.09.015.

Herring, A. L., L. Andersson, S. Schlüter, and D. Wildenschild (2014), Efficiently Engineering Pore-Scale Processes: Force Balance and Topology During Nonwetting Phase Trapping in Porous Media, submitted to Adv. Water Resour.

Iglauer, S., A. Paluszny, C. H. Pentland, and M. J. Blunt (2011), Residual CO_2 imaged with X-ray micro-tomography, Geophys. Res. Lett., 38(21), L21403.

Iglauer, S., M. A. Fernø, P. Shearing, and M. J. Blunt (2012), Comparison of residual oil cluster size distribution, morphology and saturation in oil-wet and water-wet sandstone., J. Colloid Interface Sci., 375(1), 187–92, doi:10.1016/j.jcis.2012.02.025.

IPCC (2005), IPCC special report on carbon dioxide capture and storage, edited by B. Metz, O. Davidson, H. de Coninck, M. Loos, and L. Meyer.

Jamaloei, B. Y., K. Asghari, and R. Kharrat (2012), The investigation of suitability of different capillary number definitions for flow behavior characterization of surfactant-based chemical flooding in heavy oil reservoirs, J. Pet. Sci. Eng., 90–91(0), 48–55, doi:10.1016/j.petrol.2012.04.020.

Kennedy, H. T., E. O. Burja, and R. S. Boykin (1955), An Investigation of the Effects of Wettability on Oil Recovery by Water flooding, J. Phys. Chem., 59(9), 867–869, doi:10.1021/j150531a015.

Kim, Y., J. Wan, T. J. Kneafsey, and T. K. Tokunaga (2012), Dewetting of Silica Surfaces upon Reactions with Supercritical CO_2 and Brine: Pore-Scale Studies in Micromodels, Environ. Sci. Technol., 46(7), 4228–4235, doi:10.1021/es204096w.

Krevor, S. C. M., R. Pini, L. Zuo, and S. M. Benson (2012), Relative permeability and trapping of CO_2 and water in sandstone rocks at reservoir conditions, Water Resour. Res., 48(2), W02532, doi:10.1029/2011wr010859.

Lenormand, R., E. Touboul, and C. Zarcone (1988), Numerical models and experiments on immiscible displacements in porous media, J. Fluid Mech., 189, 165–187, doi:doi:10.1017/S0022112088000953.

Liston, E. M. (1989), Plasma Treatment for Improved Bonding: A Review, J. Adhes., 30(1-4), 199–218, doi:10.1080/00218468908048206.

Lorenz, P. B., E. C. Donaldson, and R. D. Thomas (1974), Use of centrifugal measurements of wettability to predict oil recovery, Rep. Invest. - U.S., Bur. Mines; (United States), 7873.

Mahmud, W., and V. Nguyen (2006), Effects of Snap-Off in Imbibition in Porous Media with Different Spatial Correlations, Transp. Porous Media, 64(3), 279–300, doi:10.1007/s11242-005-4042-x.

Maloney, D. R., M. M. Honarpour, and A. D. Brinkmeyer (1990), The effects of rock characteristics on relative permeability.

McDougall, S. R., and K. S. Sorbie (1995), The Impact of Wettability on Waterflooding: Pore-Scale Simulation, SPE Reserv. Eng., 10(03), 208–213, doi:10.2118/25271-PA.

Morrow, N. R. (1990), Wettability and its effect on oil recovery, J. Pet. Technol., 24:12.

Pentland, C. H., R. El-Maghraby, A. Georgiadis, S. Iglauer, and M. J. Blunt (2011), Immiscible Displacements and Capillary Trapping in CO_2 Storage, Energy Procedia, 4, 4969–4976, doi:10.1016/j.egypro.2011.02.467.

Pini, R., and S. M. Benson (2013), Simultaneous determination of capillary pressure and relative permeability curves from core-flooding experiments with various fluid pairs, Water Resour. Res., 49(6), 3516–3530, doi:10.1002/wrcr.20274.

Plug, W. J., and J. Bruining (2007), Capillary pressure for the sand-CO_2-water system under various pressure conditions. Application to CO_2 sequestration, Adv. Water Resour., 30(11), 2339–2353, doi:10.1016/j.advwatres.2007.05.010.

Renard, P., and D. Allard (2013), Connectivity metrics for subsurface flow and transport, Adv. Water Resour., 51, 168–196.

Treiber, L. E., and W. W. Owens (1972), A Laboratory Evaluation of the Wettability of Fifty Oil-Producing Reservoirs, Soc. Pet. Eng. J., 12(06), 531–540, doi:10.2118/3526-PA.

Varslot, T., A. Kingston, G. Myers, and A. Sheppard (2011), High-resolution helical cone-beam micro-CT with theoretically-exact reconstruction from experimental data., Med. Phys., 38(10), 5459, doi:10.1118/1.3633900.

Wan, J., Y. Kim, and T. K. Tokunaga (2014), Contact angle measurement ambiguity in supercritical CO_2–water–mineral systems: Mica as an example, Int. J. Greenh. Gas Control, 31, 128–137, doi:10.1016/j.ijggc.2014.09.029.

Zhang, C., M. Oostrom, T. W. Wietsma, J. W. Grate, and M. G. Warner (2011), Influence of Viscous and Capillary Forces on Immiscible Fluid Displacement: Pore-Scale Experimental Study in a Water-Wet Micromodel Demonstrating Viscous and Capillary Fingering, Energy & Fuels, 25(8), 3493–3505, doi:10.1021/ef101732k.

Chapter 6. Pore-scale observations of supercritical CO_2 drainage in Bentheimer sandstone by synchrotron x-ray imaging

Anna L. Herring[1], Linnéa Andersson[1], D.L. Newell[2], J.W. Carey[3], and Dorthe Wildenschild[1]

[1]*School of Chemical, Biological and Environmental Engineering, Oregon State University, Corvallis, OR, USA*
[2]*Utah State University, Department of Geology, Logan, UT, USA*
[3] *Earth and Environmental Sciences Division (EES), Los Alamos National Laboratory, Los Alamos, NM, USA*

International Journal of Greenhouse Gas Control
IEA Greenhouse Gas R&D Programme, Cheltenham, UK
Published: Volume 25, June 2014
ISSN 1750-5836
http://dx.doi.org/10.1016/j.ijggc.2014.04.003

6.1 Abstract

This work utilizes synchrotron-based x-ray computed microtomography (x-ray CMT) imaging to quantify the volume and topology of supercritical carbon dioxide ($scCO_2$) on a pore-scale basis throughout the primary drainage process of a 6 mm diameter Bentheimer sandstone core. Experiments were performed with brine and $scCO_2$ at 8.3 MPa (1200 PSI) and 37.5^oC. Capillary pressure-saturation curves for the $scCO_2$-brine system are presented and compared to the ambient air-brine system, and are shown to overlay one another when pressure is normalized by interfacial tension. Results are analyzed from images with a voxel resolution of 4.65 µm; image-based evidence demonstrates that $scCO_2$ invades the pore space in a capillary fingering regime at a mobility ratio M=0.03 and capillary number $Ca=10^{-8.6}$ to an end-of-drainage brine saturation of 9%. We provide evidence of the applicability of previous two-dimensional micromodel studies and ambient condition experiments in predicting flow regimes occurring during $scCO_2$ injection.

6.2 Introduction

Geologic carbon sequestration has been proposed as a potential climate change mitigation strategy to prevent emissions of CO_2 to the atmosphere from large fossil-fuel burning point sources [IPCC, 2005]. In geologic sequestration, supercritical CO_2 ($scCO_2$) is injected into saline groundwater hosted in a porous aquifer (i.e. a brine drainage process), thus producing an immiscible displacement scenario where $scCO_2$ is the non-wetting (NW) fluid and brine is the wetting (W) fluid. Subsequently $scCO_2$ is mobilized or trapped by capillary forces when brine reenters the pore space of the geologic matrix (i.e. the brine imbibition process) during water flooding or buoyant CO_2 migration. There are concerns associated with the long-term stability of a mobile subsurface CO_2 plume, so drainage and imbibition should be carefully engineered to facilitate favorable trapping conditions. Capillary trapping of $scCO_2$, wherein the CO_2 is held within the pore structure of the geologic matrix by capillary forces, is a safer form of subsurface storage than hydrodynamic or structural trapping, which relies on a low permeability caprock to contain the buoyant CO_2 plume; additionally, capillary trapping occurs on vastly shorter timescales than reactive trapping methods (i.e. dissolution trapping and mineral trapping) [IPCC, 2005; Qi et al., 2009]. To understand the multiphase physics of CO_2 transport and to make quantitative estimations of potential CO_2 capillary trapping in saline aquifers, it is necessary to study field, core, and pore-scale processes. Experiments at geological reservoir conditions at the core and pore-scale in combination with x-ray computed microtomography (x-ray CMT) allow for three-dimensional (3D) in-situ visualization of fluid phases and the physical structure within a porous medium [Blunt et al., 2013; Ketcham and Carlson, 2001; Wildenschild et al., 2002] and have the potential to provide insight into the engineered process of geologic CO_2 sequestration to achieve high volume trapping of CO_2. An overview of recent advances in pore-scale characterization of structure and flow processes via x-ray CMT technology can be found in Wildenschild and Sheppard [2013].

A number of studies have indicated that capillary trapping of $scCO_2$ may be maximized via manipulation of the temperature, pressure, salinity, and flow rates of the CO_2 and brine injections such that the CO_2-brine interactions are most conducive to capillary trapping [Bachu and Bennion, 2008b; Wildenschild et al., 2011]. Studies of general flow regimes in simple model systems, such as glass beads [Morrow et al., 1988; Polak et al., 2011] and two-dimensional (2D) micromodels [Lenormand et al., 1988; Wang et al., 2012; Zhang et al., 2011], have demonstrated the transitions between capillary, viscous, and gravity force-dominated regimes and the resulting effects on drainage flow patterns and capillary trapping. Although these works undoubtedly provide insight to the general field of transport in porous media, they may not all be analogous to a $scCO_2$-brine sequestration scenario because (a) some are not conducted at reservoir conditions, (b) results from simple model systems do not directly translate to geologic media, (c) the wettability condition of the $scCO_2$-brine-rock system is not the same as in analogue systems, and (d) only the drainage (CO_2 injection) process has been analyzed so far. Confirmation of the applicability of the results of these analogue model systems to a $scCO_2$ sequestration scenario is needed.

Recent bulk-measurement-focused experiments (i.e. experiments wherein experimental parameters are measured at the inlet and outlet of the core, but not at individual points within the core) with $scCO_2$ at reservoir conditions have expanded knowledge of $scCO_2$ flow in porous media. Pentland et al. [2011a] measured the relationship between initial and residual (i.e. capillary trapped) $scCO_2$ saturation in Berea sandstone and found that the capillary-trapped amount of $scCO_2$ was less, although still significant, than that of an ambient condition analogue (decane) in the same medium, with residual $scCO_2$ saturations occupying up to 35% of the pore space. Bachu and Bennion [2008b] demonstrated that pressure, temperature, and salinity conditions, as well as rock characteristics, have a significant impact on flow parameters such as capillary pressure, relative permeability, and interfacial tension (IFT) of $scCO_2$-brine systems. Others have investigated the wettability state of various $scCO_2$-brine-medium systems, e.g. in sand packs [Plug and Bruining, 2007], sandstone [Pentland et al., 2011b], and carbonates [El-Maghraby and Blunt, 2012], and have shown that under primary drainage conditions the media behaves as strongly water-wet systems; however, during imbibition, sand and sandstone may transition to a more weakly water-wet or intermediate-wet system as a result of exposure to $scCO_2$. Other studies have shown that the CO_2-brine system can display a range of contact angles depending on the pressure, temperature, and composition of the solid surface [Broseta et al., 2012; Chalbaud et al., 2009].

In addition to these bulk-measurement-focused experiments, x-ray CMT has been utilized from a pore-scale perspective to establish the feasibility of high-resolution visualization of reservoir pressure CO_2 [Silin et al., 2011]; to confirm that residual trapping of $scCO_2$ is achievable in geologic media [Iglauer et al., 2011]; and to investigate the influence of media properties such as geometry of natural and synthetic media [Pentland et al., 2012] and wettability and grain shape of synthetic media [Chaudhary et al., 2013] on $scCO_2$ flow. In addition, core-scale studies have investigated relative permeability [Akbarabadi and Piri, 2013; Perrin et al., 2009], pressure-saturation curves [Pini et al., 2012], as well as the relationship between initial and residual $scCO_2$ saturations [Akbarabadi and Piri, 2013].

In this work, we present a synchrotron tomography-based pore-scale analysis of the drainage processes of the $scCO_2$-brine system in Bentheimer sandstone with an in-house developed mobile high-pressure setup for operation at geological reservoir conditions using a core holder compatible with x-ray CMT. We present and compare the ambient (air-brine) and supercritical ($scCO_2$-brine) capillary pressure-saturation curves for primary drainage in Bentheimer sandstone; we show images of the $scCO_2$ within the Bentheimer sandstone at multiple points during the $scCO_2$ injection (drainage) process; and we analyze the evolution of connectivity of $scCO_2$ fluid clusters. The results indicate that ambient pressure or micromodel system experiments can accurately predict the dominant flow regime during $scCO_2$ drainage in Bentheimer sandstone and confirm that low mobility ratio (M) and low capillary number (Ca) flow during drainage results in capillary fingering displacement of the wetting fluid.

6.3 Experimental Equipment and Methods

6.3.1 Porous Medium and Fluid Characteristics

Two 6 mm diameter Bentheimer sandstone cores, denoted B1 (length of 37.1 mm) and B2 (length of 39.6 mm), were used during supercritical drainage experiments. Drainage of core B1 was stopped at seven points during drainage to allow for equilibration and scanning ("quasi-static"), while core B2 was drained continuously, but not scanned, allowing for comparison of the quasi-static scanned and continuous unscanned capillary pressure-saturation curves. A third core, B3, was drained continuously under ambient conditions with air as the nonwetting phase following the methods of Herring et al. [2013]. Porosity of B1, derived from a dry scan of the core with voxel resolution of 4.65 µm, was 16%. The petrophysical properties of Bentheimer sandstone have been previously reported by Maloney et al. [1990] and Øren et al. [1998]. The wetting (W) fluid was a brine of 1:6 by mass potassium iodide (which produces good x-ray contrast) and deionized water. Relevant fluid properties at supercritical experimental conditions ($T= 37.5^oC$, $P=8.3$ MPa) are shown in Table 6-1.

Table 6-1. Experimental fluid properties at $T= 37.5^oC$, $P=8.3$ MPa.

	Viscosity (mPa-s)	Density (kg/m^3)	IFT w. Brine (mN/m)
$scCO_2$	0.03[a]	360[a]	approx. 38[b]
Brine	1.13	1080	-

a. National Institute of Standards and Technology (NIST) web database [http://webbook.nist.gov/chemistry/]
b. Interpolated from data by Bachu and Bennion [2008a]

6.3.2 Supercritical Experimental Set Up

The mobile experimental set up (Figure 6-1) was designed to allow for both core-scale and pore-scale flow experiments at pressures up to 13.75 MPa (2000 PSI) in combination with synchrotron and bench top x-ray imaging. All components are connected via 3.18 mm (1/8")

O.D. 316 stainless steel tubing (Swagelok, Solon OH, United States) and are mounted upon heavy-duty rolling carts. The aluminum Hassler-sleeve type core holder (Phoenix Instruments, Splendora Texas, United States) has a wall thickness of 0.127 cm and can accommodate cores up to 6.35 mm in diameter and 7.6 cm in length (Figure 6-2). Overburden pressure was applied to the core via a Buna-N Nitrile sleeve accommodated inside the core holder. The core was assembled with a stainless steel spacer, Viton o-ring, and two layers of hydrophilic nylon membrane with 1.2 micron pore size (General Electric Company, Fairfield CT, United States) at the base of the core and a Viton o-ring and a 316 stainless steel washer at the top of the core. The entire core assembly is wrapped in aluminum foil to prevent uptake of the $scCO_2$ by the Buna-N nitrile overburden sleeve, and then wrapped in Teflon tape (Figure 6-2). Core temperature is maintained via incandescent lamps and continuously monitored with external thermocouples (Omega Engineering Inc, Stamford Connecticut, United States).

Fluid flow rates and pressures, including the overburden pressure, were controlled by high precision, high pressure syringe pumps (Teledyne ISCO, Lincoln NE, United States). The 400 ml fluid separator (Figure 6-1) (manufactured in-house) allows complete mixing of the fluids and is monitored by a differential pressure transducer with a range of ±14.0 kPa (± 2 PSI) (Validyne Engineering, Northridge CA, United States). Three other Validyne pressure transducers are connected in parallel with the core holder to allow pressure measurements during flow experiments: two pressure transducers measure absolute pressure above and below the core (pressure range: ±8.6 MPa (±1250 PSI)), and one pressure transducer measures differential (i.e. capillary) pressure across the core (pressure range: ±14.0 kPa). The 450 ml brine and CO_2 accumulators and fluid separator, the temperature sensitive pressure transducers, as well as all other temperature-sensitive components of the setup are housed in a temperature-controlled and monitored environment (oven and external compartment), as indicated in Figure 6-1.

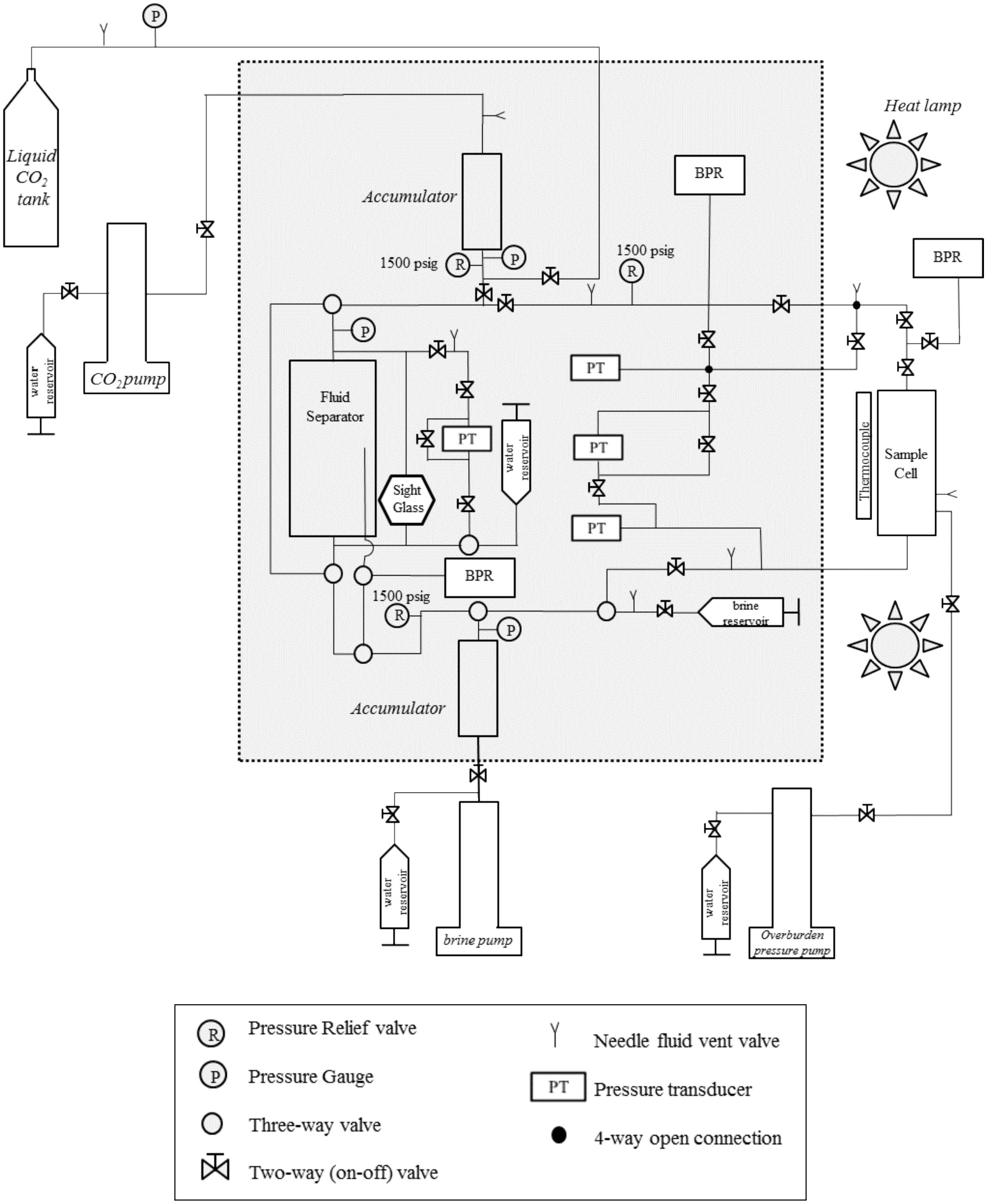

Light gray box indicates component is inside temperature-controlled environment

Figure 6-1. Experimental schematic.

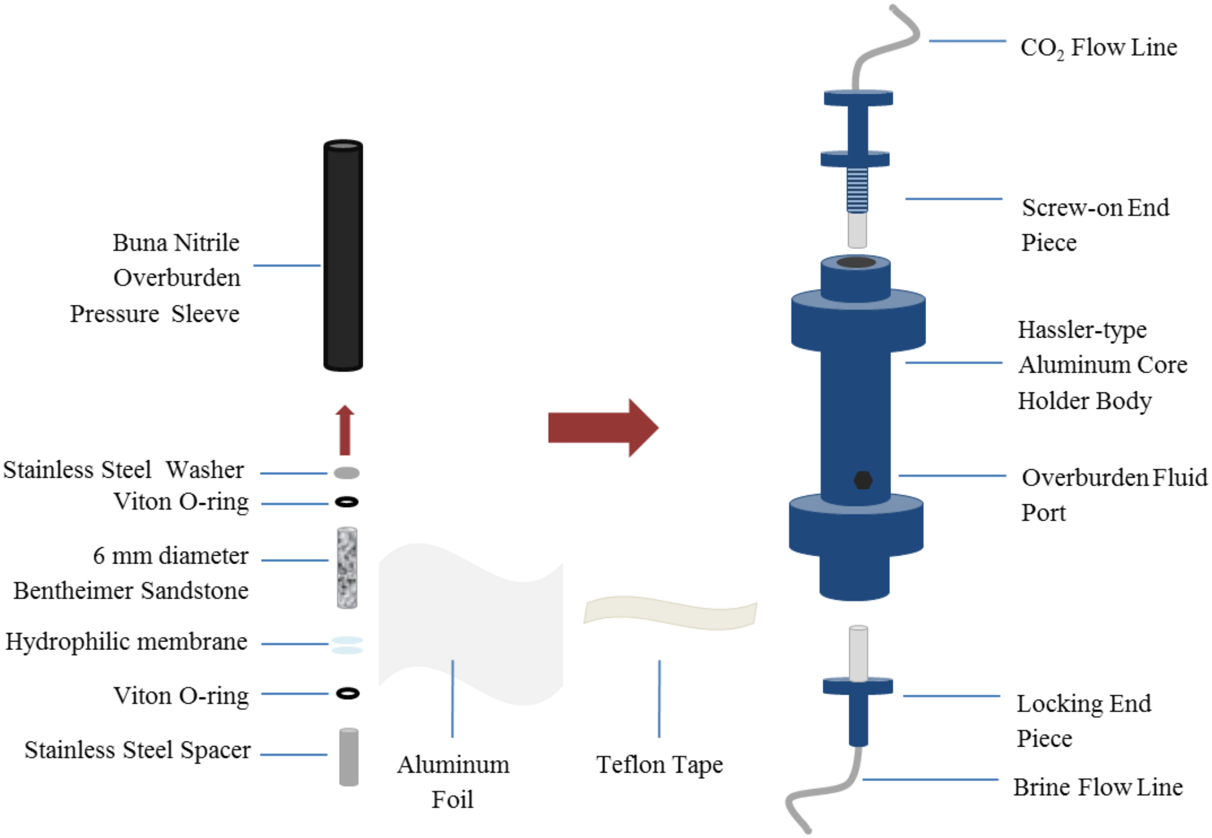

Figure 6-2. Assembly of high-pressure core holder for Bentheimer sandstone drainage experiment.

6.3.3 Supercritical Experimental Process

Before filling and pressurizing the high-pressure system, the CO_2 flow paths and fluid separator components assigned to hold and transport CO_2 were cleared of air by repeatedly flushing with gaseous CO_2. The brine accumulator and the connections for brine were filled with degassed brine and taken up to working pressure (8.3 MPa or 1200 PSI). Approximately 150 ml of brine at ambient pressure was pumped into the separator; then CO_2 was pumped into the separator until working pressure was achieved.

Mixing of fluids occurs within the fluid separator which has ports that are flush with the endcaps at the top and bottom of the vessel as well as a bored-thorough port at the bottom with a line that reaches approximately the midpoint of the vessel. Fluids are pushed back and forth using the high pressure pumps: $scCO_2$ is pushed through the flush bottom port while a mixture of fluids is allowed to be retracted through the midpoint line, then the mixture of fluids is pushed back into the cylinder via the midpoint line while the $scCO_2$ phase is allowed to retract from the top flush port. Pushing in the buoyant $scCO_2$ through the bottom port allows the $scCO_2$ to travel through the brine phase as it migrates to the top of the separator vessel, and pushing the mixture of fluids through the midpoint line allows brine in the mixture to cascade down through the $scCO_2$ phase, facilitating complete mixing. This mixture process was performed at least three cycles. Finally, brine phase was pulled from the bottom flush port then pushed through the midpoint line multiple times, while $scCO_2$ was allowed to flow in or out of the cylinder via the top port. This step clears the midpoint and lower brine lines of $scCO_2$, replacing it with a pure phase of CO_2-saturated brine.

Temperatures were set to 37.5^{o}C, and fluids allowed to reach chemical and thermal equilibrium, a process requiring 12-16 hours. Temperature was continuously monitored by thermocouples inside the temperature-controlled space. Equilibrium was assumed to be reached when the CO_2 pump, set to maintain constant pressure, maintained a constant volume, indicating no further fluid volume changes, and the pressure across the separator maintained a constant value.

The core assembly was attached to the system and vacuum-degassed brine was used to wet the hydrophilic membrane and flush the core, with an applied overburden pressure of 1.4 MPa (200 PSI). Vacuum was applied at the upper outlet of the core holder in order to completely saturate the core with brine. The core was gradually brought to the working pressure (8.3 MPa), while the overburden pressure was concurrently raised to approximately 4.1 MPa (600 PSI) in excess of the core pressure, and the core temperature (37.5^{o}C) was established using incandescent lamps. Once the core reached a stable temperature, the core was flushed with CO_2-saturated brine at 8.3 MPa and 37.5°C until CO_2 gas was confirmed to exit at the core holder back-pressure regulator (BPR) (see Figure 6-1). This filling process ensured that the brine within the core was saturated with CO_2 and that the drainage process was truly immiscible (i.e. the $scCO_2$ displaced the brine rather than dissolving into it). At this point, $scCO_2$ was introduced into the line above the core holder and the CO_2 and brine phases were separated by a single valve (labeled “S1” in Figure 6-1), and the core system was allowed to equilibrate. Equilibration was established when the differential pressure transducer across the core maintained a constant pressure.

The brine pump was used to control flow rate from the bottom of the core; while the CO_2 pump provides a constant pressure boundary at the top of the core. The brine pump was set to retract at a constant volumetric flow rate of 0.100 ml/hr, while the $scCO_2$ pump was set to a constant pressure setting of 8.3 MPa (1200 PSI). Absolute and differential pressures were continuously monitored and recorded. For both continuous and quasi-static (scanned) experiments, pumping of brine continued until a differential pressure of approximately 14.0 kPa (the pressure transducer range) was achieved, indicating that the NW fluid had reached the hydrophilic membrane. For scanning, the pumps were stopped at seven points during the drainage process, the system was allowed to equilibrate for 45 minutes and a scan was acquired of the core. A scan was also taken of the dry core.

For the scanned experiment, $scCO_2$ saturation was derived from the images. Nonwetting phase saturation for the unscanned, continuous curves was calculated from the pore volume of the rock (which is estimated using the dimensions and mass of the vacuum dried core) and the brine flow rate. That start point of drainage within the core (rather than the line above the core) is evident as a sharp decrease in pressure and saturation is calculated as a function of time from that start point.

6.3.4 Synchrotron x-ray CMT Imaging and Data Processing

Tomographic imaging was performed at the bending magnet beam-line at sector 13 (GSECARS) at the Advanced Photon Source at Argonne National Laboratory. The beam-line specifications have been described in detail in previous works [Rivers et al., 1999; Wildenschild et al., 2005; Wildenschild et al., 2002]. All scans were performed at a monochromatic energy level of 37.0 keV, significantly above the K-shell photoelectric absorption edge of iodine (33.17 keV), resulting in high x-ray attenuation by the 1:6 by weight potassium iodide-doped brine and thus allowing for separation of the wetting and non-wetting fluids in the reconstructed images. This higher energy was used to overcome the attenuation due to the core holder, overburden pressure fluid, and aluminum foil surrounding the core. Images were captured at 720 angles, with a horizontal field of view of 6.47 mm, a vertical field of view of 4.83 mm, and a resulting voxel resolution of 4.65 µm, as a result of utilizing local tomography. For each point on the drainage curve (subsequently labeled A to G, e.g. in Figure 6-5), two scans were acquired at different heights in the core with a vertical overlap of 0.5 mm.

The acquired radiographs were reconstructed into three-dimensional (3D) volumes via the programming language IDLTM (Research Systems Inc.) and the subsequent image processing and analysis was performed using Avizo® Fire (FEI Visualization Sciences Group, Burlington Massachusetts, United States).

To reduce noise and blur, the grayscale 3D datasets (Figure 6-3a) were processed with an anisotropic diffusion filter applied with a diffusion threshold value of 350 and 50 iterations (Figure 3b). The anisotropic diffusion filter facilitates the histogram-based segmentation process by separating the peaks that differentiate two phases: the non-wetting phase $scCO_2$ and a combination of the wetting phase and solid (Figure 6-3a and b). We segmented the resulting grayscale image by applying a universal intensity threshold to all volumes at a grayscale value of 62.5 (Figure 6-3c). To remove the remaining noise, we applied a size exclusion filter that removes all NW phase-labeled clusters smaller than 250 voxels (Figure 3d). The size of these clusters corresponds to the volume of a spherical pore with a radius of 18.2 µm; removal of clusters smaller than this size is justified given the pore-size distribution of the Bentheimer sandstone [Maloney et al., 1990]. The two vertical scan sections were then merged to form an 8.0 mm tall volume, and all quantitative measures are calculated on this final volume using analysis tools available in Avizo® Fire: total number and density of NW-labeled voxels and individual volume of distinct NW voxel clusters. These values were normalized by the corresponding values for the respective core in its dry state.

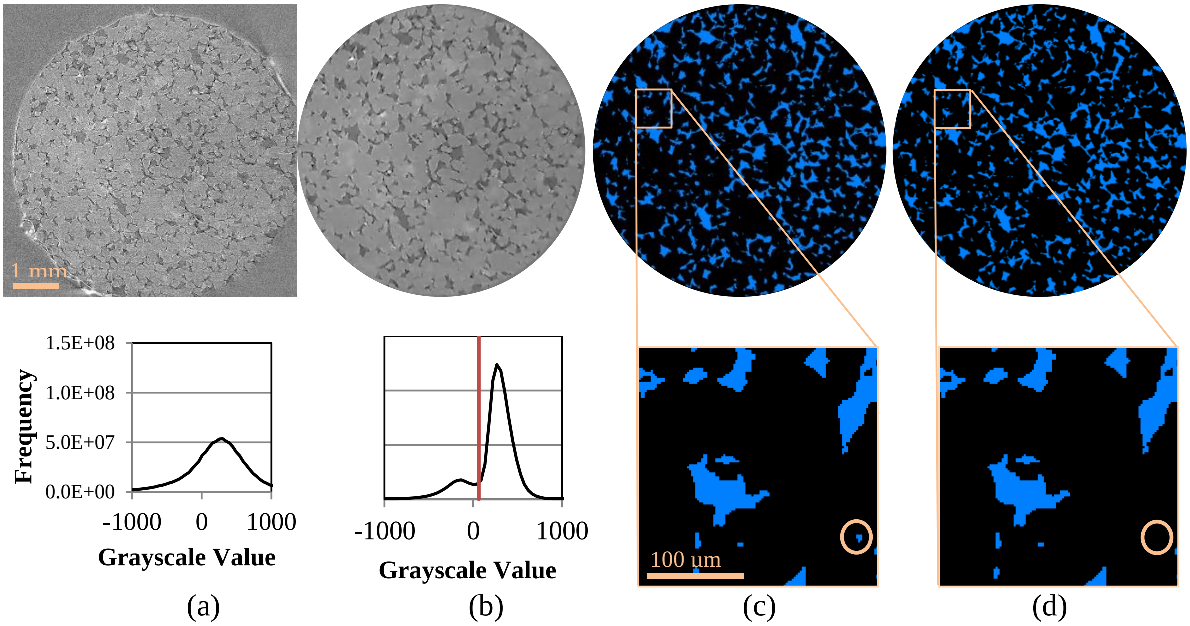

Figure 6-3. Image processing steps for segmenting supercritical CO_2 ($scCO_2$) within Bentheimer sandstone. The raw data (a) is cropped and an anisotropic diffusion filter is applied (b). The filtered image is segmented according to the grayscale histogram local minimum, resulting in a binary image (c) and noise is removed applying a size exclusion filter (d).

6.4 Results and Discussion

6.4.1 Primary Drainage Pressure-Saturation Relationship

The drainage process of the $scCO_2$-brine system in Bentheimer sandstone, at geological reservoir conditions, was imaged at the pore-scale using x-ray synchrotron tomography. Capillary pressure- saturation (P_c-S) curves measured with the supercritical experimental system are shown in Figure 6-4a; a continuous drainage curve (from core B2) is overlain with the equilibrium pressure-saturation points from the scanned drainage experiment (core B1) showing consistent behavior between the stepped equilibrium data and the continuously scanned measurements. The scanned points from core B1 are labeled A-G, corresponding to the data presented in Section 3.2. Note that the pressures of points B and C are estimated by comparison to the continuous drainage curve, due to inadequate equilibration during the first two scanning periods. Point A was collected prior to the start of drainage. However, temperature fluctuations within the core (temperature ranged from 36.9 to 38.8^{o}C prior to the start of data collection) caused exsolution of dissolved CO_2 and the resulting data is shifted towards lower brine saturation (i.e. less than 1.0) (e.g. Figure 6-4, point A; and Figure 6-7a).

For comparison with the $scCO_2$-brine system, an ambient air-brine P_c-S curve was measured on a third core, B3, following the methods described in Herring, et al. [2013] and is also shown in Figure 6-4a. The decrease in NW phase entry pressure between the ambient air and supercritical CO_2 curves is due to decreased interfacial tension (IFT) between $scCO_2$ and brine as compared to air and brine (see Table 6-1). This result is similar to the shift between supercritical and ambient pressure-saturation curves reported by Plug and Bruining [2007] and Akbarabadi and Piri [2013]. This interpretation is confirmed by the curves shown in Figure 6-4b, wherein the capillary pressures of the systems are normalized by their respective interfacial tension values; as shown, primary drainage for the $scCO_2$-brine and air-brine systems can be successfully described by a single P_c/σ-S relationship. This finding provides support for use of analogue fluids in flow experiments to simulate primary drainage of $scCO_2$.

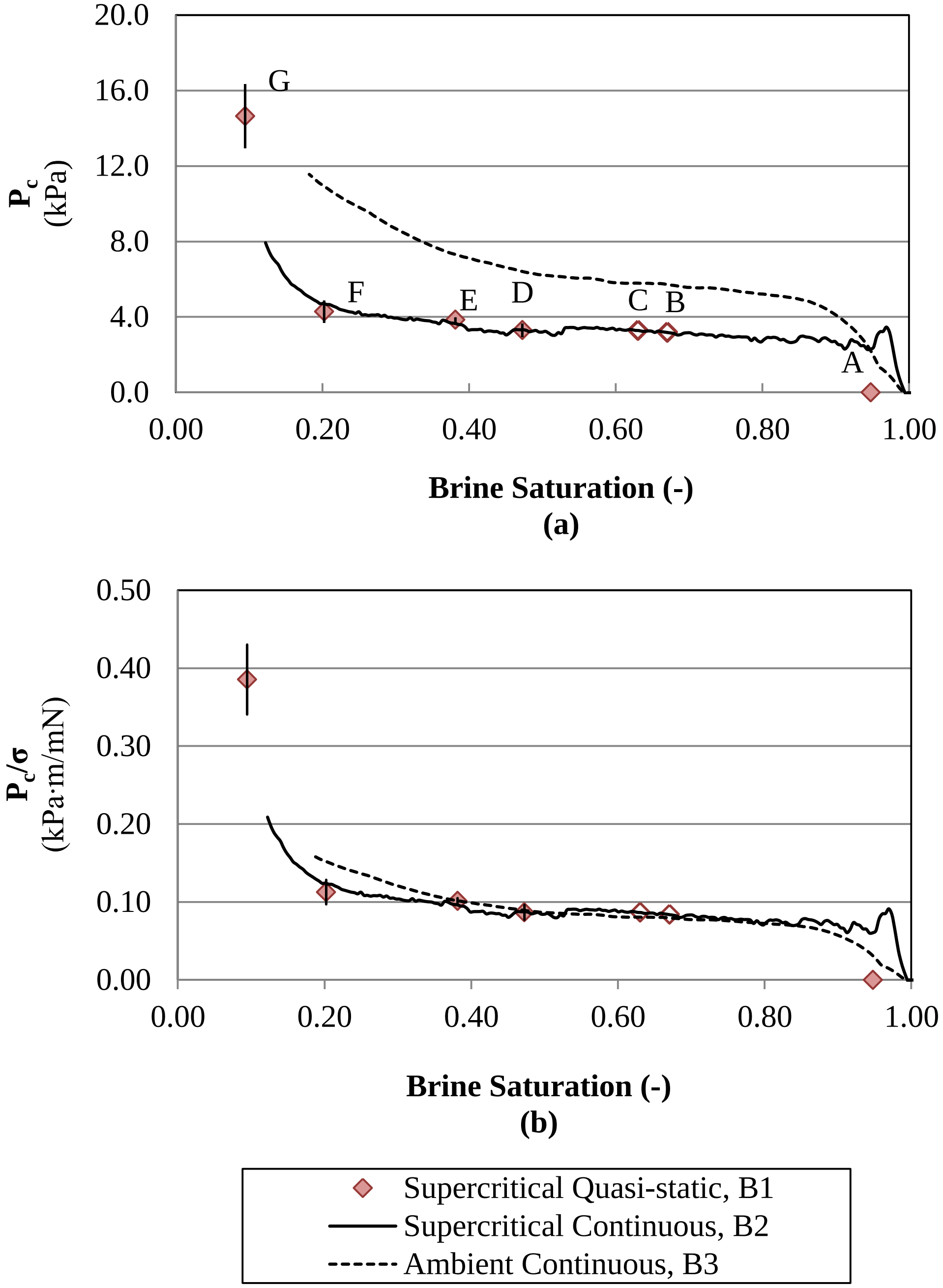

Figure 6-4. Primary drainage (a) capillary pressure-saturation (P_c-S) curves and (b) capillary pressure normalized by interfacial tension-saturation (P_c/σ-S) curves for the two $scCO_2$-brine experiments (continuous and quasi-static) and for a continuous ambient air-brine drainage experiment. The quasi-static points are labeled with their scan designation in (a). Uncertainty bars indicate the range of pressure variation during equilibration. The hollow supercritical quasi-static points indicate estimated pressure values.

The brine saturation at the end of primary drainage (“initial” brine saturation) measured here (scan G, Sw = 9%) is relatively low compared with other $scCO_2$ flow experiments. For example, Iglauer et al. [2011] measured an initial brine saturation of approximately 50% in homogenous Doddington sandstone cores of 9 mm length and 4.95 mm diameter, and Akbarabadi and Piri [2013] measured initial brine saturations ranging from 30% to 75% in Berea and Nugget sandstone cores of approximately 15 cm length and 3.8 cm diameter. Similarly, Krevor et al. [2012] report initial brine saturations of 41% to 54% in a variety of 5 cm diameter, 10 cm length sandstone and reservoir rock samples; however, Krevor et al. state that the minimum achievable end-of-drainage brine saturation is dependent on the capillary pressure achieved in the experiment, and the authors indicate that lower brine saturations should be attainable at sufficiently high capillary pressure. The difference in initial bine saturation values between these previous studies and the value reported here is due to our use of a hydrophilic membrane at one end of the core (the works mentioned above use co-current flow, and do not include a membrane in the experimental design). A similar effect is shown by Pentland et al. [2011a] who achieved initial brine saturations of approximately 10% with the use of a semi-permeable disk in their experimental set-up. The hydrophilic membrane (or semi-permeable disk) prevents $scCO_2$ breakthrough, thus approximating a semi-infinite geologic media, and allows higher capillary pressures (and consequently, lower brine saturations) to be achieved. As a result of this experimental design, we have presented a more complete pressure-saturation curve for primary drainage, derived from real-time measurements of capillary pressure across the core coupled with x-ray tomography based saturation information.

6.4.2 Connectivity and Topology of $scCO_2$ Front during Drainage

The connectivity of NW fluid after drainage plays a significant role in controlling the amount of residual trapping of the NW fluid that is achieved after the subsequent imbibition of W fluid back into the pore space [Herring et al., 2013; Wardlaw and Yu, 1988]. Here, the connectivity of the CO_2 is investigated via Γ_{scCO2} [Renard and Allard, 2013]:

$$\Gamma_{scCO_2} = \frac{1}{n_{scCO2}^2} \sum_{i=1}^{N(X_{scCO2})} n_i^2 \qquad \text{(Eq. 6.1)}$$

where n_i is the number of connected $scCO_2$ voxels of each individual i^{th} $scCO_2$ cluster (i.e. the size of each individual $scCO_2$ cluster, in voxels), X_{scCO2} is the set of all $scCO_2$ voxels, and n_{scCO_2} is the total number of $scCO_2$ voxels. The relative fraction of connected $scCO_2$ clusters increases as drainage proceeds and brine saturation decreases (Figure 6-5). The relative fraction of connected $scCO_2$ clusters approaches unity even at relatively high brine saturation (0.60); this indicates that the $scCO_2$ invades the core largely as one connected component, rather than multiple distinct fingers emanating from distinct sources.

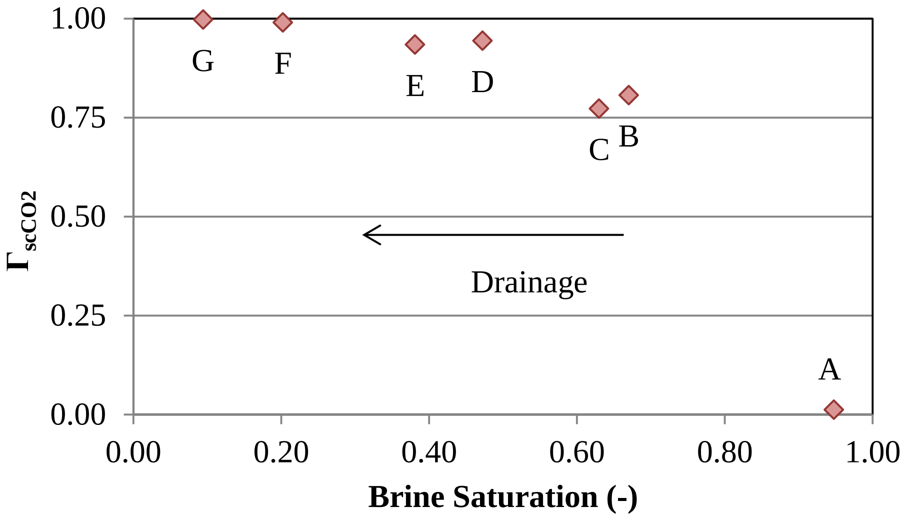

Figure 6-5. Connectivity of the supercritical CO_2 ($scCO_2$), quantified by the connectivity measure $\Gamma_{scCO2,}$ as a function of brine saturation during the brine drainage process in Bentheimer sandstone

The high connectivity of the $scCO_2$ is confirmed by investigating the distribution of the $scCO_2$ cluster sizes (Figure 6-6). Figure 6-6a demonstrates that throughout the drainage process, the number of small clusters (clusters of approximately 0.01 mm^3 and smaller) first increases (points A to E), then decreases (points E to G). These small clusters are present due to snap-off, which occurs when pumping is paused during scanning. The number of small clusters first increases as more $scCO_2$ enters the pore space, then decreases as pumping continues and $scCO_2$ saturation increases and connects individual clusters via pore throats. Figure 6-6b is a truncated plot, showing the size distribution of the medium (0.01 – 1 mm^3) and large (> 1 mm^3) clusters, which establishes that for drainage points B-G, there exists precisely one large cluster that increases in volume from points B-G. Comparison of Figure 6-6b with Figure 6-6c establishes that this one large $scCO_2$ cluster makes up the great majority of the total $scCO_2$ volume within the pore space (90% of the total $scCO_2$ volume for point B, and increasing as drainage proceeds) for every drainage point (excluding point A, which was measured before the start of drainage).

The topology of the $scCO_2$ can be investigated from a qualitative perspective as well (Figure 6-7). Three dimensional (3D) isosurfaces and two dimensional (2D) binary X-Z oriented slices of the $scCO_2$ show the extent of temperature-induced $scCO_2$ phase separation out of the brine prior to drainage (Figure 6-7, scan designation A). We note here that such exsolution may occur in any experiment using CO_2-saturated brine, which highlights the importance of maintaining temperature uniformity throughout the experimental system. The tomographic data show the increase of $scCO_2$ saturation during the progression of drainage (Figure 6-7, scan designations B, D, and G). A subsection of these binary X-Z oriented slices overlain on the original grayscale data (Figure 6-7) demonstrates the evolution of the $scCO_2$ front on the pore scale. As shown by all three image types, although $scCO_2$ was injected at the top of the core, the $scCO_2$ does not move in a uniform, stable front. Rather, it first invades the largest pores, gradually filling smaller pores as drainage proceeds, and travelling in all directions.

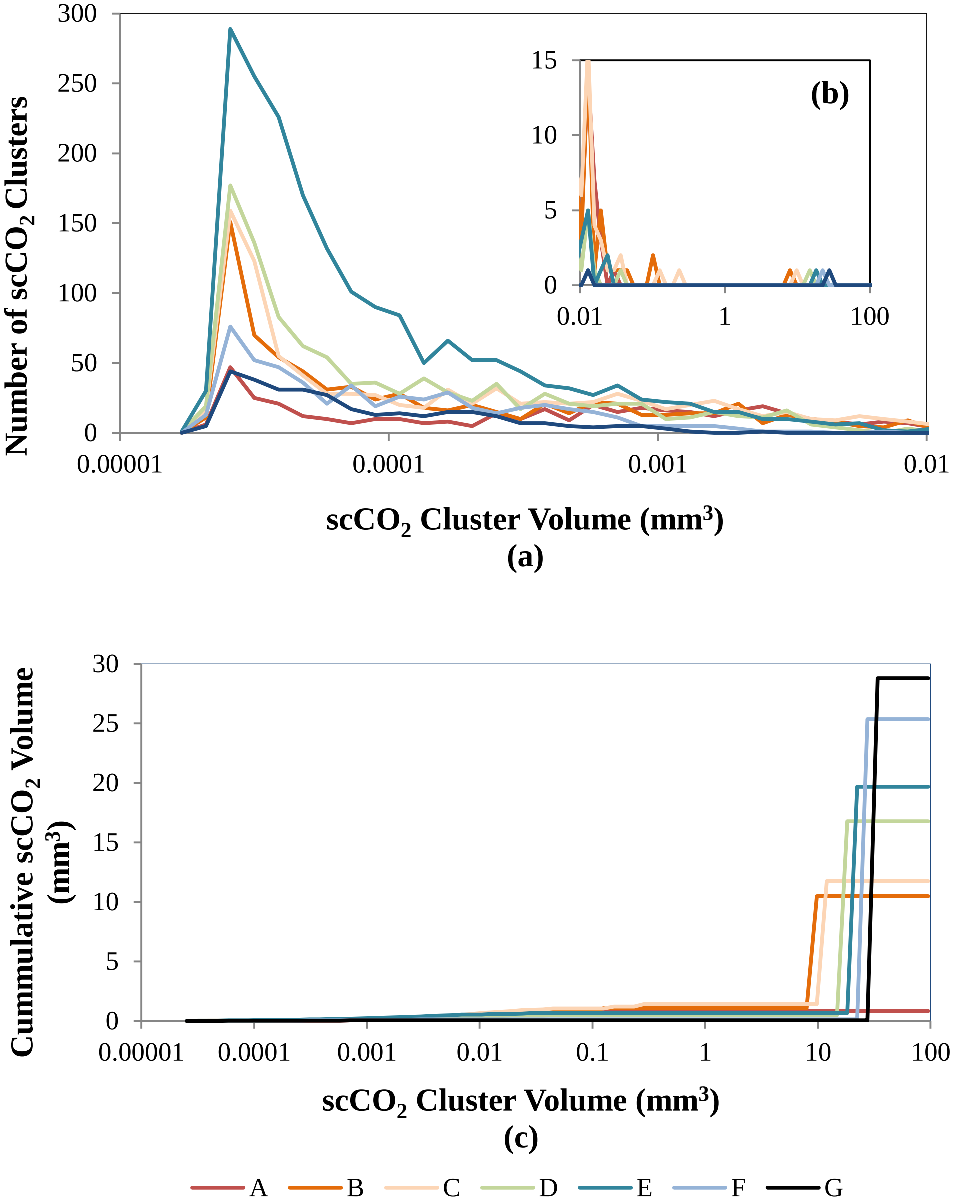

Figure 6-6. Size of supercritical CO$_2$ (scCO$_2$) fluid clusters at each point A-G during the brine drainage process in Bentheimer sandstone: (a) distribution of scCO$_2$ clusters as a function of cluster volume for small clusters less than 0.01 mm^3, (b) close-up view of distribution of scCO$_2$ clusters as a function of cluster volume for clusters larger than 0.01 mm^3, and (c) cumulative scCO$_2$ volume as a function of cluster volume. Note difference of scale between (a) and (b). Although there is a relatively large number of small (<0.01 mm^3) fluid clusters, most of the cumulative volume of scCO$_2$ present within the sandstone (greater than 90%) is derived from a single large cluster for drainage points B-G (with a size ranging from 9.4 mm^3 for scan B to 28.7 mm^3 for scan G).

Scan designation and corresponding core condition	S_W (-)	P_C (kPa)
A	0.95	0.0
B	0.67	3.2*
D	0.47	3.3
G	0.09	14.6

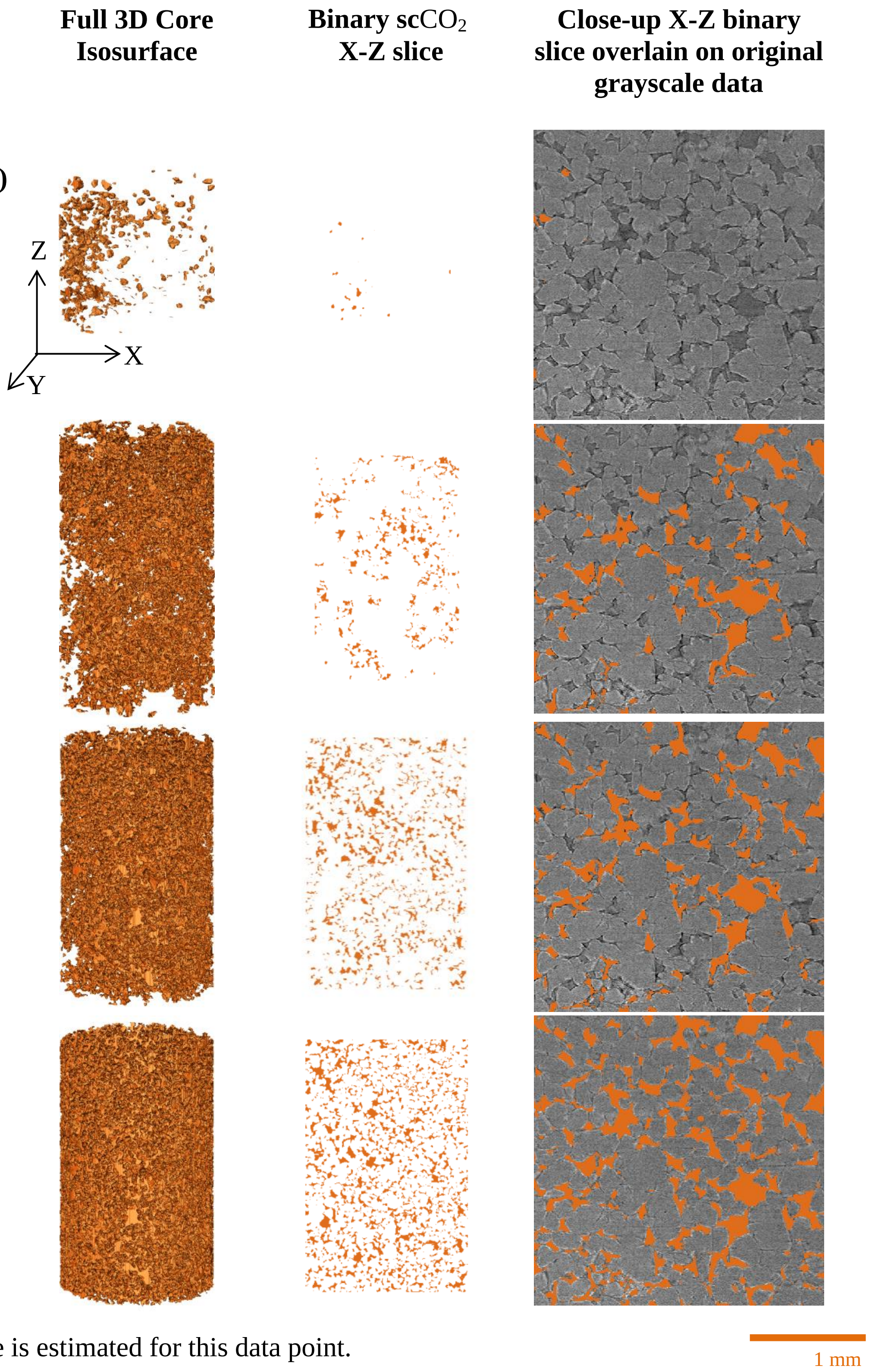

*Capillary pressure is estimated for this data point.

Figure 6-7. Three dimensional (3D) isosurfaces, two dimensional (2D) binary X-Z oriented slices, and a closer view of the 2D binary slices overlain on the original grayscale image of supercritical CO_2 ($scCO_2$) within Bentheimer sandstone at four points during the drainage process. Core diameter is approx. 6 mm and the scale is shown for the close-up slices.

For a drainage process in 2D micromodels, three flow regimes have been identified: capillary fingering is characterized by flow through a single interconnected flow path with a width of tens of pore bodies; viscous fingering presents several disconnected flow paths with widths of 1-3 pore bodies; and stable displacement occurs when the NW fluid advances as a solid front [Lenormand et al., 1988; Zhang et al., 2011]. The characteristics of these flow regimes are not as clearly defined in 3D porous media; however, the quantitative measures demonstrating high connectivity dominated by a single $scCO_2$ fluid cluster (Figures 6-5 and 6-6) and qualitative data illustrating the evolution of the $scCO_2$ front (Figure 6-7) we present here provide evidence that during this drainage experiment, $scCO_2$ invades the sandstone via capillary fingering. This is expected; given the low mobility ratio $M = \frac{\mu_{CO_2}}{\mu_{brine}} = 0.03$ and low capillary number $Ca = \frac{\mu_{CO_2} v_{CO_2}}{\sigma} = 10^{-8.6}$of this drainage experiment (Figure 6-8). The agreement between previous studies on 2D systems and the supercritical 3D system investigated here provides support that the flow regimes developed by examination of 2D micromodels [Lenormand et al., 1988; Wang et al., 2012; Zhang et al., 2011] are relevant to 3D systems with geologic porous media and supercritical conditions.

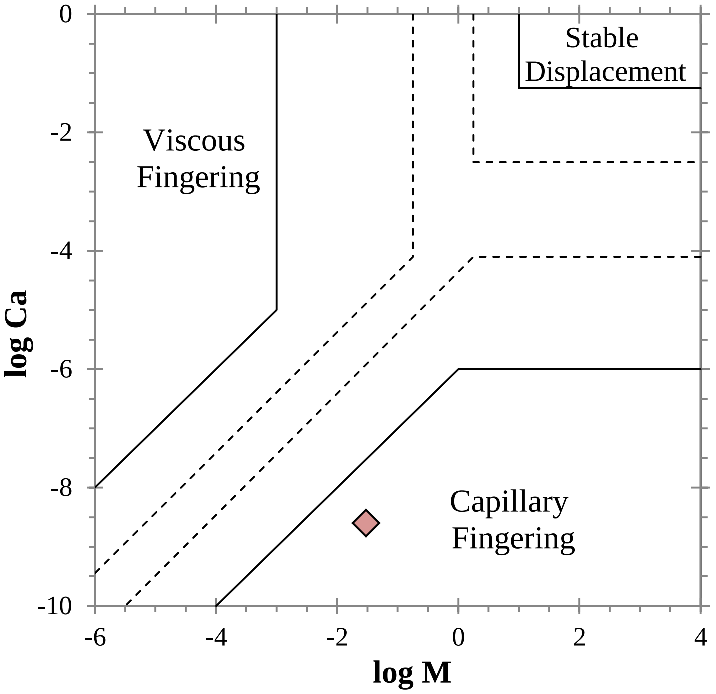

Figure 6-8. Flow regime phase diagram for drainage. The flow regimes are defined based on the capillary number (Ca) and mobility ratio (M) of the drainage process; solid lines indicate boundaries defined by Lenormand et al. [1988] and dashed lines indicate boundaries defined by Zhang et al. [2011]. Conditions of the scanned supercritical CO_2 ($scCO_2$) drainage experiment within Bentheimer sandstone are represented by the red diamond.

6.5 Conclusions

We have presented unique capillary pressure-saturation (P_c-S) curves for supercritical CO_2 ($scCO_2$) and brine at reservoir conditions, i.e. 37.5°C and 8.3 MPa, where the saturation data is calculated from x-ray CMT images paired with bulk measurements of capillary pressure via pressure transducers. We have compared the $scCO_2$ P_c-S curve to an ambient P_c-S curve and normalization of the capillary pressure curves by the air-brine and $scCO_2$-brine interfacial tensions (σ) results in a single P_c/σ-S curve that describes primary drainage for both ambient and supercritical conditions. We have shown that quasi-static equilibrium capillary pressure data overlap that obtained in continuous pressure experiments of the primary drainage process of $scCO_2$ in Bentheimer sandstone at reservoir conditions and low flow rate. We have obtained much lower initial saturations of brine in our system (9%) than reported in other studies (30-75%), which, because of our use of a hydrophilic membrane at the brine outlet, better approximates a semi-infinite geologic medium, and which we believe is a more realistic characterization of CO_2 storage capacity during drainage. These experiments have highlighted the importance of temperature uniformity throughout the experimental system due to the possibility of $scCO_2$ exsolution due to temperature variation. Additionally, we have investigated the connectivity of the $scCO_2$ front on a pore-scale basis and provided both quantitative and qualitative evidence demonstrating $scCO_2$ invasion via capillary fingering, which is consistent with mobility ratio/capillary number-based predictions obtained at ambient pressure [Lenormand et al., 1988; Zhang et al., 2011] and in homogenous (2D) high-pressure CO_2 system micromodel studies [Wang et al., 2012]. Our results show a very complete drainage process of $scCO_2$ displacing brine (to a brine saturation of 9% at the end of primary drainage) in a capillary fingering flow regime using sandstone at reservoir conditions and indicate that 2D and ambient system experiments can be used to approximate $scCO_2$ flow processes during primary drainage.

6.6 Acknowledgements

We gratefully acknowledge the support of the U.S. Department of Energy through the LANL/LDRD Program (#20100025DR) for this work; as well as the Department of Energy's Basic Energy Sciences, Geosciences Program via grant number DE-FG02-11ER16277. Use of the Advanced Photon Source, an Office of Science User Facility operated for the U.S. Department of Energy (DOE) Office of Science by Argonne National Laboratory, was supported by the U.S. DOE under Contract No. DE-AC02-06CH11357. We acknowledge the support of GeoSoilEnviroCARS (Sector 13), which is supported by the National Science Foundation - Earth Sciences (EAR-1128799), and the Department of Energy, Geosciences (DE-FG02-94ER14466). L. Andersson wishes to acknowledge funding from the Swedish Science Council. We are grateful to the GSECARS staff for technical support during beam-time, in particular Dr. Mark Rivers.

6.7 References

Akbarabadi, M., and M. Piri (2013), Relative permeability hysteresis and capillary trapping characteristics of supercritical CO_2/brine systems: An experimental study at reservoir conditions, Advances in Water Resources, 52, 190-206.

Bachu, S., and B. Bennion (2008a), Interfacial Tension between CO_2, Freshwater, and Brine in the Range of Pressure from (2 to 27) MPa, Temperature from (20 to 125) °C, and Water Salinity from (0 to 334 000) mg•L−1, Journal of Chemical & Engineering Data, 54(3), 765-775.

Bachu, S., and B. Bennion (2008b), Effects of in-situ conditions on relative permeability characteristics of CO_2-brine systems, Environmental Geology, 54(8), 1707-1722.

Blunt, M. J., B. Bijeljic, H. Dong, O. Gharbi, S. Iglauer, P. Mostaghimi, A. Paluszny, and C. Pentland (2013), Pore-scale imaging and modelling, Advances in Water Resources, 51, 197-216.

Broseta, D., N. Tonnet, and V. Shah (2012), Are rocks still water-wet in the presence of dense CO_2 or H2S?, Geofluids, 12(4), 280-294.

Chalbaud, C., M. Robin, J. M. Lombard, F. Martin, P. Egermann, and H. Bertin (2009), Interfacial tension measurements and wettability evaluation for geological CO_2 storage, Advances in Water Resources, 32(1), 98-109.

Chaudhary, K., M. Bayani Cardenas, W. W. Wolfe, J. A. Maisano, R. A. Ketcham, and P. C. Bennett (2013), Pore-scale trapping of supercritical CO_2 and the role of grain wettability and shape, Geophysical Research Letters, 40(15), 3878-3882.

El-Maghraby, R. M., and M. J. Blunt (2012), Residual CO_2 Trapping in Indiana Limestone, Environmental Science & Technology, 47(1), 227-233.

Herring, A. L., E. J. Harper, L. Andersson, A. Sheppard, B. K. Bay, and D. Wildenschild (2013), Effect of fluid topology on residual nonwetting phase trapping: Implications for geologic CO_2 sequestration, Advances in Water Resources, 62, 47-58.

http://webbook.nist.gov/chemistry/, a. f., edited.

Iglauer, S., A. Paluszny, C. H. Pentland, and M. J. Blunt (2011), Residual CO_2 imaged with X-ray micro-tomography, Geophysical Research Letters, 38(21), L21403.

IPCC (2005), IPCC special report on carbon dioxide capture and storage.

Ketcham, R. A., and W. D. Carlson (2001), Acquisition, optimization and interpretation of X-ray computed tomographic imagery: applications to the geosciences, Computers & Geosciences, 27(4), 381-400.

Krevor, S. C. M., R. Pini, L. Zuo, and S. M. Benson (2012), Relative permeability and trapping of CO_2 and water in sandstone rocks at reservoir conditions, Water Resources Research, 48(2), W02532.

Lenormand, R., C. Zarcone, and A. Sarr (1983), Mechanisms of the displacement of one fluid by another in a network of capillary ducts, Journal of Fluid Mechanics, 135, 337-353.

Lenormand, R., E. Touboul, and C. Zarcone (1988), Numerical models and experiments on immiscible displacements in porous media, Journal of Fluid Mechanics, 189, 165-187.

Maloney, D. R., M. M. Honarpour, and A. D. Brinkmeyer (1990), The effects of rock characteristics on relative permeabilityRep. NIPER-441; Other: ON: DE90000212 United StatesOther: ON: DE90000212Wed Feb 06 15:58:38 EST 2008NTIS, PC A03/MF A01 - OSTI; GPO Dep.NETL; EDB-90-031427; NTS-90-009616; ERA-15-015946English, 29 pp.

Morrow, N. R., I. Chatzis, and J. T. Taber (1988), Entrapment and mobilization of residual oil in bead packs, SPE Reservoir Engineering, 3(3), 927-934.

Øren, P.-E., S. Bakke, and O. J. Arntzen (1998), Extending predictive capabilities to network models, SPE Journal, 3(4), 324-336.

Pentland, C. H., R. El-Maghraby, S. Iglauer, and M. J. Blunt (2011a), Measurements of the capillary trapping of super-critical carbon dioxide in Berea sandstone, Geophys. Res. Lett., 38(6), L06401.

Pentland, C. H., R. El-Maghraby, A. Georgiadis, S. Iglauer, and M. J. Blunt (2011b), Immiscible Displacements and Capillary Trapping in CO_2 Storage, Energy Procedia, 4, 4969-4976.

Pentland, C. H., S. Iglauer, O. Gharbi, K. Okada, and T. Suekane (2012), The influence of pore space geometry on the entrapment of carbon dioxide by capillary forces, paper presented at SPE Asia Pacific Oil and Gas Conference and Exhibition, Society of Petroleum Engineers.

Perrin, J.-C., M. Krause, C.-W. Kuo, L. Miljkovic, E. Charoba, and S. M. Benson (2009), Core-scale experimental study of relative permeability properties of CO_2 and brine in reservoir rocks, Energy Procedia, 1(1), 3515-3522.

Pini, R., S. C. M. Krevor, and S. M. Benson (2012), Capillary pressure and heterogeneity for the CO_2/water system in sandstone rocks at reservoir conditions, Advances in Water Resources, 38, 48-59.

Plug, W. J., and J. Bruining (2007), Capillary pressure for the sand-CO_2-water system under various pressure conditions. Application to CO_2 sequestration, Advances in Water Resources, 30(11), 2339-2353.

Polak, S., Y. Cinar, T. Holt, and O. Torsæter (2011), An experimental investigation of the balance between capillary, viscous, and gravitational forces during CO_2 injection into saline aquifers, Energy Procedia, 4, 4395-4402.

Qi, R., T. C. LaForce, and M. J. Blunt (2009), Design of carbon dioxide storage in aquifers, International Journal of Greenhouse Gas Control, 3(2), 195-205.

Renard, P., and D. Allard (2013), Connectivity metrics for subsurface flow and transport, Advances in Water Resources, 51, 168-196.

Rivers, M. L., S. R. Sutton, and P. J. Eng (1999), Geoscience applications of x-ray computed microtomography, paper presented at SPIE's International Symposium on Optical

Science, Engineering, and Instrumentation, International Society for Optics and Photonics.

Silin, D., L. Tomutsa, S. Benson, and T. Patzek (2011), Microtomography and Pore-Scale Modeling of Two-Phase Fluid Distribution, Transp Porous Med, 86(2), 495-515.

Wang, Y., C. Zhang, N. Wei, M. Oostrom, T. W. Wietsma, X. Li, and A. Bonneville (2012), Experimental Study of Crossover from Capillary to Viscous Fingering for Supercritical CO_2–Water Displacement in a Homogeneous Pore Network, Environmental Science & Technology, 47(1), 212-218.

Wardlaw, N. C., and L. Yu (1988), Fluid topology, pore size and aspect ratio during imbibition, Transp Porous Med, 3(1), 17-34.

Wildenschild, D., and A. P. Sheppard (2013), X-ray imaging and analysis techniques for quantifying pore-scale structure and processes in subsurface porous medium systems, Advances in Water Resources, 51(0), 217-246.

Wildenschild, D., J. Hopmans, M. Rivers, and A. Kent (2005), Quantitative analysis of flow processes in a sand using synchrotron-based X-ray microtomography, Vadose Zone Journal, 4(1), 112-126.

Wildenschild, D., C. M. P. Vaz, M. L. Rivers, D. Rikard, and B. S. B. Christensen (2002), Using X-ray computed tomography in hydrology: systems, resolutions, and limitations, Journal of Hydrology, 267(3–4), 285-297.

Wildenschild, D., R. T. Armstrong, A. L. Herring, I. M. Young, and J. William Carey (2011), Exploring capillary trapping efficiency as a function of interfacial tension, viscosity, and flow rate, Energy Procedia, 4, 4945-4952.

Zhang, C., M. Oostrom, T. W. Wietsma, J. W. Grate, and M. G. Warner (2011), Influence of Viscous and Capillary Forces on Immiscible Fluid Displacement: Pore-Scale Experimental Study in a Water-Wet Micromodel Demonstrating Viscous and Capillary Fingering, Energy & Fuels, 25(8), 3493-3505.

Chapter 7. Summary and Conclusions

7.1 Research Summary

The research presented in this dissertation has utilized x-ray computed microtomography (x-ray CMT) to investigate nonwetting (NW) phase fluid movement and trapping on a pore-scale basis. In particular, we have utilized ambient-condition core experiments to focus on three areas of study which are of significant importance to geologic sequestration of supercritical phase CO_2:

(1) Variation of wetting (W) and NW fluid/engineering/medium properties and the resulting transitions in pore-scale force dominance

(2) Impact of the post-drainage, initial state of the system on the post-imbibition, residual state of the system

(3) Influence of wettability state on NW phase fluid flow and mobilization

In addition, supercritical-condition CO_2 flow experiments have been conducted and related the results to ambient condition studies to demonstrate the applicability of previously developed flow models.

Though the investigation attempted to isolate the individual effect of these issues, each one influences the others, with the result that all must be considered in order to fully describe an experimental system.

Chapter 3 presented results of an ambient condition experimental study investigating NW phase trapping during one drainage-imbibition cycle, using multiple W-NW fluid pairs in sintered glass bead columns. It was demonstrated that viscous and gravitational forces, as described by Mobility ratio and Bond number, control trapping in that experimental system rather than capillary forces. Chapter 4 presented an additional ambient condition study of NW (air) trapping in air-brine drainage-imbibition experiments in Bentheimer sandstone, which (contrary to the glass bead system) show trapping to be a function of imbibition Capillary number. To explain the difference in results for different experimental systems, a method is presented in Chapter 4 for estimating pore-scale force dependence as a function of fluid properties (viscosity, density, interfacial tension), engineering parameters (flow rate), and medium properties (grain size); this analysis allows for prediction of the forces and parameters which will have the greatest impact on capillary trapping in a multiphase-porous medium system.

Also in Chapter 4, the same air-brine Bentheimer sandstone system was used to investigate how the initial state of the system (in particular, the connectivity and topology of NW phase at the initial state) impacts the residual state of the system. Two quantitative metrics were used to describe initial state connectivity and topology. The gamma function, Γ(NW), measures the ratio of connected pairs of individual NW voxels to *all* the possible pairs of NW voxels in the data volume. The normalized Euler number, $\hat{\chi}_{NW}$, is a topological measure of the relative amount of distinct individual NW fluid clusters to the number of redundant connections within NW fluid clusters in the data volume, normalized to the the χ value of the same medium at 100% NW phase saturation. For $\Gamma(\mathrm{NW}) = \hat{\chi}_{NW} = 1.0$, NW phase is at maximum connectivity. It was shown that capillary trapping efficiency decreases linearly as initial $\hat{\chi}_{NW}$ increases, demonstrating that NW phase mobilization is more likely if the number of redundant connections within NW phase at the initial state is high. This effect was found to be more significant for systems dominated by viscous forces, compared to capillary forces.

Results of ambient condition experiments of air and brine flow in Bentheimer sandstone which had been treated to exhibit varying degrees of wettability (strongly water-wet, weakly water-wet, and intermediate-wet) were discussed in Chapter 5. It was demonstrated that reduced capillary trapping resulted for systems with contact angle closer to 90^o; and also quantitatively and qualitatively shown that flow patterns are significantly different for systems of different wettability: as contact angle increases towards 90^o, capillary forces are reduced and flow is dominated by buoyancy forces.

In Chapter 6, a novel supercritical condition experimental system was introduced that allows for experiments wherein bulk measurements (i.e. pressure measurements across the core) are coupled with in-situ synchrotron x-ray CMT visualization of supercritical CO_2 flow. It was demonstrated that by consideration of the influence of viscous and capillary forces, drainage of supercritical CO_2 follows flow regimes developed in ambient condition 2D micromodel experiments; this confirms that pore-scale phenomena observed at ambient conditions are influential to flow processes at geologic conditions as well.

7.2 Application to Geologic Sequestration

For application to carbon capture and storage (CCS) operations, this research suggests that in order to optimize capillary trapping of supercritical CO_2 in a geologic storage reservoir:

- The supercritical CO_2-brine-geologic reservoir system should be analyzed from a pore-scale force balance perspective to determine which fluid/flow/medium properties will dominate the capillary trapping process.
- Engineering parameters of the CO_2 and/or chase brine injections (e.g. temperature, pressure, flow rate) can be more efficiently optimized based on the above force balance analysis.
- Reservoir medium properties (grain- and pore-size distribution, and wettability) should be carefully considered in order to limit the effects of gravity and thus reduce buoyant transport of CO_2.
- CO_2 injection should be managed in order to limit connectivity of the CO_2 after injection stops; either by limiting the initial CO_2 saturation or by manipulation of injection patterns. For example, one suggestion would be to have a shorter vertical injection interval in the injection well: injection only into the lower portions of the aquifer would allow for vertical migration and might prevent the CO_2 plume from approaching high saturation levels at the injection point.
- After CO_2 injection, the subsequent imbibition process should be carried out at very low Ca regime; this would be accomplished by allowing imbibition via natural groundwater flow, or by using very low flow rates for chase brine injection.

7.3 Future Work

In this work several factors which influence capillary trapping in ambient condition systems have been investigated, and it has been demonstrated that it is feasible to investigate these same factors in supercritical-condition experiments. The supercritical experimental set-up which was designed, built, and implemented during the course of the work encompassing this dissertation, and which was presented in Chapter 6, is uniquely capable of investigation of the same factors under supercritical conditions:

- The pore-scale force balance analysis presented in Chapter 4 should be confirmed for supercritical conditions. Increasing or decreasing experimental pressure and temperature, and increasing experimental flow rate will allow for exploration of buoyancy, viscosity, and capillary-dominated flow and trapping of supercritical CO_2.
- The relationship between initial state connectivity and capillary trapping, as presented in Chapter 4, should be confirmed for supercritical conditions in order to verify the importance of considering CO_2 topology during CO_2 injection. Conducting a series of supercritical condition drainage-imbibition capillary trapping experiments would allow for investigation of this relationship. Further, CO_2 connectivity and topology in different and more heterogeneous media could also be studied.
- Wettability alteration as a function of exposure to supercritical CO_2 and brine can be investigated from a pore-scale perspective by investigation of supercritical CO_2-brine-solid interfaces (e.g. Andrew et al.[2014]). A temporal change in contact angle of residually trapped CO_2 clusters, along with visualization of successive CO_2 flow patterns (as in Chapter 5) during multiple drainage-imbibition cycles of supercritical CO_2 and brine would allow for determination of wettability alteration and prediction of CO_2 flow in wettability altered media.

To further confirm applicability of these findings for CO_2 sequestration applications, upscaling relationships need to be developed which link these pore-scale processes to overall reservoir-scale trapping mechanisms. For this, larger scale ambient condition experiments with proxy fluids could be conducted with 2D visualization based techniques (e.g. neutron radiography, or use of “transparent soils”).

Chapter 8. Bibliography

Akbarabadi, M., and M. Piri (2013), Relative permeability hysteresis and capillary trapping characteristics of supercritical CO2/brine systems: An experimental study at reservoir conditions, *Adv. Water Resour.*, *52*, 190–206.

Anderson, W. G. (1987), Wettability Literature Survey- Part 4: Effects of Wettability on Capillary Pressure, *J. Pet. Technol.*, *39*(10), 1283–1300, doi:10.2118/15271-PA.

Andrew, M., B. Bijeljic, and M. J. Blunt (2014), Pore-scale contact angle measurements at reservoir conditions using X-ray microtomography, *Adv. Water Resour.*, *68*, 24–31, doi:10.1016/j.advwatres.2014.02.014.

Armstrong, R. T., A. Georgiadis, H. Ott, D. Klemin, and S. Berg (2014), Critical capillary number: Desaturation studied with fast X-ray computed microtomography, *Geophys. Res. Lett.*, *41*(1), 55–60.

Bachu, S. (2003), Screening and ranking of sedimentary basins for sequestration of CO2 in geological media in response to climate change, *Environ. Geol.*, *44*(3), 277–289, doi:10.1007/s00254-003-0762-9.

Bachu, S., and B. Bennion (2008), Effects of in-situ conditions on relative permeability characteristics of CO2-brine systems, *Environ. Geol.*, *54*(8), 1707–1722, doi:10.1007/s00254-007-0946-9.

Bachu, S., and B. D. Bennion (2009), Dependence of CO2 -brine interfacial tension on aquifer pressure, temperature and water salinity, *Energy Procedia*, *1*(1), 3157–3164, doi:10.1016/j.egypro.2009.02.098.

Bachu, S., D. B. Bennion, K. Clark, R. Nw, and A. Tn (2009), Interfacial Tension between CO 2 , Freshwater , and Brine in the Range of Pressure from (2 to 27) MPa , Temperature from (20 to 125) ° C , and Water Salinity from (0 to 334 000) mg · L - 1, , 765–775.

Broseta, D., N. Tonnet, and V. Shah (2012), Are rocks still water-wet in the presence of dense CO2 or H2S?, *Geofluids*, *12*(4), 280–294, doi:10.1111/j.1468-8123.2012.00369.x.

Cense, A. W., and S. Berg (2009), The Viscous-Capillary Paradox in 2-Phase Flow in Porous Media, in *International Symposium of the Society of Core Analysts*, Shell International Exploration & Production, Noordwijk, The Netherlands.

Chalbaud, C., M. Robin, S. Bekri, and P. Egermann (2007), Wettability impact on CO2 storage in aquifers: visualisation and quantification using micromodel tests, pore network model and reservoir simulations, in *International symposium of the society of core analysts, Calgary, Canada*.

Chatzis, I., and N. R. Morrow (1984), Correlation of capillary number relationships for sandstone, *J. Name SPEJ, Soc. Pet. Eng. J.; (United States); J. Vol. 245*, Medium: X; Size: Pages: 555–562.

Chatzis, I., N. Morrow, and H. Lim (1983), Magnitude and detailed structure of residual oil saturation, *Old SPE J.*, *23*(2), 311–326.

Chatzis, I., M. S. Kuntamukkula, and N. R. Morrow (1988), Effect of capillary number on the microstructure of residual oil in strongly water-wet sandstones, *J. Name SPE (Society Pet. Eng. Reserv. Eng.; (United States); J. Vol. 33*, Medium: X; Size: Pages: 902–912.

Chiquet, P., D. Broseta, F. Complexes, U. Pau, and S. Thibeau (2005), SPE 94183 Capillary Alteration of Shaly Caprocks by Carbon Dioxide, , (1), 1–10.

Chiquet, P., J.-L. Daridon, D. Broseta, and S. Thibeau (2007a), CO2/water interfacial tensions under pressure and temperature conditions of CO2 geological storage, *Energy Convers. Manag.*, *48*(3), 736–744, doi:10.1016/j.enconman.2006.09.011.

Chiquet, P., D. Broseta, and S. Thibeau (2007b), Wettability alteration of caprock minerals by carbon dioxide, *Geofluids*, *7*(2), 112–122, doi:10.1111/j.1468-8123.2007.00168.x.

Cnudde, V., and M. N. Boone (2013), High-resolution X-ray computed tomography in geosciences: A review of the current technology and applications, *Earth-Science Rev.*, *123*, 1–17, doi:10.1016/j.earscirev.2013.04.003.

Ding, M., and A. Kantzas (2007), *Capillary number correlations for gas-liquid systems*, Society of Petroleum Engineers, Calgary, CANADA.

Fry, V. A., J. S. Selker, and S. M. Gorelick (1997), Experimental investigations for trapping oxygen gas in saturated porous media for in situ bioremediation, *Water Resour. Res.*, *33*(12), 2687–2696, doi:10.1029/97wr02428.

Geistlinger, H., S. Mohammadian, S. Schlueter, and H.-J. Vogel (2014), Quantification of capillary trapping of gas clusters using X-ray microtomography, *Water Resour. Res.*, *50*(5), 4514–4529, doi:10.1002/2013WR014657.

Harper, E. J., and D. D. Wildenschild (2012), Optimization of Capillary Trapping for CO2 Sequestration in Saline Aquifers, Oregon State University, Corvallis, Oregon.

Hughes, R. G., and M. J. Blunt (2000), Pore Scale Modeling of Rate Effects in Imbibition, *Transp. Porous Media*, *40*(3), 295–322, doi:10.1023/a:1006629019153.

Iglauer, S. (2011), Dissolution Trapping of Carbon Dioxide in Reservoir Formation Brine – A Carbon Storage Mechanism, in *Mass Transfer - Advanced Aspects*, edited by H. Nakajima, p. 824, InTech.

IPCC (2005), *IPCC special report on carbon dioxide capture and storage*, edited by B. Metz, O. Davidson, H. de Coninck, M. Loos, and L. Meyer.

Jamaloei, B. Y., K. Asghari, and R. Kharrat (2012), The investigation of suitability of different capillary number definitions for flow behavior characterization of surfactant-based chemical flooding in heavy oil reservoirs, *J. Pet. Sci. Eng.*, *90–91*(0), 48–55, doi:10.1016/j.petrol.2012.04.020.

Ketcham, R. A., and W. D. Carlson (2001), Acquisition, optimization and interpretation of X-ray computed tomographic imagery: applications to the geosciences, *Comput. & Geosci.*, *27*(4), 381–400, doi:10.1016/s0098-3004(00)00116-3.

Kim, Y., J. Wan, T. J. Kneafsey, and T. K. Tokunaga (2012), Dewetting of Silica Surfaces upon Reactions with Supercritical CO2 and Brine: Pore-Scale Studies in Micromodels, *Environ. Sci. Technol.*, *46*(7), 4228–4235, doi:10.1021/es204096w.

Krevor, S. C. M., R. Pini, L. Zuo, and S. M. Benson (2012), Relative permeability and trapping of CO2 and water in sandstone rocks at reservoir conditions, *Water Resour. Res.*, *48*(2), W02532, doi:10.1029/2011wr010859.

Land, C. (1968), Calculation of imbibition relative permeability for two-and three-phase flow from rock properties, *Old SPE J.*, *8*(2), 149–156.

Lenormand, R., E. Touboul, and C. Zarcone (1988), Numerical models and experiments on immiscible displacements in porous media, *J. Fluid Mech.*, *189*, 165–187, doi:doi:10.1017/S0022112088000953.

Al Mansoori, S. K., E. Itsekiri, S. Iglauer, C. H. Pentland, B. Bijeljic, and M. J. Blunt (2010), Measurements of non-wetting phase trapping applied to carbon dioxide storage, *Int. J. Greenh. Gas Control*, *4*(2), 283–288, doi:10.1016/j.ijggc.2009.09.013.

Morrow, N. R., I. Chatzis, and J. T. Taber (1988), Entrapment and mobilization of residual oil in bead packs, *SPE Reserv. Eng.*, *3*(3), 927–934.

Nguyen, V. H., A. P. Sheppard, M. A. Knackstedt, and W. Val Pinczewski (2006), The effect of displacement rate on imbibition relative permeability and residual saturation, *J. Pet. Sci. Eng.*, *52*(1-4), 54–70, doi:10.1016/j.petrol.2006.03.020.

Selker, J. S., J. T. McCord, and C. K. Keller (1999), *Vadose zone processes*, CRC Press.

Taina, I. A., R. J. Heck, and T. R. Elliot (2008), Application of X-ray computed tomography to soil science: A literature review, *Can. J. Soil Sci.*, *88*(1), 1–19, doi:10.4141/CJSS06027.

Treiber, L. E., and W. W. Owens (1972), A Laboratory Evaluation of the Wettability of Fifty Oil-Producing Reservoirs, *Soc. Pet. Eng. J.*, *12*(06), 531–540, doi:10.2118/3526-PA.

Wang, Y., C. Zhang, N. Wei, M. Oostrom, T. W. Wietsma, X. Li, and A. Bonneville (2012), Experimental Study of Crossover from Capillary to Viscous Fingering for Supercritical CO2–Water Displacement in a Homogeneous Pore Network, *Environ. Sci. Technol.*, *47*(1), 212–218.

Wildenschild, D., and A. P. Sheppard (2013), X-ray imaging and analysis techniques for quantifying pore-scale structure and processes in subsurface porous medium systems, *Adv. Water Resour.*, *51*(0), 217–246, doi:http://dx.doi.org/10.1016/j.advwatres.2012.07.018.

Wildenschild, D., C. M. P. Vaz, M. L. Rivers, D. Rikard, and B. S. B. Christensen (2002), Using X-ray computed tomography in hydrology: systems, resolutions, and limitations, *J. Hydrol.*, *267*(3–4), 285–297, doi:10.1016/s0022-1694(02)00157-9.

Zhang, C., M. Oostrom, T. W. Wietsma, J. W. Grate, and M. G. Warner (2011), Influence of Viscous and Capillary Forces on Immiscible Fluid Displacement: Pore-Scale Experimental Study in a Water-Wet Micromodel Demonstrating Viscous and Capillary Fingering, *Energy & Fuels*, *25*(8), 3493–3505, doi:10.1021/ef101732k.